Chapter 3
Converging Shocks

3.1 Introduction

We started this book by giving some examples of shock waves that each one of us has experienced many times. One example of such events is lightning followed by a thunder. Extremely hot air produced by lightning functions as a piston as it rapidly expands into the cool surrounding air and creates an outgoing shock. The shock strength decreases as the shock expands and is transformed into a sound wave producing low rumbling that we call thunder. In terms of energy, one can say that a very high initial energy density produced by a thin streak of lightning is spread over a large volume of surrounding air with a much lower-energy concentration. But is it possible to reverse this process? Is it possible to transform thunder into lightning? At the first glance, this seems to belong more to the realm of science fiction. However, as we shall see later in this chapter, this is achieved experimentally by "collecting" energy spread over a large volume into a tiny spot through shock focusing.

Figure 3.1a shows an initial burst of energy produced by a lightning generating a shock wave. In Fig. 3.1b we can see a 5 mm high and 0.1 mm thick streak of glowing argon gas obtained as a result of a reverse process when initial energy of the shock wave generated in a shock tube is focused at the center of the cylindrical test chamber of the tube. The initial energy produced in the shock tube is here concentrated in a tiny volume producing temperatures in excess of 6000 K in compressed argon gas. Later in this chapter, we will describe this experiment along other shock focusing experiments with a substantially more powerful spherical shock convergence producing glowing argon plasma with temperatures in excess of 30,000 K as well as shock focusing in liquids leading to extreme pressures able to disintegrate metal at the focal region.

In this chapter we will consider complex, highly-nonlinear physical mechanisms governing convergence and focusing of strong shocks in gases and liquids. Why shocks? Shocks are closely connected to high-energy density. A shock or a blast wave is often created by an abrupt release of energy confined in space. Oppositely,

N. Apazidis, V. Eliasson, *Shock Focusing Phenomena*, Shock Wave and High Pressure Phenomena, https://doi.org/10.1007/978-3-319-75866-4_3

Fig. 3.1 (**a**) Common occurrences of shock waves in nature: lightning in the evening sky, from pixabay.com. (**b**) Radiation from 5 mm high, 0.1 mm thick streak of glowing argon gas at the center of a cylindrical test section of a shock tube, (**a**) As stands. (**b**) Reproduced from [65], with the permission of AIP Publishing

an already existing shock, propagating in a medium when confined to a small volume, has a potential to increase in strength and generate very high-energy concentration. This is manifested by extreme temperatures and pressures in, e.g., gas that are hard or even impossible to achieve by other methods. These extreme conditions may result in human injuries and substantial material damage when occurring uncontrolled or may be used with advantage if monitored in a well-defined environment. If this is so, is this not a perfect way to obtain an ever-increasing energy density by, for example, focusing a spherical shock at the center of a sphere? Unfortunately, this is prevented by the instability of the converging shock. While an expanding shock is stable, the converging shock is not. This means that even an asymmetric explosion in confined space will eventually result in a smooth expanding and at the same time weakening shock. On the other hand, an almost symmetric converging shock will initially increase in strength but eventually lose its symmetry and thus its ability to concentrate energy as it converges on the focal region. The questions of shock generation, shock front evolution and symmetry, and also stability as well as stabilization of the shock front will be discussed in this section. The physical properties of imploding shocks governing the convergence process is another subject of interest here. Finally, we will describe the extreme conditions of matter produced as a result of symmetric implosion in gas or liquid. Production of an extreme state of matter usually requires extreme levels of stored energy delivered by, for example, powerful lasers, intense heavy ion beams, etc. One of the most striking features of shock focusing is that the extreme state of matter in the focal region is in this case produced by a limited and as a matter of fact quite modest amount of input energy.

3.2 Generation of Converging Shocks: Initial Experiments

In the previous chapter, we touched upon the theory behind shock and blast waves, their mathematical description, as well as experimental methods used to study their properties. We are specifically interested in the properties of converging shocks and blast waves and discussed the famous similarity solution of a converging cylindrical or spherical shock published by Guderley in 1942 [52]. In the same way as the work of Guderley played a pivotal role in opening the field of theoretical investigations of converging shocks, the work of Perry and Kantrowitz [84] produced a road map of experimental studies in this area. This article, published in 1951, is a perfect example of a scientific work successfully passing the test by time and inspiring a large number of experimental as well as theoretical and numerical investigations in the area of shock wave convergence and focusing.

Not only is this study one of the earliest experimental investigations of converging shocks, but it also contains a discussion of several important physical phenomena that are directly related to the process of shock focusing and later further investigated by a large number of researchers. We are therefore starting this section by giving a short account of this and two other early experimental studies of shock convergence by Knystautas et al. [70] and Sturtevant and Kulkarny [102] that all played a leading role in this field of research.

The main purpose of these studies was to show the possibility of experimental production of converging shocks. How can one create a converging cylindrical shock in an ordinary shock tube? This is in a way a topological problem of transforming a plane shock into a ring. Perry and Kantrowitz [84] discuss the first experimental methods of producing cylindrical segments by converging channels with walls smoothly bent inward. They argue that the shock redistributes the curvature smoothly along the shock front transforming an initially plane shock to a curved cylindrical form. This mechanism of shock shaping leads to an idea of producing not just a segment but a complete cylindrical shock front by inserting a central teardrop-formed body along the axis of a shock tube. By leading the annular shock through the axisymmetric channel between the walls of the central body and the shock tube, they were able to produce initial cylindrical shock with a high degree of symmetry. The convergence process was then carefully investigated in the test section of the shock tube (that was equipped with glass windows to provide an opportunity to visualize the shocks) by means of schlieren photography (Fig. 3.2).

The authors were able to produce and observe the initial converging cylindrical shocks as well as outgoing reflected waves in the test section. Shocks with initial Mach numbers $M = 1.1$, $M = 1.4$, and $M = 1.8$ were generated. Helium was used as the driver gas and air and argon as driven gases in the test section. Luminosity was detected with argon as test gas. The question of stability of converging shocks was for the first time investigated experimentally. The authors observed a departure from the cylindrical form for strong shocks with initial Mach number of $M = 1.8$ as compared to cylindrical shocks with initial strength of $M = 1.1$. The stability was further investigated by perturbing the shock front by a small object inserted

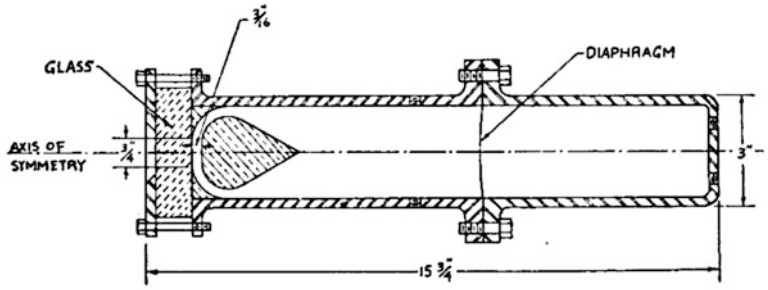

Fig. 3.2 Sketch of the cylindrical shock tube used in the first experiments on shock focusing by Perry and Kantrowitz, reproduced from [84], with the permission of AIP Publishing

along the path of the shock close to the edge of the test chamber. Although the authors concluded that the only effect of the disturbance was a shift of the center of convergence toward the disturbed side, traces of the disturbance may be clearly seen in Fig. 3.3c for the converging shock and even more clearly for the reflected shocks in Fig. 3.3d–f.

An important observation was the appearance of luminosity spots at the center of convergence appearing in argon as test gas at initial Mach number $M = 1.8$ shown in Fig. 3.4.

To summarize, we may say that the results of this pioneering work have inspired and guided a large number of researchers by utilizing a simple and yet effective method of experimental production of cylindrical converging shocks, by investigating their stability and ability to create high temperatures resulting in luminosity of the compressed gas at the center of convergence. Another very important feature of converging shocks raised in this investigation was the tendency to planarity of the shock front for strong shocks departing from cylindrical symmetry as seen in Fig. 3.5. We will see further that this feature plays an important role in understanding and controlling the process of strong shock convergence.

Another early experimental work on cylindrical shock convergence was performed by Knystautas et al. [70] in 1969. These authors used a different technique to produce cylindrically converging shocks, namely, a cylindrical implosion chamber. The shocks were generated by electric discharge initiated simultaneously in 30 equally spaced spark gaps at the cylinder boundary as illustrated in Fig. 3.6. By this method the authors were able to produce detonation waves in the acetylene-oxygen mixture. The researchers conducted optical and spectroscopic studies on the shock convergence. Shock fronts were visualized by the schlieren technique, and the temperature of the plasma at the center of convergence was measured by spectroscopic studies. A nearly cylindrical shock front may be seen in Fig. 3.7.

Knystautas, Lee, and Lee conclude that a smooth cylindrical shock front may be achieved by this method. Due to poor magnification of the optical schlieren system, they were unable to take images closer to the center of the chamber. What can be seen, however, in Fig. 3.7 is the tendency toward a square form which, as we will

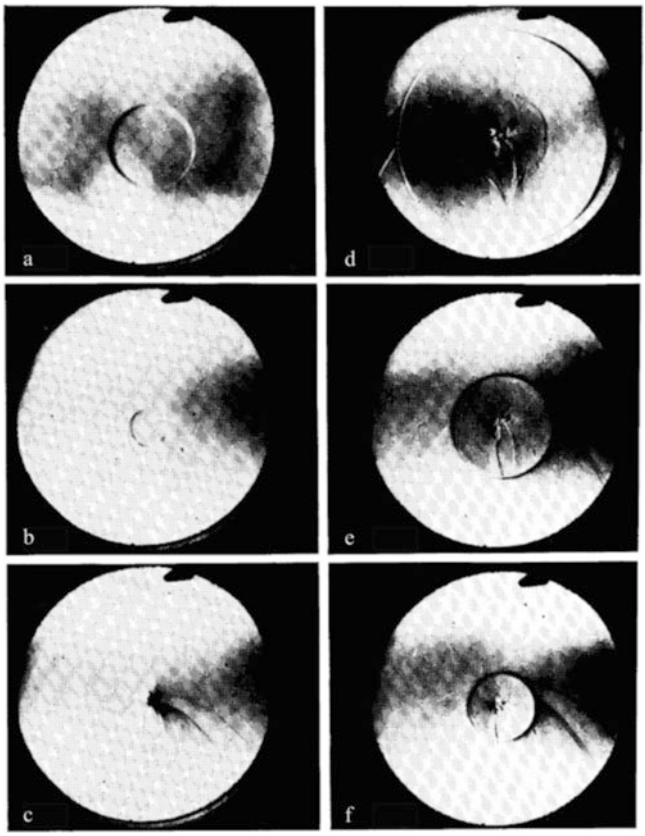

Fig. 3.3 Converging cylindrical shocks disturbed by an object, from [84] with the permission of AIP

see later, will be amplified as the shock converges on the implosion center. The spectroscopic measurements gave a very high temperature $T = 1.89 \cdot 10^5$ of the plasma at the center of the chamber. These measurements were however found to be erroneous later.

As the next important step in understanding the behavior of converging shocks in the focal area, we would like to highlight the experimental study by Sturtevant and Kulkarny [102]. These researchers conducted studies of an initially plane shocks of Mach numbers in the range $M = 1.005$–1.5 reflected from a parabolic reflector. By varying the strength of the shock from weak to moderately strong, they were able to observe various types of behavior in the focusing region. The authors investigate one of the main mechanisms of shock convergence or as they put it "... competition between the convergence of the sides of the focusing front and acceleration of its central portion." For weak shocks the first process is dominating, and the "... wave fronts emerge from the focus crossed and folded, in accordance with the predictions of geometrical acoustics theory. In the latter, the strong shock case, the fronts beyond

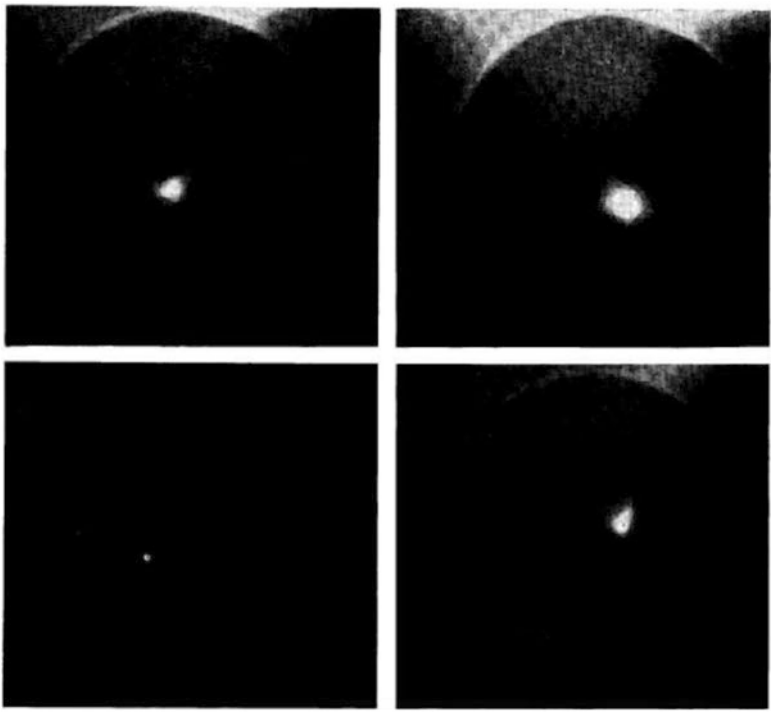

Fig. 3.4 Luminosity spots in argon at the center of shock wave convergence, reproduced from [84], with the permission of AIP

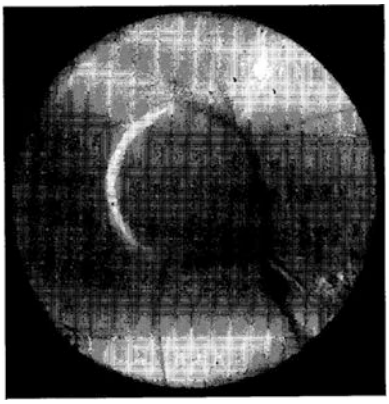

Fig. 3.5 Departure from cylindrical symmetry caused by a disturbance, reproduced from [84], with the permission of AIP

the focus are uncrossed, as predicted by the theory of shock dynamics." These various types of behaviors of weak and strong shocks are illustrated in Fig. 3.8. For weak shocks, the shock-shocks cross forming a triangular loop, while for strong shocks they do not cross but spread apart as can be seen from Fig. 3.8.

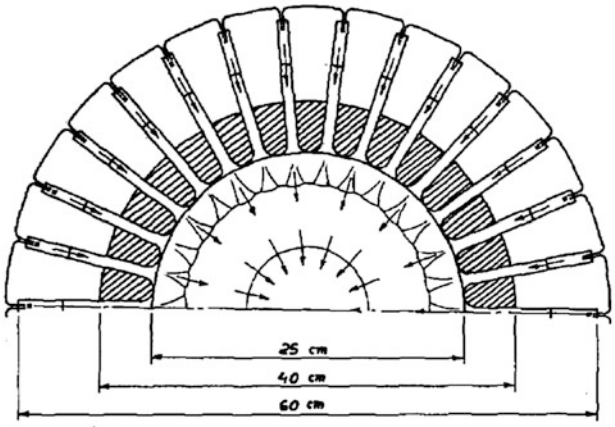

Fig. 3.6 Implosion chamber, reproduced from [70], with the permission of AIP

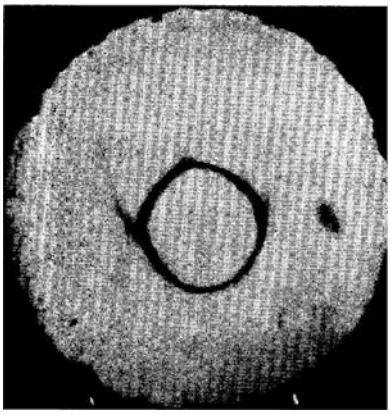

Fig. 3.7 Nearly cylindrical shock, reproduced from [70], with the permission of AIP

In a later article, Cates and Sturtevant [20] apply the theory of geometrical shock dynamics (GSD) [120] to model the behavior of weak, moderate, and strong shocks in the focal area observed experimentally. Later in this chapter, we will return to the role of artificial disturbances and their influence on the shape and stability of converging shocks. However, a time line of some of the research studies that have been performed on converging shock waves is summarized in Fig. 3.9.

3.3 Self-Similarity of Converging Shocks

As we have mentioned in the previous chapter and in the beginning of this chapter, the famous self-similarity solution for strong cylindrical and spherical converging shocks opened a whole new field of shock wave research. According to this solution,

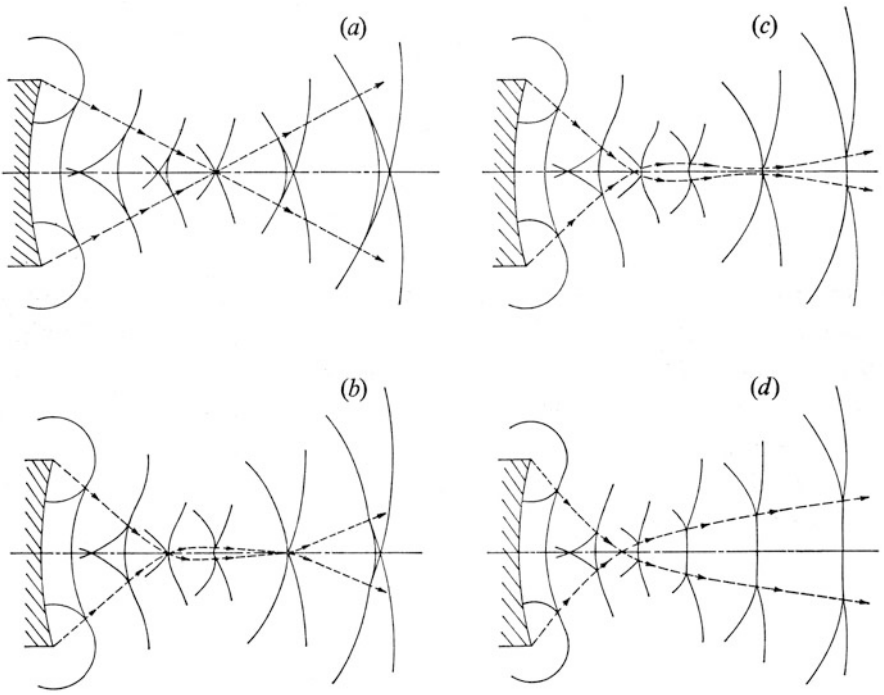

Fig. 3.8 Shock focusing for weak and moderately strong shocks, reproduced from [102], with permission from Cambridge University Press

the radius r of the converging shock is expressed in a self-similar form:

$$r = r_0\left(1 - \frac{t}{t_0}\right)^{\alpha} \tag{3.1}$$

where r_0 is the value of the radius at time $t = 0$ and α is the similarity constant that defines the strength of the convergence. The value of α depends on the adiabatic exponent γ of the gas. For air with $\gamma = 1.40$, Guderley determined the value of $\alpha \approx 0.835$ for converging cylindrical shocks and $\alpha \approx 0.717$ for converging spherical shocks.

A large number of analytical and numerical studies have been dedicated to the question of determining the value of α since; see, e.g., references [18, 48, 54, 81, 85, 99, 108]. Lazarus and Richtmyer [73] considered solutions for a wide range of values of the adiabatic exponents γ. This was further expanded in a thorough and detailed investigation by Lazarus [72], including extensive analytical analysis of the problem. This work presents values of α for a wide range of the adiabatic constant γ. Ponchaut et al. [85] investigate solution for imploding and reflecting cylindrical and spherical shocks, initially at rest. By means of dimensional analysis, they found a general solution of the problem in which Guderley power-law solution can be interpreted as the leading-order strong shock approximation valid in the

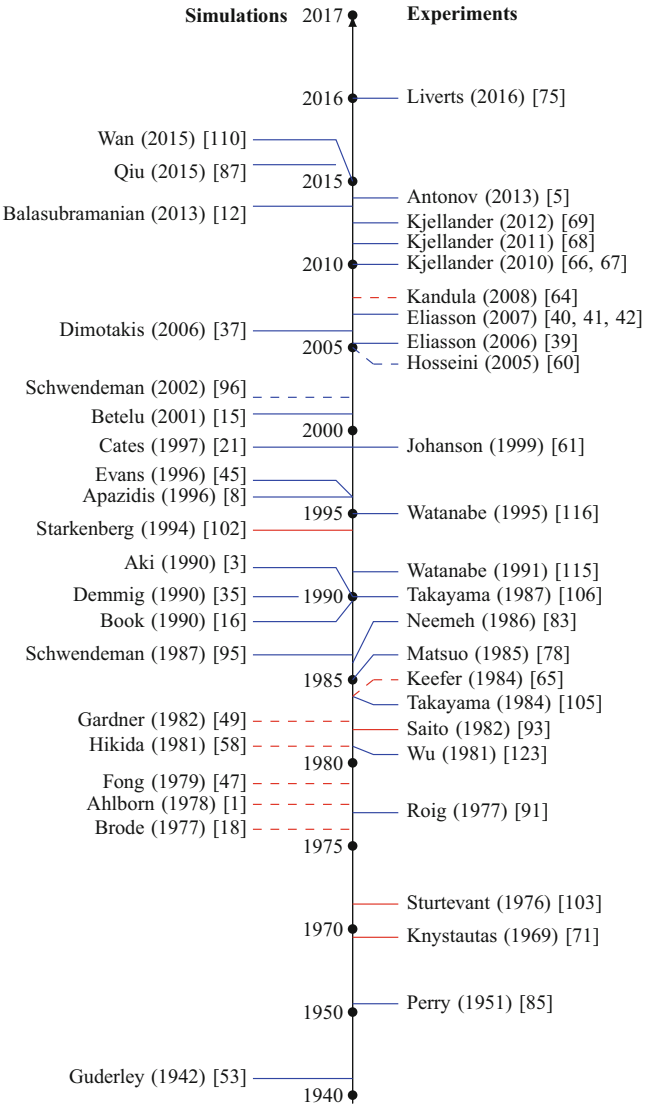

Fig. 3.9 Chronology of shock focusing research. Blue lines, shock waves with constant properties behind shock wave; red lines, shock waves generated by explosions; dashed lines, three-dimensional; solid lines, two-dimensional. Only first author is shown

vicinity of the implosion center. Later, Hornung et al. [58] presented an elegant approach to this problem by using Whitham's theory of geometrical shock dynamics (GSD) [120]. Although this theory gives an approximated description of shock propagation, neglecting the condition behind the advancing shock, it proved to be extremely successful in describing accelerating shocks. We will give a short

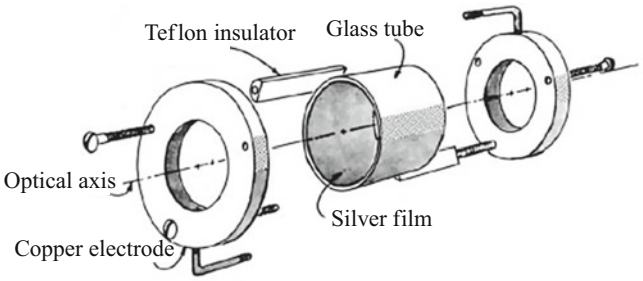

Fig. 3.10 Schematic of the cylindrical exploding wire setup, reproduced from [35], with permission from Springer

account of this theory in the next section. GSD allows for a very simple form of solution for converging cylindrical and spherical shocks in the form of an integral of a known function, obtained from a so-called area-Mach number relation given by GSD. Hornung et al. [58] found that the solution based on GSD gives a very good approximation, graphically indistinguishable from the general solution of Ponchaut [85]. The great advantage of this approach is that the value of γ is directly included in the area-Mach number relation resulting in a simple determination of $\alpha = f(\gamma)$ dependence.

Experimental investigations of the power-law behavior of the converging shocks are more scarce. Dennen and Wilson [35] were among the first researchers to verify Guderley's solution experimentally. They generated converging cylindrical shocks by a neat experimental setup using the exploding wire technique in a cylindrical geometry, shown in Fig. 3.10.

Schlieren images of the converging shocks were taken not as a sequence but for separate runs. Despite the irregularities seen on the converging shock fronts displayed in Fig. 3.11a, and the fact that schlieren images were taken for different runs, the authors were able to determine the average distance traveled by the shock from the initial shock position. The obtained experimental data was plotted along Guderley's similarity solution for a cylindrical shock with $\alpha = 0.834$ and is illustrated in Fig. 3.11b, showing a surprisingly good agreement.

The electric discharge technique was also used in experiments performed by Baronets [13], where cylindrical shocks in argon and xenon were created by induction discharges in a cylindrical chamber. Experimental values of α in argon and xenon ($\gamma = 1.66$) as function of the shock front velocity are shown in Fig. 3.12. For shock speeds less than 2000 m/s, the shock front trajectories are completely linear with $\alpha = 1$. In the strong shock limit when the speed of the shock front increases to about 6000 m/s, the value of α approaches the analytical value of 0.816.

In an experimental study by Matsuo and Nakamura [75, 76], cylindrically converging shocks, or rather blast waves, were produced by detonation of PENT (pentaerythritol tetranitrate) loaded over cylindrical surfaces. The PENT power explosion was initiated by exploding a copper wire attached to the PENT charge.

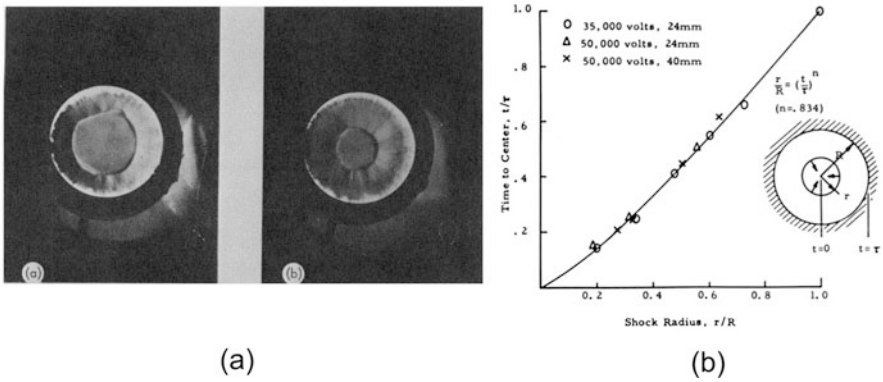

Fig. 3.11 (**a**) Converging shock fronts. (**b**) Experimental data vs Guderley's power-law solution, reproduced from [35], with permission from Springer

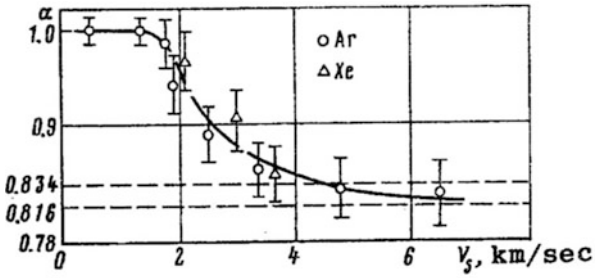

Fig. 3.12 Experimental value of the power-law constant α for various shock velocities, reproduced from [13], with permission from Springer

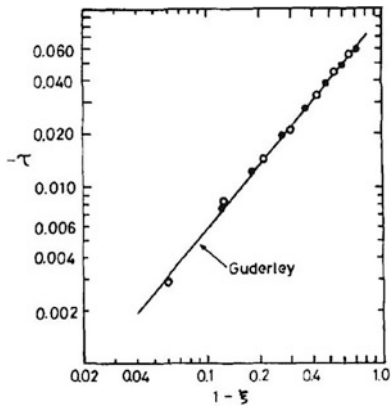

Fig. 3.13 Comparison of experimental data for shock front position vs time with Guderley's power-law solution, reproduced from [75], with the permission of AIP

Converging cylindrical blast wave fronts were traced by sequential framing camera images taken at 5 μs intervals. The results can be seen in Fig. 3.13 where shock fronts are plotted using dimensionless time, τ, and space variables, ξ, defined as $\tau = a_0 t / R_0$ and $\xi = (R_0 - R_s) / R_0$, where t, a_0, R_0, and R_s are time, sound speed, and radius at initial instant (subscript 0) and time τ (subscript s), respectively.

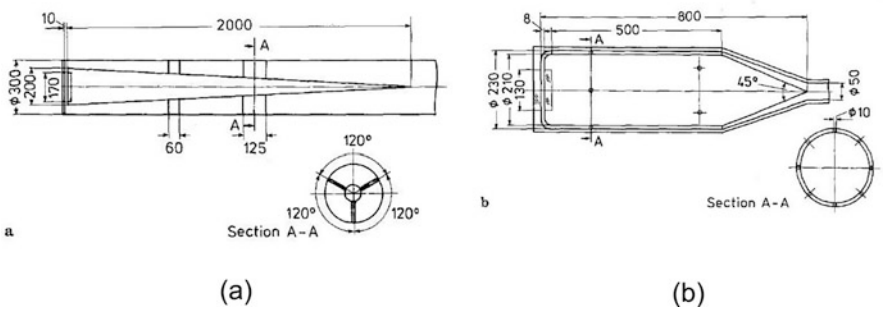

Fig. 3.14 Annular shock tubes at (**a**) RWTH Aachen and (**b**) Tohoku University, reproduced from [105], with permission from Springer

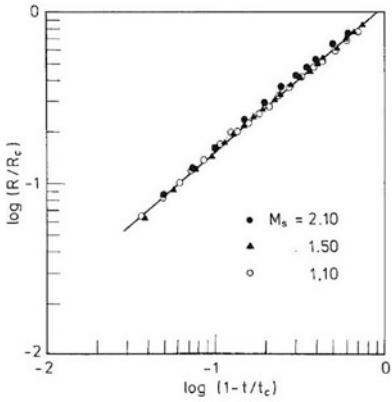

Fig. 3.15 Similarity exponents for various Mach numbers from experiments at Tohoku University, reproduced from [105], with permission from Springer

As one can see, there is an excellent agreement between Guderley's theory and experimental data. Unfortunately the authors do not present the value of α calculated from their experimental data.

Takayama, Kleine, and Grönig conducted an experimental study of converging cylindrical shock wave in air produced in annular shock tubes at Stoßwellenlabor, RWTH Aachen, and at Institute of High Speed Mechanics, Tohoku University, illustrated in Fig. 3.14a and b, respectively. The authors determined the experimental value of α in air ($\gamma = 1.4$) by doing least square fits to the streak camera recordings with initial Mach numbers varying from $M = 1.1$ to $M = 2.1$. Experiments were conducted both in Aachen and Sendai. Data obtained from experiments at Tohoku, Sendai, are shown in Fig. 3.15. Least square fit to data for initial Mach numbers $M = 1.1, 1.5$, and 2.1 provide values of $\alpha = 0.828, 0.829$, and 0.833, respectively. Corresponding experiments in at RWTH, Aachen gave $\alpha = 0.832\ (+0.028/-0.043)$ for $1.3 < M < 2.1$.

Measurements of the power-law exponent for the case of spherical shock convergence are even more elaborate than in the case of cylindrical geometry. The reason is obvious, since it is harder to visualize and access the data for a converging spherical shock front. Hosseini and Takayama [59] conducted a series

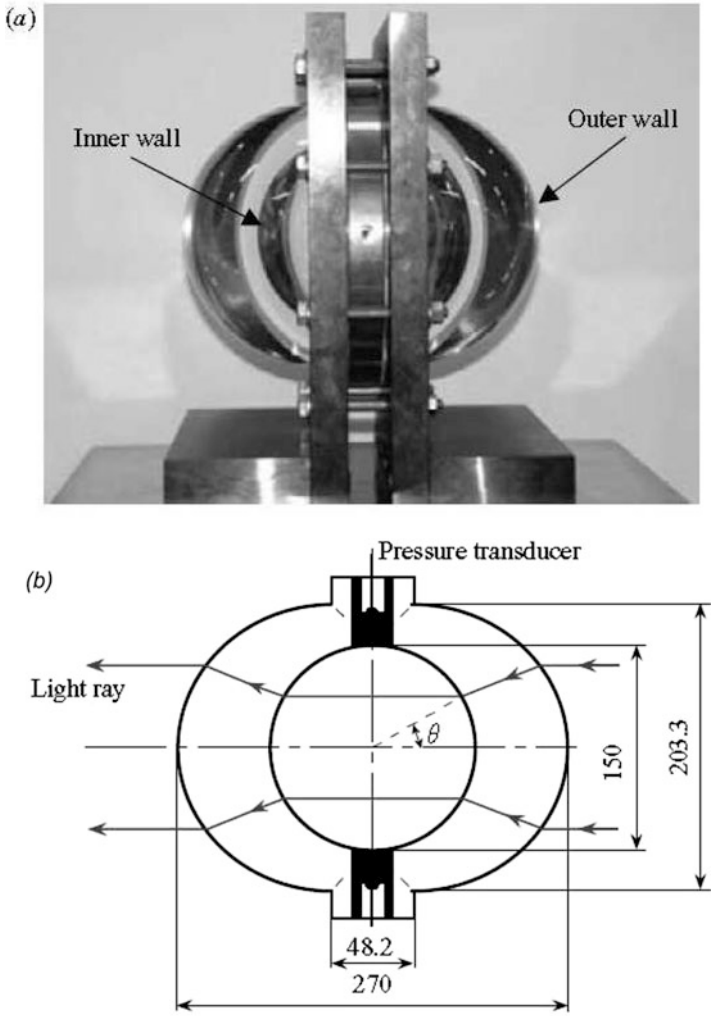

Fig. 3.16 Experimental setup (**a**) photograph and (**b**) schematic diagram, reproduced from [59], with permission from Cambridge University Press

of experiments in a spherical chamber. Shocks were produced at the center of the chamber by explosion of silver azide pellets. Shock visualization was possible due to a transparent aspheric lens-shaped test section producing collimated object beams. An image and schematic of the spherical test section is shown in Fig. 3.16.

Shock motion of initial outgoing as well as reflected converging shocks in the chamber was recorded by high-speed shadowgraph visualization giving shock front position as functions of time. Experimental data for converging shock fronts was compared to Guderley's similarity solution for spherical shocks, Fig. 3.17. A fit to experimental data gave a value of $\alpha = 0.738$ as compared with the theoretical value

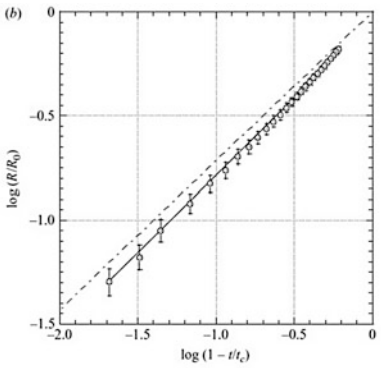

Fig. 3.17 Fit to experimental log–log plot of the converging shock radius versus the time measured relative to the arrival time of the shock at the center compared to Guderley theory $- \cdot -$, reproduced from [59], with permission from Cambridge University Press

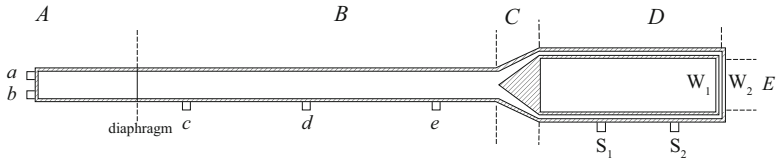

Fig. 3.18 Schematic of the shock tube. A, driver; B, inlet pipe; C, transformation section; D, annular channel; E, test section; W_1 and W_2, glass windows framing the test section, reproduced from [67], with the permission of AIP

of $\alpha = 0.717$ indicating that experimental shock fronts converged slower than the convergence rate predicted by theory. The authors attribute this to the fact that the reflected shocks converge in the outgoing flow field produced by the initial diverging blast wave.

Kjellander, Tillmark, and Apazidis [67] investigated experimentally the value of the power-law constant α in Guderley's solution as function of the adiabatic exponent γ. Three different gases were considered: argon (Ar, $\gamma = 1.66$), nitrogen (N_2, $\gamma = 1.40$), and propane (C_3H_8, $\gamma = 1.13$). The main idea was to obtain the value of a power-law exponent for converging cylindrical shocks in various gases having different values of the adiabatic exponent γ. The goal was to capture the variation of the power-law exponent α with the adiabatic constant γ in the same shock tube facility at KTH, Stockholm. The schematic of the shock tube is illustrated in Fig. 3.18.

Numerical calculations were performed in order to assess the influence of the sharp 90 degree corner connecting the annular section with the test section of the shock tube. The purpose was to obtain an understanding of the process of stabilization of the converging shock to a plane shock front after entering the test section from the sharp corner. The results are illustrated in Fig. 3.19. As one can see, the shock front stabilizes to a plane form about one third of the radial distance from the center. The dashed line in the figure marks the location from where the measurements were performed. Three different test gases were used: propane (C_3H_8, $\gamma = 1.13$), nitrogen (N_2, $\gamma = 1.40$), and argon (Ar, $\gamma = 1.66$).

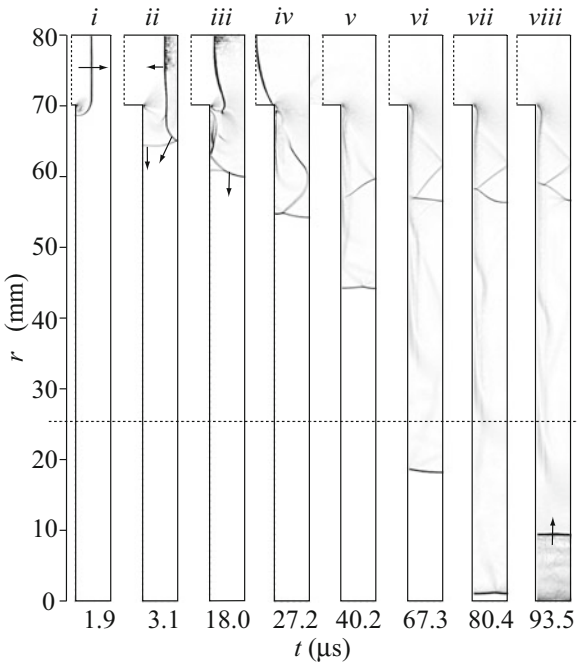

Fig. 3.19 Numerical schlieren images of shock propagation in the test section after the sharp 90 degree turn from the annular section, reproduced from [67], with the permission of AIP

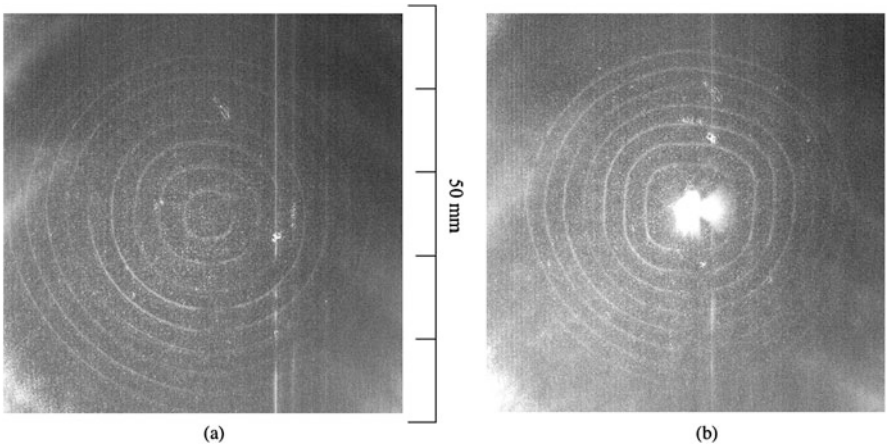

Fig. 3.20 Multiple exposure images for converging shocks in argon at two different initial Mach numbers: (**a**) $M = 1.9 \pm 0.01$ and (**b**) $M = 2.4 \pm 0.01$, reproduced from [67], with the permission of AIP

Multiple exposures of converging shock fronts in argon for two different initial Mach numbers are illustrated in Fig. 3.20.

The light flash at the center of the test section at the instant of implosion may be clearly seen in Fig. 3.20b showing a sequence of converging shock fronts in argon. The successive shock front positions were processed numerically to obtain the value

Table 3.1 Values of the self-similar exponent α acquired from [67]: comparison with analytical work and previous experiments

γ	α, Analytical other authors	α, Experimental other authors	α, Kjellander [67],
1.13	0.8778 from [72]		0.88 ± 0.02
1.40	0.8353 from [72]	0.831 ± 0.002 from [105]	0.84 ± 0.01
1.66	0.8156 from [72]	0.820 to 1.0 from [13]	0.81 ± 0.01

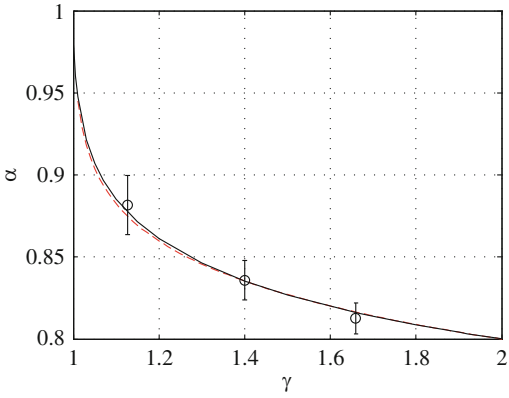

Fig. 3.21 Acquired experimental values and standard deviation of α compared to the analytical solution (full line; values from Ref. [72]) and geometrical shock dynamics (dashed line), reproduced from [67], with the permission of AIP

of the average radius for each shock front. The values of the power-law exponent were then determined by curve fitting to self-similar paths, and the results are listed in Table 3.1 [67].

Based on the experimental values, Fig. 3.21 shows the variation of the power-law exponent α as function of the adiabatic exponent γ for different gases.

See Table 3.2 for additional self-similarity exponents obtained to date.

3.4 Stability of Converging Shocks

As we mentioned in the previous sections, the pioneering experimental work of Perry and Kantrowitz [84] and other early researchers produced a road map for further studies of converging shocks. One of the most important questions raised by these researchers was the question of stability of the converging shocks. In their own study, Perry and Kantrowitz introduced an artificial disturbance on the path of the converging shock. They observed that the influence of the disturbance resulted in shifting the center of convergence from the center of the test section closer to the location of the disturbance. But will the shock front remain mainly circular or at least not break up during the further motion of the converging shock? This question is pivotal for the ability of the converging shock to produce extreme conditions in the compressed gas. If the shock front can retain some symmetry and remains bounded by a smaller and smaller area, then various portions of the shock front will arrive

Table 3.2 Summary of self-similarity exponents for converging cylindrical and spherical shock waves for two different adiabatic gas constants

	Cylindrical $\gamma = 7/5$	Cylindrical $\gamma = 5/3$	Spherical $\gamma = 7/5$	Spherical $\gamma = 5/3$
Guderley [52]	0.834	–	0.717	–
Butler [18]	0.835217	–	0.717173	0.688377
Stanyukovich [100]	0.834	–	0.717	–
Welsh [116]	0.835323	0.815625	0.717174	0.688377
Lazarus & Richtmyer [73]	0.83532320	0.81562490	0.71717450	0.68837682
Mishkin & Fujimoto [79]	0.828	0.814	–	–
de Neef & Hechtman[a] [33]	0.835 ± 0.003	–	–	–
Van Dyke & Guttman [108]	0.835324	–	0.7171745	0.6883768
Nakamura [81]	0.8342, $M_s = 4.0$	–	0.7173	–
	0.8345, $M_s = 10.0$			
Kleine[a] [69]	$0.832 + 0.028, -0.043$			
Takayama[a] [105]	0.831 ± 0.002	$M_s = 1.1 - 2.1$		
Hafner [54]	0.835323191952911	0.815624901431225	0.717174501488999	0.688376822922543
Chisnell [27]	0.83532	0.81562	0.71716	0.68837
Hosseini & Takayama[a] [59]	–	–	0.738	
Ponchaut et al. [85]	0.835323191953	0.8156229691667	0.717174501488	0.6883740859496
Kjellander et al.[a] [67]	0.84 ± 0.01			
Ramsey et al. [88]	0.835323192	0.815624901	0.717174501	0.688376823

[a]Results obtained by experiments

almost simultaneously to a small focal region and compress the engulfed gas to high pressures and temperatures. If, on the other hand, the shock front will undergo a large distortion or even break up, then this effect of focusing will of course be lost.

The question of shock stability is therefore of pivotal importance for the ability of the converging shock to generate extreme conditions at the center of convergence, in the focusing region. This question has over the years been addressed many times and by a large number of researchers. Many of those used the theory of geometrical shock dynamics (GSD) also called CCW theory by the names of the researchers who developed it in the middle of the last century, namely, Chester [23], Chisnell [25, 26], and Whitham [117]. We have already mentioned the GSD theory in the previous section where we discussed the self-similarity solution for converging cylindrical and spherical shocks. A large number of researchers have been using this approximate theory presenting a more simple alternative to a full set of Euler equations to describe shock propagation in various geometries. This theory describes the shock propagation along the rays normal to the shock front and because of its clear geometrical interpretation of shock motion gives a useful insight in the physical properties of advancing shocks. Although GSD is an approximate theory that disregards flow conditions behind the moving shock front, it gives surprisingly accurate results in a broad range of flow configurations, especially for accelerating shocks. Let us here get acquainted with some basic ideas of this theory.

The main idea of GSD is to consider flow along the tube with slowly varying cross-section as illustrated in Fig. 3.22. The tube wall is built by the rays normal to the surface of the shock. The continuity, momentum, and thermodynamic relation for isentropic flow averaged over the cross-section area of the tube take the form:

$$\frac{\partial \rho}{\partial t} + u\frac{\partial \rho}{\partial x} + \rho\frac{\partial u}{\partial x} + \rho u\frac{1}{A}\frac{dA}{dx} = 0, \tag{3.2}$$

$$\frac{\partial u}{\partial x} + u\frac{\partial u}{\partial x} + \frac{1}{\rho}\frac{\partial p}{\partial x} = 0, \tag{3.3}$$

$$\frac{d\rho}{dt} = \frac{1}{a^2}\frac{dp}{dx}. \tag{3.4}$$

Here, ρ, p, u, and a denote density, pressure, velocity, and sound speed, respectively, averaged over the cross-section $A(x)$ of the tube with x being the direction along the tube axis. Introducing Eq. (3.4) into (3.2) and multiplying the sum by a/ρ, we get

$$\frac{1}{\rho a}\left[\frac{\partial p}{\partial t} + u\frac{\partial p}{\partial x}\right] + a\frac{\partial u}{\partial x} + au\frac{A'}{A} = 0. \tag{3.5}$$

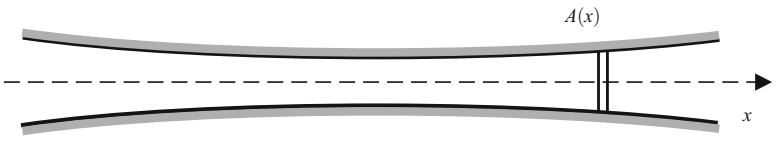

Fig. 3.22 Tube with slowly varying cross-section used in GSD theory

Upon adding the last equation with (3.3), we obtain

$$\frac{1}{\rho a}\left[\frac{\partial p}{\partial t}+(u+a)\frac{\partial p}{\partial x}\right]+\left[\frac{\partial u}{\partial t}+(u+a)\frac{\partial u}{\partial x}\right]+au\frac{A'}{A}=0. \tag{3.6}$$

The last equation is transformed to an ordinary differential equation along the path

$$\frac{dx}{dt}=u+a, \tag{3.7}$$

which is the C_+ characteristic and the resulting system of quasi one-dimensional balance equations is combined in a single ordinary differential equation

$$\frac{dp}{dx}+\rho a\frac{du}{dx}+\frac{\rho a^2 u}{u+a}\frac{1}{A}\frac{dA}{dx}=0. \tag{3.8}$$

This equation together with the jump relations over the shock interface for velocity

$$u=a_0\frac{2}{\gamma+1}\left(M-\frac{1}{M}\right), \tag{3.9}$$

pressure,

$$p=\rho_0 a_0^2\left(\frac{2}{\gamma+1}M^2-\frac{\gamma-1}{\gamma\,(\gamma+1)}\right), \tag{3.10}$$

and density,

$$\rho=\rho_0\frac{(\gamma+1)\,M^2}{(\gamma-1)\,M^2+2}, \tag{3.11}$$

result in the so-called area-Mach number relation along the tube given by

$$g(M)\frac{dM}{dx}+\frac{1}{A}\frac{dA}{dx}=0, \tag{3.12}$$

with γ denoting the usual adiabatic index, M, Mach number and $g(M)$ being a known function of the Mach number [120]. Strictly speaking Eq. (3.8) is valid only on the C_+ characteristic given by Eq. (3.7), which may deviate from the rays perpendicular to the shock front and building the walls of the tube. This deviation is due to the nonuniform flow behind the shock. This means that the characteristic rule disregards the conditions behind the shock. Although presenting an approximate description, this theory gives a simple, elegant, and physically insightful approach to shock wave propagation. It has also proven to be surprisingly accurate in predicting propagation of accelerated shocks and thus very useful for treating converging

shocks. An accelerating shock nearly "escapes" the nonuniform flow conditions behind the shock front and is therefore less affected by those. This theory, when applied to a converging cylindrical or spherical shock wave, gives a very simple as well as accurate description of the convergence process. It gives, for example, an extremely good approximation of Guderley's exact solution [52].

In 1957 Whitham [117] described this theory as applied to two-dimensional shock propagation. He was also the first to apply it to the important question of plane shock stability. He considered first the propagation of a plane shock moving along a wall and studied the decay of a small disturbance in the form of a small bump on the wall. For a shock normal to the wall, the bump will result in a formation of an "N-wave." It was also found that the stability decreases with increasing Mach number [117]. Whitham considers two important wedge-shaped shock configurations. One generated by a convex forward piston and the other by concave forward piston as seen from Fig. 3.23. These two configurations are generic for propagating strong shocks. If the shock has already obtained the form of the piston described here, the next shock position will be determined by the process illustrated in Fig. 3.23. In the case of convex forward configuration, the next shock front emanating from the

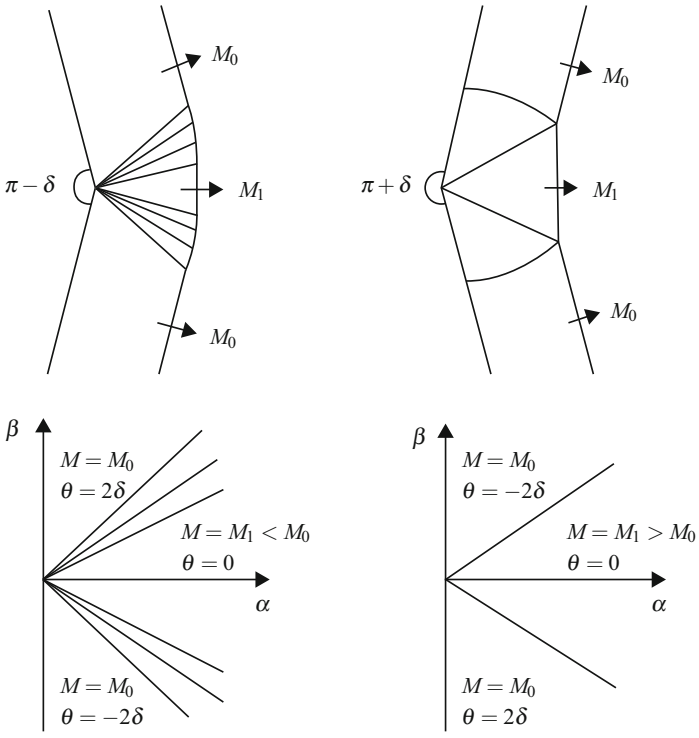

Fig. 3.23 Shock wedge patterns, original figure reproduced from [117], with permission from Cambridge University Press

corner will be built by two centered simple waves, while for the concave forward configuration, the solution from the corner is given by two shock-shocks, building a Mach stem with a new, higher Mach number. This is the process that governs the convergence of polygonal shocks described later in this chapter. In the concluding section of this fundamental work, the author considers the stability of converging cylindrical shocks. He argues that in this situation, it is sufficient to consider the case of strong shocks since all converging cylindrical shocks ultimately become strong. The author uses hodograph transformation to find out whether a small deviation of the cylindrical shape will increase or decrease during convergence. He deducts that as the shock contracts, the harmonics will dominate the symmetrical mode and comes to a conclusion that the shock ultimately becomes unstable.

The geometrical interpretation of GSD formulated mainly by Whitham [117, 118, 120] gives a simple and useful interpretation of shock propagation. This geometrical picture describing propagation of a shock front along the rays perpendicular to the surface of the shock by means of locally quasi one-dimensional ordinary differential equation makes it especially useful for performing shock front stability analysis. A number of researches have successfully applied this theory to study the stability of converging shocks both numerically and analytically.

Ahlborn and Fong [1, 47] investigated the stability of converging shocks both analytically and numerically. Their numerical method was based on the theory of GSD. They introduce mesh points along the shock front and obtain a system of ordinary differential equations describing the shock front propagation along the rays normal to the shock front. The authors introduce various types of initial perturbations of the cylindrical shock and investigate how these instabilities evolve in the process of shock convergence. They consider several geometric parameters as a measure of perturbation magnitude, such as the ratio of local increase of the shock radius to the average shock radius $\Delta r/r$, ratio of the corresponding area perturbation to the average segment area $\Delta A/A$, as well as the deviation of the local normal angle from the radial direction δ, which are all shown in Fig. 3.24. The authors define absolute stability of a shock if all of these parameters go to zero before the collapse of the shock and as partial stability if their values tend to some small value much less than 1. They finally map stability regions for various types of perturbations for various values of the initial Mach number. The findings of these researchers are thus in some contradiction with the results of Whitham [117], who concluded that all converging shocks are ultimately unstable. The reason for this contradiction is that the work of Fong and Ahlborn [47] is restricted by the linear stability analysis.

Gardner, Book, and Bernstein [49] represent another team of researchers who considered the problem of converging shocks. They used the GSD (or CCW) theory to develop an analytical and computational model to address the question of stability of converging cylindrical and spherical shocks. They present their work as an extension of [47] to smaller radii including the analysis of nonlinear behavior.

Evans [45] is yet another researcher who addressed the stability of converging spherical shocks on the basis of GSD. He investigates convergence of a nearly spherical shock in van der Waals gas analytically. His research is motivated by the implications of stability analysis on the problem of sonoluminescence. The author conducts a first-order perturbation analysis on the solution of converging spherical

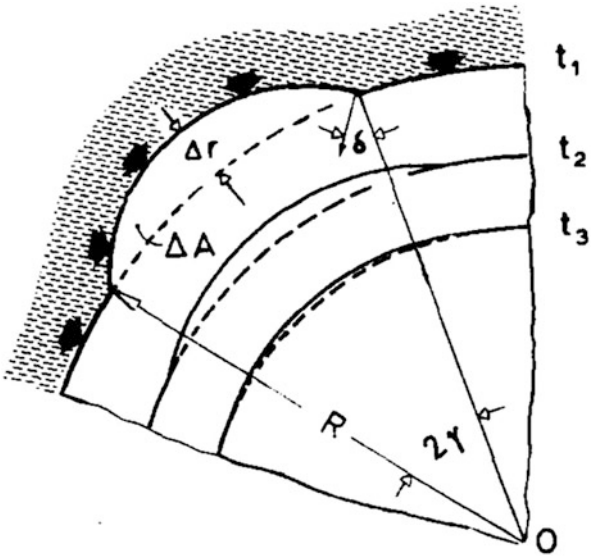

Fig. 3.24 Geometric parameters of shock front perturbation, reproduced from [47], with the permission of AIP (Phys. Fluids 22(3), 416–421 (1979)

shock front according to GSD. He obtains an ordinary differential equation for the radial component of the disturbance $\mu(r)$ with a simple exponential solution $\mu(r) = r^{\xi}$ where ξ is the function of flow parameters. He was then able to calculate the size of perturbation divided by the radius, $\delta r/r$, and finally find that as the spherical shock converges, the relative deviation from the spherical form increases both in amplitude and frequency as can be seen from Fig. 3.25.

The final conclusions of this investigation are that the converging spherical shock in van der Waals gas is unstable, meaning that a small initial perturbation of the spherical form will grow and eventually destroy the initial spherical symmetry of the shock. The instability is, however, weak with slow rate of increase in disturbances being proportional to the inverse power of the radius. These findings are as we see in agreement with the conclusions of the initial study by Whitham [117].

In a short but very informative experimental investigation by Wu et al. [122], the authors study the stability of converging cylindrical shocks. Artificial perturbations of the flow field were introduced by removing the wedge fairings from the shock tube support flange webs. The four rectangular webs introduced perturbations of the flow field transforming an initially cylindrical shock front to a square-like shock as it approached the center of the test section. The authors also considered perturbation of the shock front by a single cylindrical rod.

The group of Takayama [105] was the next group of researchers who investigated the question of stability in a series of experimental studies. These researchers observed what they called "instability modes" produced in the converging shock front in their experimental facilities. This study reported the results of a series of experiments conducted in two experimental facilities: the first one at Stosswellenlabor, RWTH Aachen and the second at Institute of High Speed Mechanics,

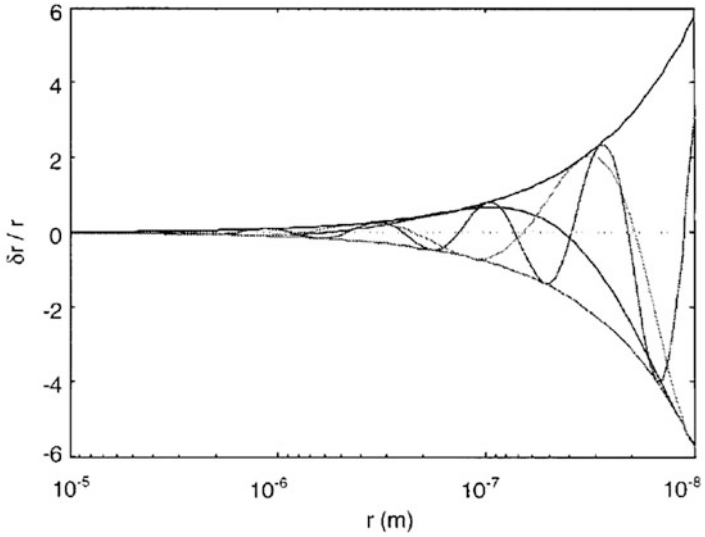

Fig. 3.25 Growth of relative perturbation of the converging spherical shock front, reproduced from [45], with the permission of AIP

Tohoku University, Sendai. Both shock tube facilities had a central body inserted in a cylindrical shock tube that transformed the plane shock to an annular ring. They found that the initially cylindrical shock front was distorted in both facilities. In the first facility shock fronts with triangular symmetries were formed, while in the second facility, the initially cylindrical shock was transformed to a front with quadrangular symmetries. The imaging was done by holographic interferometry and revealed not a chaotic breakup of a shock front but on the contrary very symmetric and beautiful structures that the researchers called three- and four-instability modes, respectively, as seen in Fig. 3.26. There are two other important features that can be observed in this image. In Fig. 3.26b we can see the transformation of an initially cylindrical shock to an almost perfect square with a rounded corners and plane sides. The second feature, also seen in this image, is the "rotation" of a larger square to a smaller one in the center. This 90 degree "rotation" placing corners of the new small square opposite to the centers of the plane sides of the larger square is in reality a periodic transformation that the square form of the shock undergoes during convergence. This tendency of converging shocks to build polygonal structures with plane sides and corners brings us to the next question. Can this property be used to enhance the symmetry of the converging shock? We will address this question later in this section.

Let us here continue with the overview of other experimental and numerical studies in this area as the study by Watanabe and Takayama in 1991 [114]. The experiments were carried out in the annular shock tube facility at Tohoku University. The co-axial annular shock tube similar to that used by Perry and Kantrowitz was

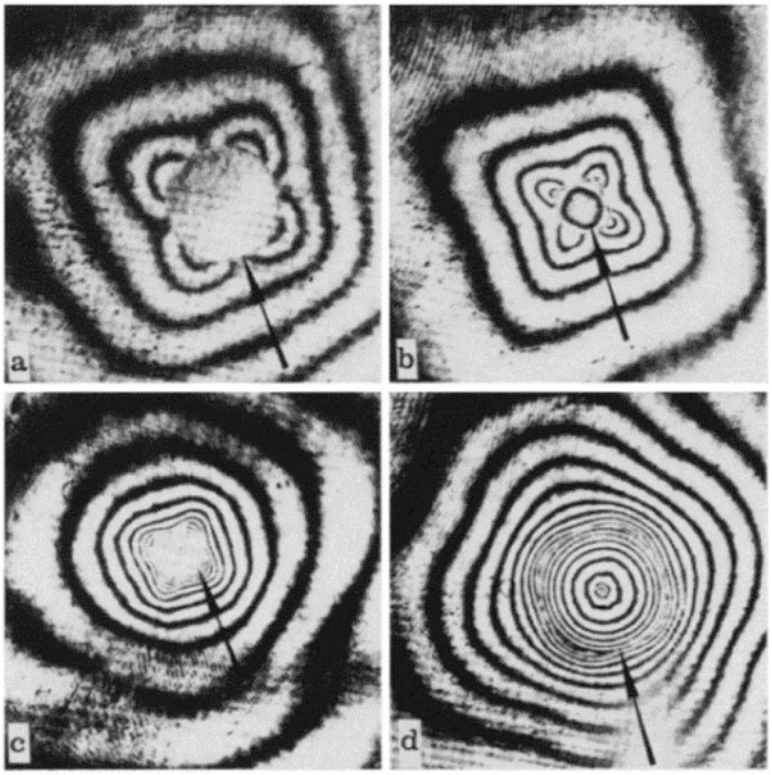

Fig. 3.26 Holographic interferograms of converging cylindrical shock waves, reproduced from [105], with permission from Springer

able to transform an initially plane shock to a converging cylindrical. The visualization of converging shock fronts was conducted by double exposure holographic interferometry. The inner central body of the transformation section was supported by four struts. Shock waves with initial Mach numbers in the range $M = 1.1$–2.0 were investigated. One of the main findings of this study was that although the initial influence of the disturbances caused by the supporting struts was initially small, it was amplified as the shock strength increased in the process of convergence and finally was dominating the shape of the shock transforming it from cylindrical to a nice symmetric square with rounded corners as can be seen in Fig. 3.27.

This study confirmed once again that even a small initial perturbation in the flow will be amplified for a converging shock as the shock strength increases and will become a decisive factor dominating the transformation of the converging shock front.

In order to eliminate the flow disturbances caused by the supporting struts of the central body, a series of experiments were conducted by Watanabe, Onodera, and Takayama in a vertical annular shock tube with no supporting struts [115].

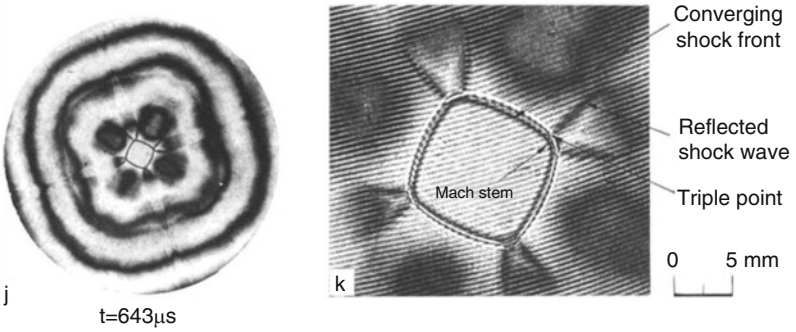

Fig. 3.27 Transformation of initially cylindrical to a square shock, reproduced from [114], with permission from Springer

The main findings of these experiments were that for weaker initial shocks with Mach number in the range $M = 1.51$, the cylindrical shock preserved its symmetry through convergence and even after reflection from the center of convergence. When the strength of the initial shock was increased to $M = 2.0$, the converging shock was still symmetric, while irregular vortices were observed for the reflected shock in the vicinity of the center. It was concluded that for stronger shocks, the initial disturbances, in this case caused by small changes in the clearance of the co-axial channel, were amplified making the converging cylindrical shock unstable.

3.5 Polygonal Shocks

3.5.1 Stability of Polygonal Shocks

One of the main results of the experimental study by Takayama and co-workers [105] was the ability of the square shock once it was formed to retain its square structure. Although the polygon is seen to rotate, its square form is preserved. In [105] we see just one "rotation" of the initially generated square to a new, smaller one which is "rotated" 90 degrees as compared to the initial. Is this transformation stable, and if so will it continue during a further convergence process?

A theoretical study by Schwendeman and Whitham [94] gives answers to these questions. The authors use a ray theory of geometrical shock dynamics (GSD) to investigate the properties of converging polygonal shock structures. As we have discussed in the previous section, Whitham [117] used this theory to show that the converging cylindrical shock is unstable to small disturbances. In the quoted article, the authors show that a regular polygon can be analyzed exactly by means of the GSD. The results describe a periodic transformation of a regular polygon structure in which a new polygon with the same number of sides n but rotated by an angle π/n relative to the older is created at regular intervals. Above that, the Mach number

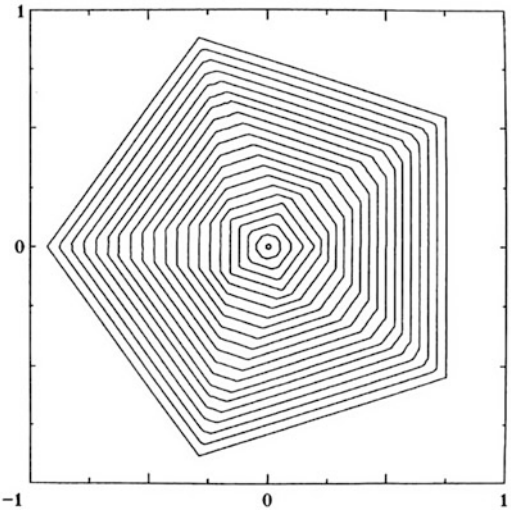

Fig. 3.28 Converging pentagonal shock, reproduced from [94], with permission from the Royal Society

of the converging polygonal structure calculated at the end of each interval increases in exactly same way as for converging cylindrical shock.

Figure 3.28 shows a process of convergence for a polygonal shock with five sides. Numerical calculations of this shock convergence were done by means of the numerical scheme based on GSD and developed by Henshaw et al. [56]. The numerical procedure is based on approximating the shock front by a discrete set of points $\mathbf{r}_k(t), \quad k = 1, \ldots, N$ and then integrate a system of ordinary differential equations

$$\frac{d}{dt}\mathbf{r}_k(t) = M_k(t)\mathbf{n}_k(t), \quad k = 1, \ldots, N, \tag{3.13}$$

where $M_k(t)$ and $\mathbf{n}_k(t)$ are the local Mach number and normal to the shock front. This scheme allows for propagation of the shock front along the rays normal to the shock front. The value of the Mach number at a new shock front position is then calculated by means of the Area-Mach number relation

$$\frac{A_k(t)}{A_k(0)} = \frac{f\,(M_k(t))}{f\,(M_k(0))}, \quad k = 1, \ldots, N, \tag{3.14}$$

supplied by the theory of geometrical shock dynamics.

An example of such calculations is displayed in the abovementioned Fig. 3.28. One can here see the rotation of the initial pentagon to a new one by an angle of 36°. This "rotation" is in reality a process of a continuous transformation of the initial pentagon. This transformation arises as a result of Mach reflection at the corners of the polygon, where a Mach stem is created opposite to the corner. The value of the Mach number on the newly created Mach stem is higher than on the

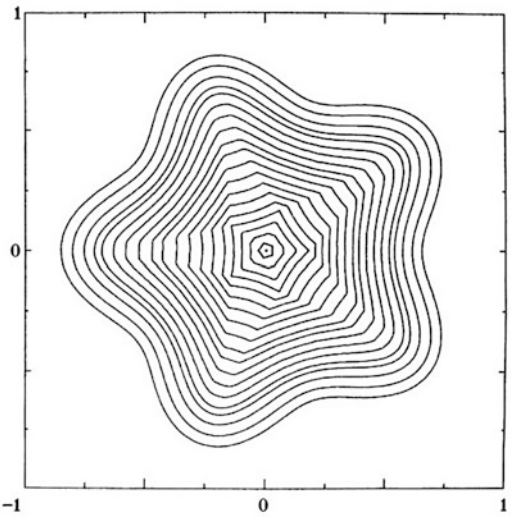

Fig. 3.29 Converging symmetrically perturbed pentagonal shock, reproduced from [94], with permission from the Royal Society

adjacent sides of the polygon giving it a higher speed of propagation which leads to an increase of its length. This process is completed when the newly created Mach stems completely absorb the older sides of the polygon and meet at a new corner. At this instant the new polygon with a higher Mach number is formed. The corner of the new polygon is located right opposite to the midpoint of an older polygon side and thus the whole structure seems to be "rotated" by π/n. The value of the Mach number of the new polygon is increased exactly as for the corresponding converging cylindrical shock. After that, the process is repeated. To understand the robustness of this transformation process, the authors further investigate convergence of polygonal shocks with symmetric perturbation of the form like a perturbed pentagonal structure shown next in Fig. 3.29.

One can here see that the initial and strong—albeit symmetric—perturbation of the polygonal form is eventually suppressed and flattened out resulting in pentagons with increasingly flatter sides. Here as the shock strength increases, its tendency to planarity becomes dominating. In this sense this procedure of converging symmetric polygonal shocks provides a very attractive alternative to cylindrical convergence. On the one hand, it is stable and robust, and on the other hand, it gives the same amplification of the shock strength! Well if symmetric polygonal shocks are so good, how can one create them in practice? We will address this question in the next section.

3.5.2 Generation of Polygonal Shocks by Reflection

Apazidis and Lesser [8] investigated theoretically the possibility to generate symmetric converging polygonal shocks by reflection from smooth reflectors of appropriate shape. Reflector shapes are chosen as a perturbation of a cylindrical shape to

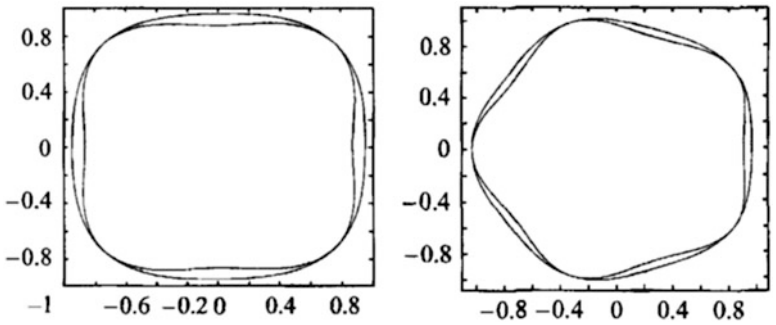

Fig. 3.30 Reflector boundaries and fully reflected shocks for $n = 4$ and $n = 5$, reproduced from [8], with permission from Cambridge University Press

a smooth polygonal shape with, e.g., four, five, six, and eight sides. The reflector boundary can be described by an equation of the form

$$r = \frac{1}{1 + \varepsilon \cos(n\theta)}, \tag{3.15}$$

which describes a perturbation of a circular boundary using a cosine function with a small parameter. Examples of two such reflector boundaries with fully formed reflected shocks for $n = 4$ and $n = 5$ are given in Fig. 3.30.

The numerical procedure used in this investigation is based on the modified version of the GSD. This modified version takes into account the nonhomogeneous conditions created by the flow ahead of the advancing shock. The initial outgoing and expanding from the center of the chamber shock creates a flow field ahead of the reflected shock converging in the opposite direction toward the center of the chamber. The main idea is to transform the governing equations to a coordinate frame (x', y') in which the medium ahead of the advancing shock is locally at rest. This locally Galilean transformation is given by

$$x = x' + U(x, t)t, \quad y = y' + V(x, y)t, \quad t = t', \tag{3.16}$$

where $U(x, t)$ and $V(x, t)$ are the local components of the flow velocity. The usual form of GSD with quiescent conditions ahead of the shock is then valid in this frame. Obtaining the relations between the variables in the fixed and moving frames results in the a transformation of the flow variables with modified expressions for the Mach number and area in Eqs. (3.18) and (3.14) as well as in the direction of propagation which is now along the rays not necessarily normal to the shock front. One of the results of this transformation gives the relation between the cross-section areas and unit vectors guiding the direction of shock propagation and takes the following form

$$A = A'(\mathbf{e} \cdot \mathbf{n}), \tag{3.17}$$

where A' and $\mathbf{e}$ are the tube area and unit vector along the ray direction in the moving frame and A and $\mathbf{n}$ corresponding quantities in the fixed frame [8]. Thus, as shown earlier by Whitham [119], A' is the area cut out by the ray tube, and A is the normal cross-section.

The numerical procedure is similar to that used in [94] and is based on approximating the shock front by a discrete set of points $\mathbf{r}_k(t), \quad k = 1, \ldots, N$ and then integrating a system of ordinary differential equations

$$\frac{d}{dt}\mathbf{r}_k(t) = M_k(t)\mathbf{e}_k(t), \quad k = 1, \ldots, N \tag{3.18}$$

with $\mathbf{e}_k$ being the unit vector along the ray that describes the shock path when it is moving into a nonuniform region. In order to calculate $\mathbf{e}$ as well as the Mach number M' in the moving frame, it is necessary to have the expressions for the oncoming flow field and suitable gradients of this field. In [8] this is accomplished by using the blast wave solution for a cylindrically symmetric explosion.

The results of calculations show the formation of polygonal shocks by reflection from smooth square, pentagon, hexagon, and octagon—like reflector boundaries given by Eq. (3.15). In these calculations the initial outgoing shock is given by the cylindrical blast wave from the center of the chamber. Initially smooth shock profiles resembling the reflector form are seen to gradually form flat sides and sharp corners transforming into a real polygon; see Fig. 3.31.

The influence of the flow ahead of the converging shock is also investigated. It is shown that the flow ahead enhances the formation of the polygonal form as well as the strength of the converging shock. Since the flow ahead is symmetric, it preserves the symmetry of the converging shock. Figure 3.32 shows the Mach number along converging shock fronts as well as the tendency to planarity of the shock front and corresponding Mach number with initially smooth distribution replaced by a stepwise with increasing shock strength. The lower Mach number curve corresponds to the reflected shock close to reflector boundary and the upper curve to the converging shock front approaching the center of reflector.

These ideas were realized in practice experimentally by Johansson, Apazidis, and Lesser in 1999 [60]. One of the main purposes of this work was to produce symmetric converging polygonal shocks experimentally. A two-dimensional test section with a reflector boundary described by Eq. (3.15) with $n = 5$ and $\varepsilon = 0.035$ was manufactured. The average radius of the boundary was 80 mm and the height of the test section was 5 mm. The upper and lower test section walls were made of 15 mm thick glass plates for flow visualization realized by a schlieren system with a still camera and flash unit connected to a time measuring and controlling equipment for initiation of single or double flash pulses. The initial outgoing shock was generated by an electric discharge device with a 0.3 μF capacitor. The exact time interval between the initial released shock and the time for the flash was provided by a photodiode connected to an oscilloscope detecting both the light from the electric discharge and the flash unit. The boundary of the chamber with two initial cylindrical outgoing shocks just before reflection may be seen in Fig. 3.33.

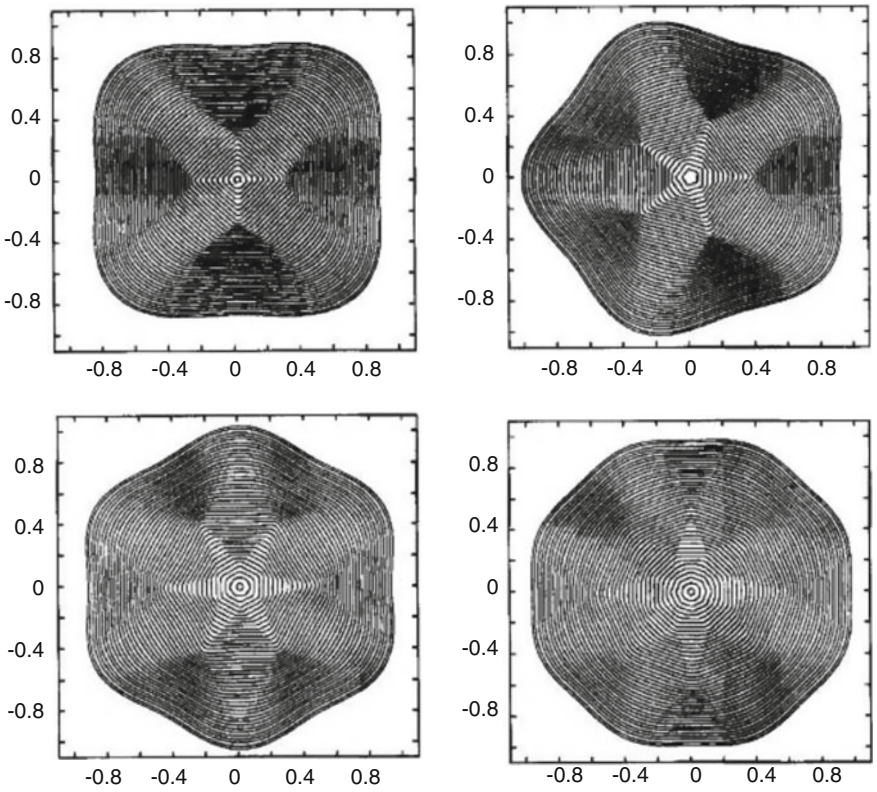

Fig. 3.31 Converging polygonal shocks, reproduced from [8], with permission from Cambridge University Press

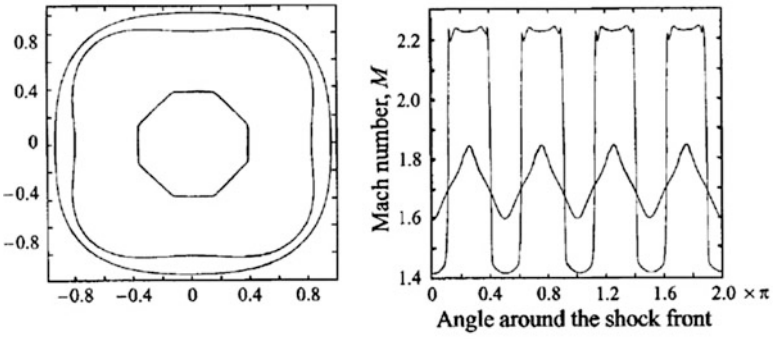

Fig. 3.32 Mach number distribution along the converging polygonal shock front, reproduced from [8], with permission from Cambridge University Press

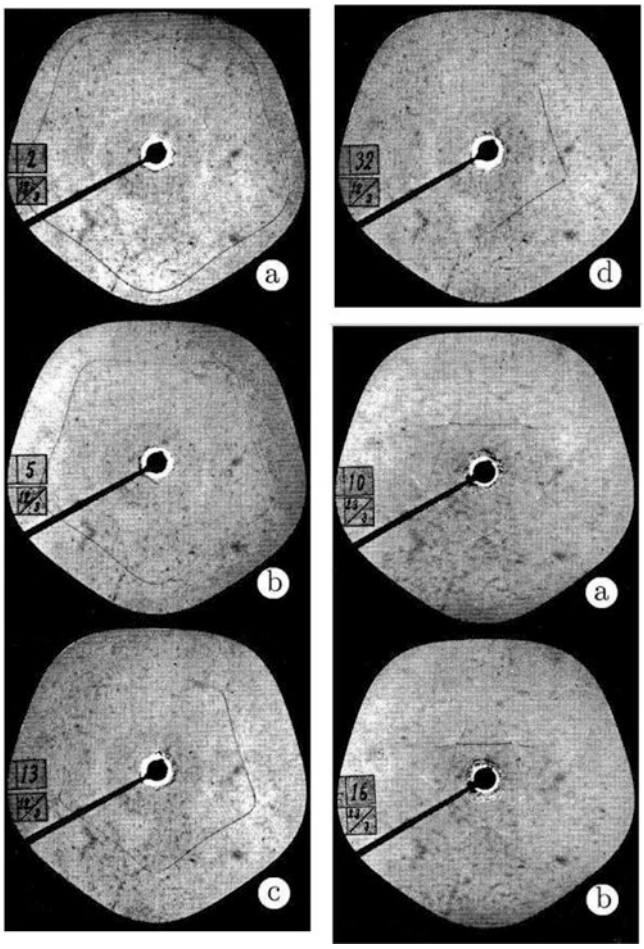

Fig. 3.33 Creation of polygonal shocks by reflection, reproduced from [60], with permission from Elsevier

The Mach number near the reflector boundary was measured to $M = 1.1$ classifying the shocks as weak and thus having weak shock behavior such as formation of caustics with shock crossing at the corners of the polygonal structure as may be seen in Fig. 3.34.

The shock strength was increased in a follow-up study using the same chamber but with a different method of shock generation, namely, exploding wire technique [9]. A thin copper wire, connected to the electrodes, was placed at the center of the chamber. A triac device triggered discharges leading to rapid Joule heating, melting, and vaporizing the copper wire and thus creating an outgoing cylindrical blast wave in air. The photograph of the test section with the exploding wire setup and smooth pentagonal reflector boundary is shown in Fig. 3.35.

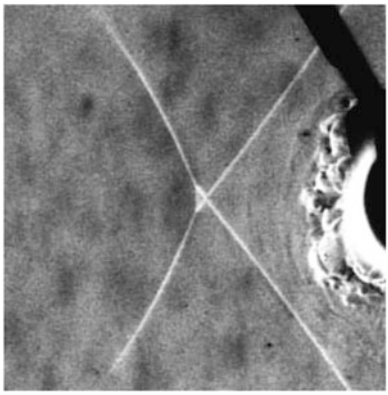

Fig. 3.34 In the case of weak shocks the traces of shock-shocks cross and form a triangular shape in the form of a caustic as shown here, reproduced from [60], with permission from Elsevier

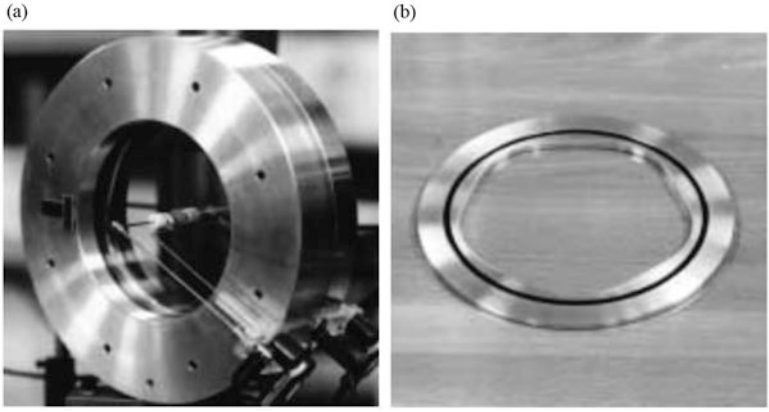

Fig. 3.35 Image of (**a**) the test section with exploding wire setup at the center and (**b**) reflector boundary, reproduced from [9], with permission from Springer

By this method the authors were able to create shock waves in the range of $M \sim 1.5$–2.0. The higher strength of the initial shocks resulted in the nonlinear behavior of converging shocks after reflection from the boundary. The shock crossing with caustic formation for weak shocks was now replaced by the formation of Mach stems at the corners of the polygon, as may be seen from Fig. 3.36a. The Mach number is higher on the Mach stems as compared to the adjacent sides of the polygon leading to a transformation of the polygonal structure as described previously.

Figure 3.36b shows experimental image and comparison with computations based on the extended theory of GSD, taking into account flow ahead of the converging shock and created by the initial outgoing blast wave [8]. The GSD theory is seen to be able to reproduce the converging shock front in good agreement with the experiment. The flow details behind the converging shock front are however not

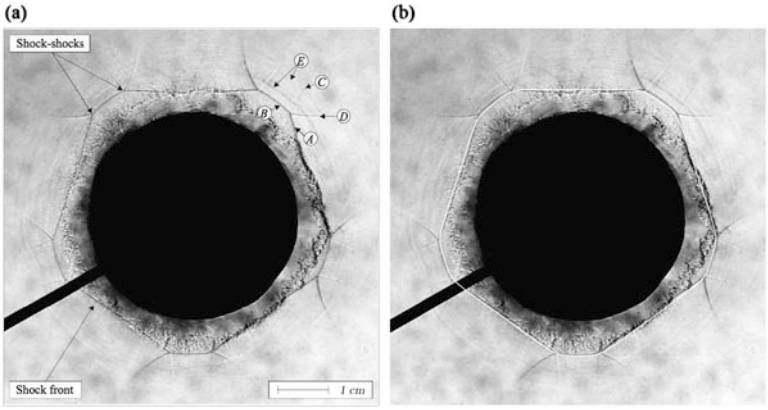

Fig. 3.36 Converging shock close to the center of the chamber. (**a**) Experimental schlieren image. (**b**) Comparison with the GSD computations (white curve), reproduced from [9], with permission from Springer

captured since GSD is based on the approximation that does not take into account the conditions behind the accelerating shock front.

Tailoring of the converging shocks by means of the reflector boundary was later continued in a work by Eliasson et al. [39]. Thin cylindrical test section with glass windows for visualization and replaceable reflector boundaries was mounted at the end of the annular shock tube facility at KTH (Royal Institute of Technology), Stockholm, Sweden, shown in Fig. 3.37.

Shocks with initial Mach numbers in the range $M = 2.3$–3.6 were produced and reflected from three different reflector boundaries, circular, octagonal with sharp edges, as well as smooth pentagonal as shown in Fig. 3.38.

In this work it was shown that it is possible to tailor the form of the converging shock by means of the reflector boundary. Also, the form of the outgoing shock after reflection from the center of the chamber was visualized, and the influence of the flow created by the initial converging shock was clearly seen as, e.g., in Fig. 3.39 where the octagonal structure is seen to be preserved for the outgoing shock.

One of the observations of this study was that despite the form of the reflector the final form of the converging shock, very close to the center of convergence was square-like, Fig. 3.40. This was attributed to the flow disturbances created by the four supports of the central annular body of the shock tube. A feature, previously detected by Takayama and co-workers [104].

3.5.3 Generation of Polygonal Shocks by Cylindrical Obstacles

The instability modes observed experimentally by Takayama and co-workers that transformed initially cylindrical converging shocks to polygonal structures stemmed from the supports holding the inner central body inside the shock tube. These

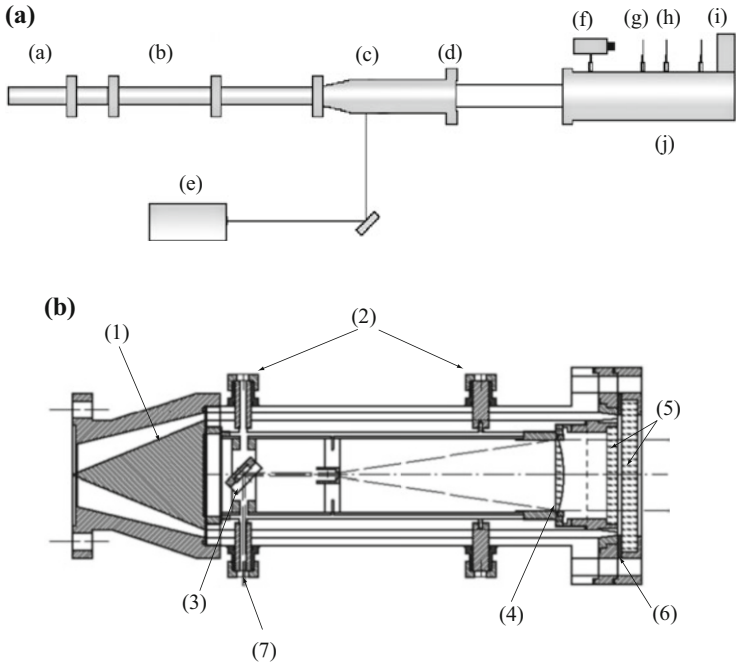

Fig. 3.37 (**a**) Schematic of the annular shock tube: (a) driver, (b) driven section, (c) conical transformation section, (d) test section, (e) pulsed laser, (f)–(j) schlieren optical setup. (**b**) Schematic of the annular part of the shock tube with the conical insert: (1) inner body with a cone, (2) supports, (3) mirror, (4) lens, (5) glass windows for visualization, (6) convergence chamber with replaceable reflector plates, and (7) laser light entrance. Both images reproduced from [39], with permission from Springer

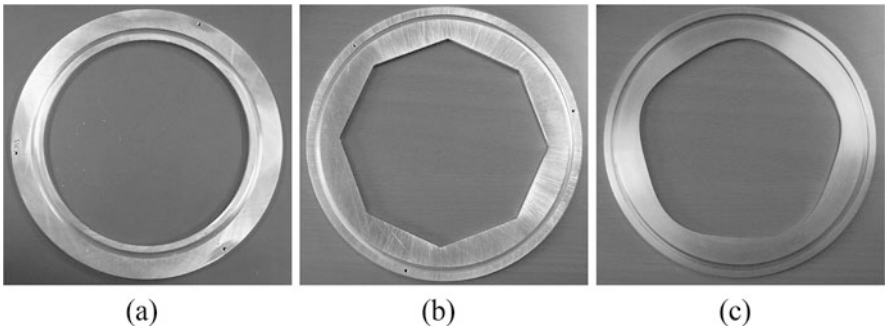

Fig. 3.38 Various reflector boundaries: (**a**) circular, (**b**) octagonal, (**c**) pentagonal, reproduced from [39], with permission from Springer

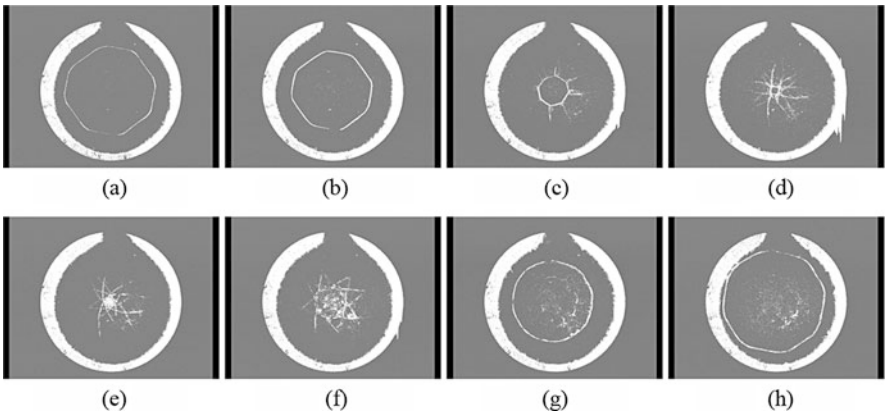

Fig. 3.39 Converging and diverging shocks from an octagonal reflector. (**a**) $\Delta t = 185\,\mu s$. (**b**) $\Delta t = 190\,\mu s$. (**c**) $\Delta t = 202\,\mu s$. (**d**) $\Delta t = 210\,\mu s$. (**e**) $\Delta t = 215\,\mu s$. (**f**) $\Delta t = 230\,\mu s$. (**g**) $\Delta t = 250\,\mu s$. (**h**) $\Delta t = 265\,\mu s$, reproduced from [39], with permission from Springer

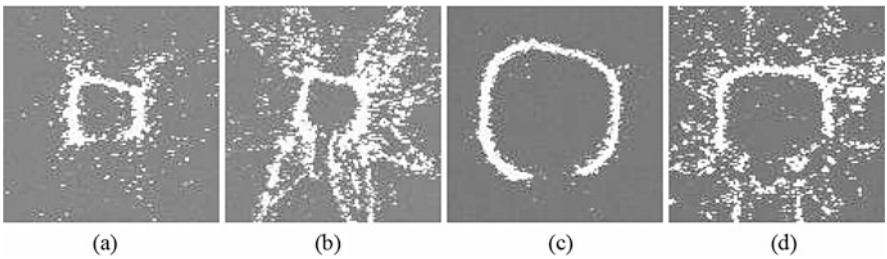

Fig. 3.40 Close-up of the region very close to the focal point of converging and outgoing shocks using circular and octagonal reflectors. (**a**) $M_s = 2.51$, circular reflector. (**b**) $M_s = 2.35$, octagonal reflector. (**c**) $M_s = 2.35$, circular reflector. (**d**) $M_s = 3.68$, octagonal reflector, reproduced from [39], with permission from Springer

structures introduced perturbations in the flow leading to a transformation of the shock front. The perturbations were persistent, and their influence increased in the process of convergence with increasing shock strength. Suppose that one introduces small objects, obstacles, in the convergence chamber intentionally. Could such objects, placed in a certain predetermined pattern, serve as a tool for exactly this purpose—transformation of an initially cylindrical shock front to a desired shape?

This question was studied in detail by Eliasson et al. [40]. A thin shock tube test section with a circular boundary was mounted at the end of the annular shock tube facility at KTH, Stockholm. The experimental setup was similar to the one described above with a difference that the initially cylindrical shock front was disturbed by small cylindrical objects placed in various configurations inside the shock tube test section as, for example, the one with 8×8 cylinders shown in Fig. 3.41.

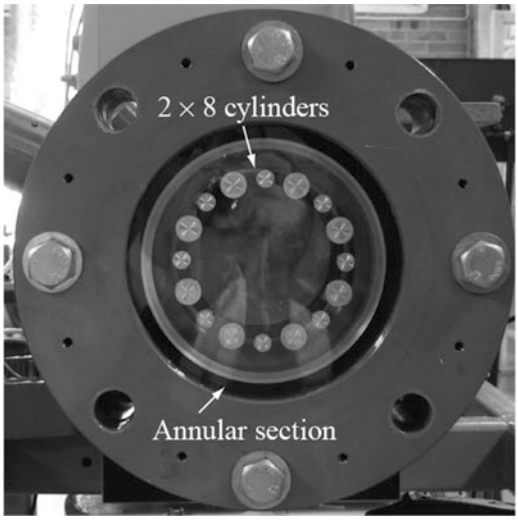

Fig. 3.41 Small cylindrical objects inside the shock tube test section, reproduced from [40], with permission from Springer

Both symmetric and nonsymmetric configurations were investigated. Shock fronts obtained by disturbing an initially cylindrical shock with one, two, three, and four cylindrical objects are shown in Fig. 3.42.

A full series of converging and diverging shocks obtained by eight cylindrical objects placed in a symmetric pattern is shown next in Fig. 3.43.

This work showed that it is possible to tailor the form of a converging shock to a symmetric as well as asymmetric shock front by placing cylindrical objects in the convergence chamber. The perturbations generated by the objects showed to be strong and able to transform an initially circular shock front to various polygonal-like structures.

Transforming a cylindrical converging shock to a shock with symmetric polygonal shock front is of advantage for the stability and thus high-energy concentrations at the focal region. As shown by Schwendeman and Whitham [94], a symmetric polygonal shock undergoes periodic transformations retaining the symmetry. Each transformation increases the strength of the shock due to Mach reflections at the corners of the polygon. It was also shown that the ratio of Mach numbers for the successive regular polygons follow the same formula as for a converging cylindrical shock. This is true for all regular polygons with the number of sides $n > 3$, meaning that this is not true for a shock front in the form of an equilateral triangle. Betelu and Aronson [14] obtained a self-similar solution for the case of a converging shock with a regular triangular shock front. By contrast to all other regular polygons, this solution does not lead to an increase of the converging shock strength because the reflection taking place at each corner of the triangular shock front is regular and not Mach reflection as in the case of regular polygons with greater number of sides then three. The authors conclude that unlike circular and regular polygon convergence, the case of a regular triangle leads to bounded energy density at the focal region.

This theoretical and computational result was confirmed in the experimental study by Eliasson, Kjellander, and Apazidis [42]. The annular shock tube facility at

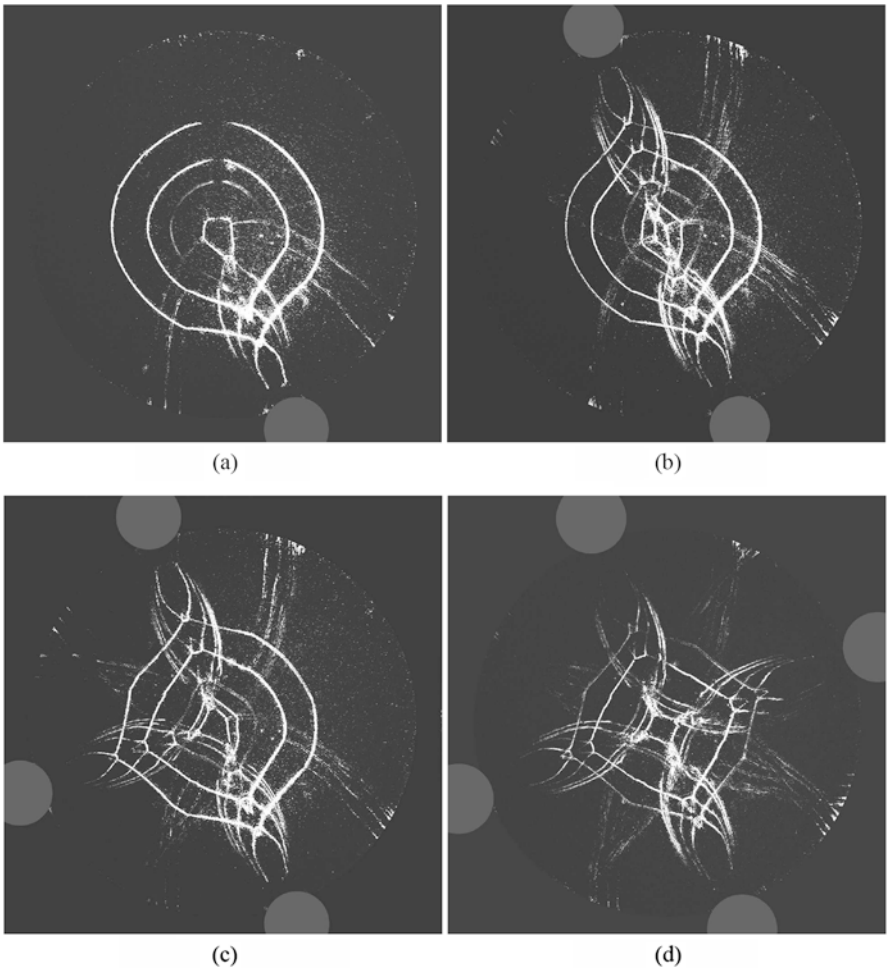

Fig. 3.42 Schlieren images from multiple sequential experiments displayed in a single figure showing how varying the number of cylindrical objects disturb the shock front evolution as it propagates toward the focal point. (**a**) One obstacle. (**b**) Two obstacles. (**c**) Three obstacles. (**d**) Four obstacles, reproduced from [40], with permission from Springer

KTH was used to study convergence of triangular and square shock fronts generated by three, respectively, and four small cylindrical objects placed in symmetric patterns in the convergence chamber, as shown in Fig. 3.44.

The idea was to compare convergence of a triangular shock with one which has one more side that is a square, Figs. 3.45 and 3.46. The experimental results showed that triangular and square-like shocks undergo different type of convergence. A triangular-shaped shock converged with unchanged form preserving the initial orientation until the very end of convergence indicating that the shocks at the

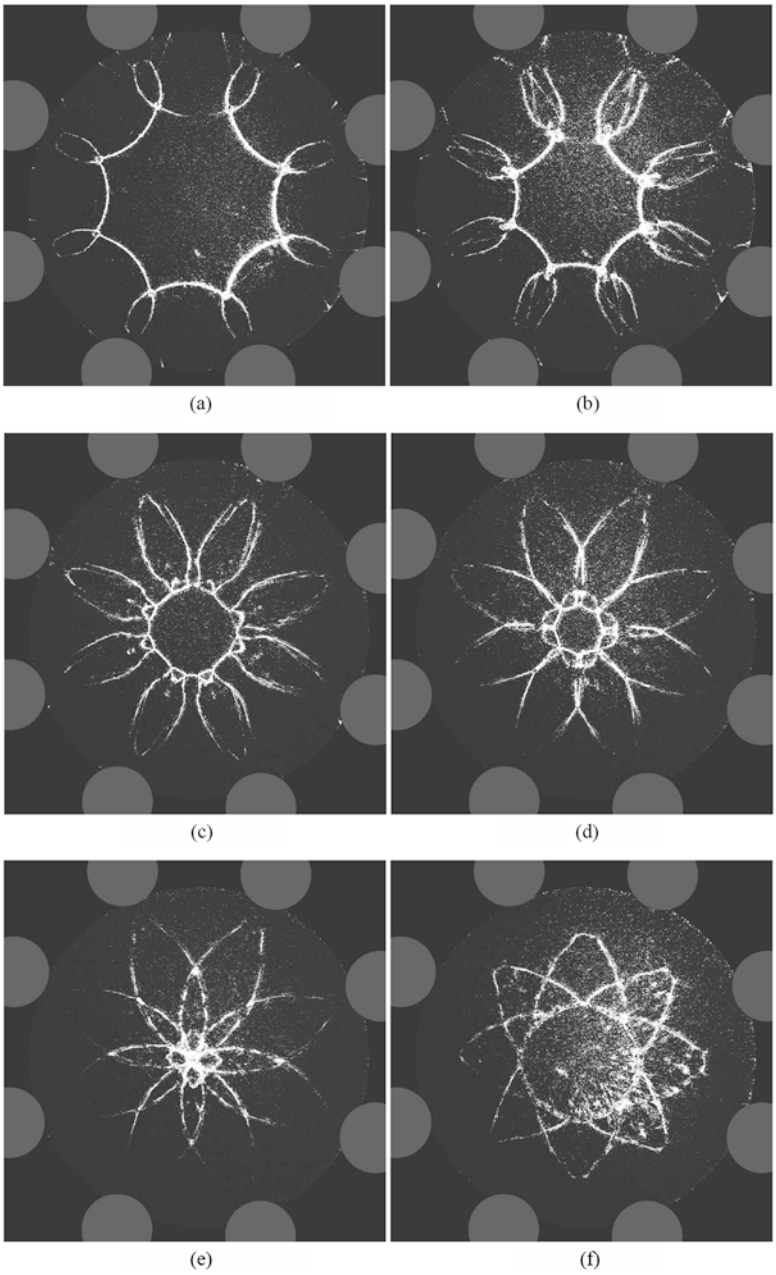

Fig. 3.43 Schlieren images of individual experiments repeated with different time delays for the camera. Symmetric shock fronts obtained by a combination of eight 15 mm diameter cylinders. (**a**) $\Delta t = 200\,\mu s$. (**b**) $\Delta t = 205\,\mu s$. (**c**) $\Delta t = 210\,\mu s$. (**d**) $\Delta t = 216.5\,\mu s$. (**e**) $\Delta t = 217.5\,\mu s$. (**f**) $\Delta t = 240\,\mu s$, reproduced from [40], with permission from Springer

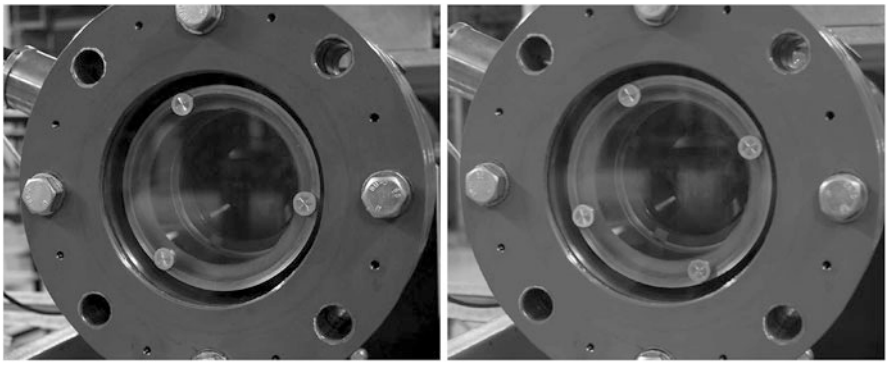

Fig. 3.44 Three and four cylindrical objects in the shock tube test section, reproduced from [42], with permission from Springer

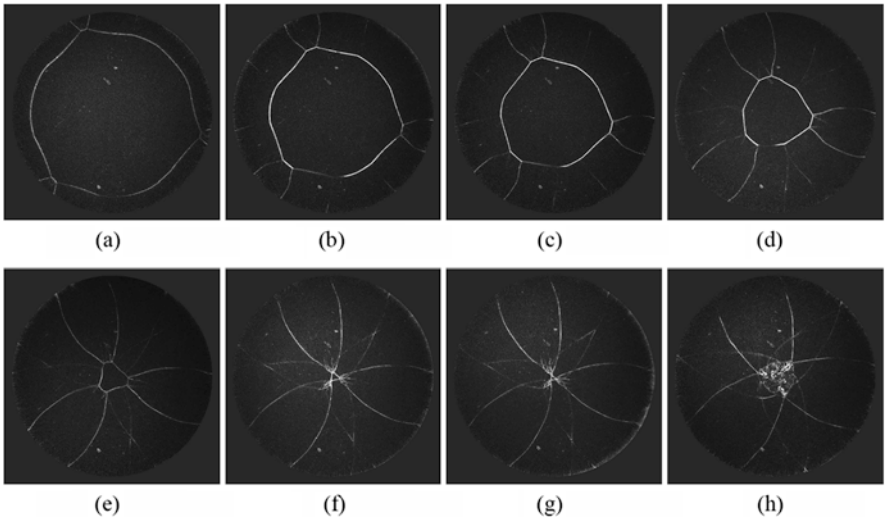

Fig. 3.45 Triangular shock convergence using three 15 mm diameter cylinders to shape the shock. (**a**) $\Delta t = 0\,\mu$s. (**b**) $\Delta t = 4\,\mu$s. (**c**) $\Delta t = 7\,\mu$s. (**d**) $\Delta t = 17\,\mu$s. (**e**) $\Delta t = 22\,\mu$s. (**f**) $\Delta t = 31\,\mu$s. (**g**) $\Delta t = 32\,\mu$s. (**h**) $\Delta t = 43\,\mu$s, reproduced from [42], with permission from Springer

vertices of the triangle undergo regular reflection. While in the case of a square-like shock, the shocks at the vertices suffered Mach reflection reconfiguring the form of the shock front. After one cycle a new square "rotated" 90° relative to the initial was formed as illustrated in Fig. 3.45.

As we saw, the presented experimental method makes it possible to tailor the form of converging shock by placing an array of small cylindrical obstacles in the chamber. The stability and symmetry of the converging shock are essential for its ability to produce high-energy density in gas at the focal region. The extreme conditions in gas are manifested by high pressures and temperatures leading to

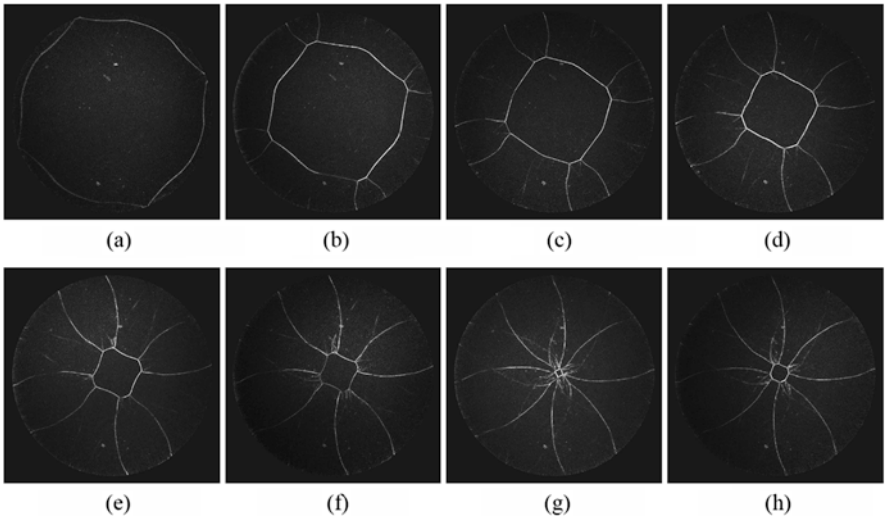

Fig. 3.46 Square shock convergence using four 15 mm diameter cylinders to shape the shock. (**a**) $\Delta t = 0\,\mu$s. (**b**) $\Delta t = 10\,\mu$s. (**c**) $\Delta t = 18\,\mu$s. (**d**) $\Delta t = 20\,\mu$s. (**e**) $\Delta t = 22\,\mu$s. (**f**) $\Delta t = 28\,\mu$s. (**g**) $\Delta t = 31\,\mu$s. (**h**) $\Delta t = 31\,\mu$s, reproduced from [42], with permission from Springer

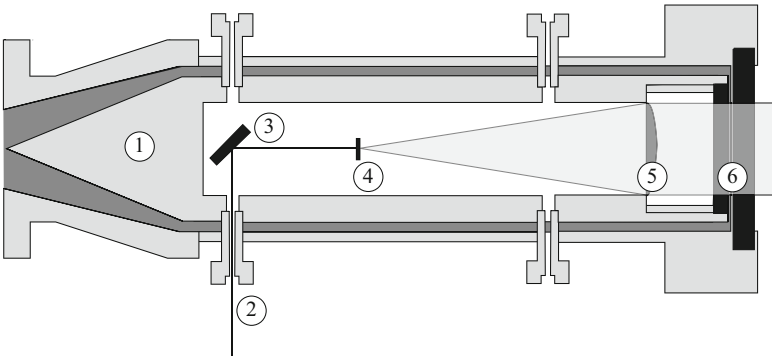

Fig. 3.47 The annular part of the shock tube: 1. inner body with a cone, 2. supports, 3. mirror, 4. beam expander, 5. lens, 6. test section, reproduced from [41], with permission from Springer

luminescence of the heated gas core visible to a naked eye. The main purpose of the work by Eliasson et al. [41] was to investigate the connection between the form of the converging shock and light emission levels of the compressed gas experimentally. The annular shock tube facility at KTH, Stockholm, with a central body is shown in the sketch in Fig. 3.47. An optical system consists of a mirror with beam expander and a lens provided for visualization by laser pulses and a schlieren imaging for capturing the form of converging shock fronts.

These were produced by disturbing the initial cylindrical shock by an array of three, four, seven, and eight small cylindrical objects placed symmetrically in the

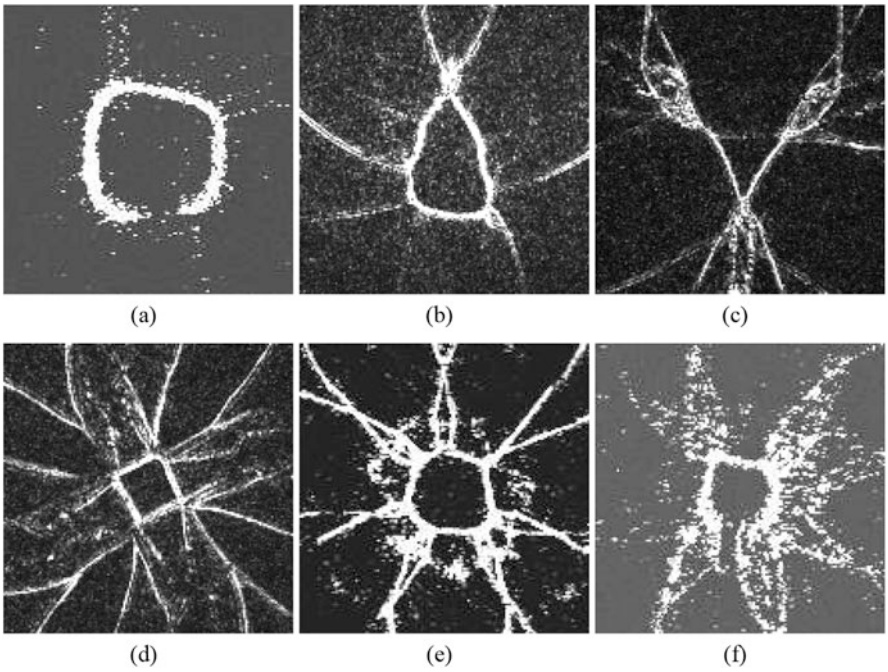

Fig. 3.48 Shock fronts approaching the center of the shock tube test section obtained by various combinations of cylindrical objects. (**a**) Cylindrical, (**b**) one cylinder, (**c**) three cylinders, (**d**) four cylinders, (**e**) seven cylinders, and (**f**) eight cylinders, reproduced from [41], with the permission of AIP

chamber. In addition the cylindrical shock front was also disturbed by a single cylindrical object. Converging shock fronts approaching the center of the chamber and obtained by various combinations of cylindrical objects are shown in Fig. 3.48.

The light emission of converging shocks at the instant of shock implosion was measured by a photomultiplier (PM) tube connected to the rear part of the shock tube. The PM tube was mounted inside a light sealed cover to prevent contamination from other light sources than those originating from the shock implosion. The PM tube was mounted without disturbing the schlieren optics setup to ensure the use of both measurements simultaneously. A photograph of the PM tube with a light cover is shown in Fig. 3.49.

Light intensity was measured both in air and argon. The intensity levels of light emission in argon were substantially higher than in air. Results of light intensity curves in argon for various shapes of the converging shock are shown in Fig. 3.50.

Figure 3.50a shows the light emission levels for a cylindrical shock not disturbed by any obstacles. One can see here a large spread up to a factor 10 in the intensity levels between the runs indicating the unstable nature of convergence. This may be compared to Fig. 3.50e showing light emission levels for a symmetric heptagonal shock formed by seven cylindrical objects. By contrast to a cylindrical shock, this

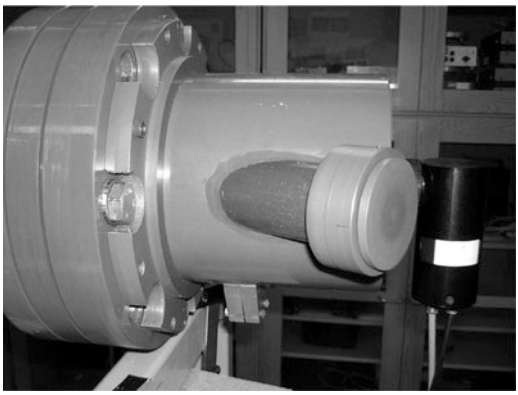

Fig. 3.49 The PM tube with a light cover seal at the rear part of the shock tube, reproduced from [41], with the permission of AIP

case shows very high degree of coherence between different runs indicating a much higher degree of stability in the focusing process. The duration of a typical light pulse was also measured with a full width of half maximum being about 200 ns.

Experimental investigation of the connection between the form of the converging shock front and intensity of light emission was complemented by numerical calculations to boost the detail analysis of convergence process. The Overture suite [22], a numerical scheme with adaptive mesh refinement, was incorporated. The gas was treated as ideal neglecting the real gas effects. Numerical shock profiles of an initially cylindrical shock disturbed by one, three, and four cylindrical objects are shown in Fig. 3.51.

A corresponding numerical temperature distribution for the case of a cylindrical shock, a shock disturbed by one, three, and four obstacles, is shown in the next Fig. 3.52.

3.5.4 Generation of Polygonal Shocks by Wing-Shaped Profiles

Desired polygon-like symmetric shape of an initially converging cylindrical shock may be achieved by placing an array of cylindrical obstacles in the convergence chamber as it was described in the previous section. Although small, as compared to chamber dimensions, cylindrical objects introduce substantial amount of drag and flow disturbances. Would it be possible to transform a cylindrical shock to a symmetric polygon by more aerodynamically streamlined objects thus reducing the overall drag and flow disturbances? This question was investigated experimentally and numerically by Kjellander, Tillmark, and Apazidis [65]. The test section of the shock tube facility at KTH was equipped with eight wing-shaped profiles placed radially in a symmetric pattern, as shown in Fig. 3.53.

The main purpose of this investigation was, however, to measure the temperature of the compressed heated gas at the moment of implosion, Fig. 3.54.

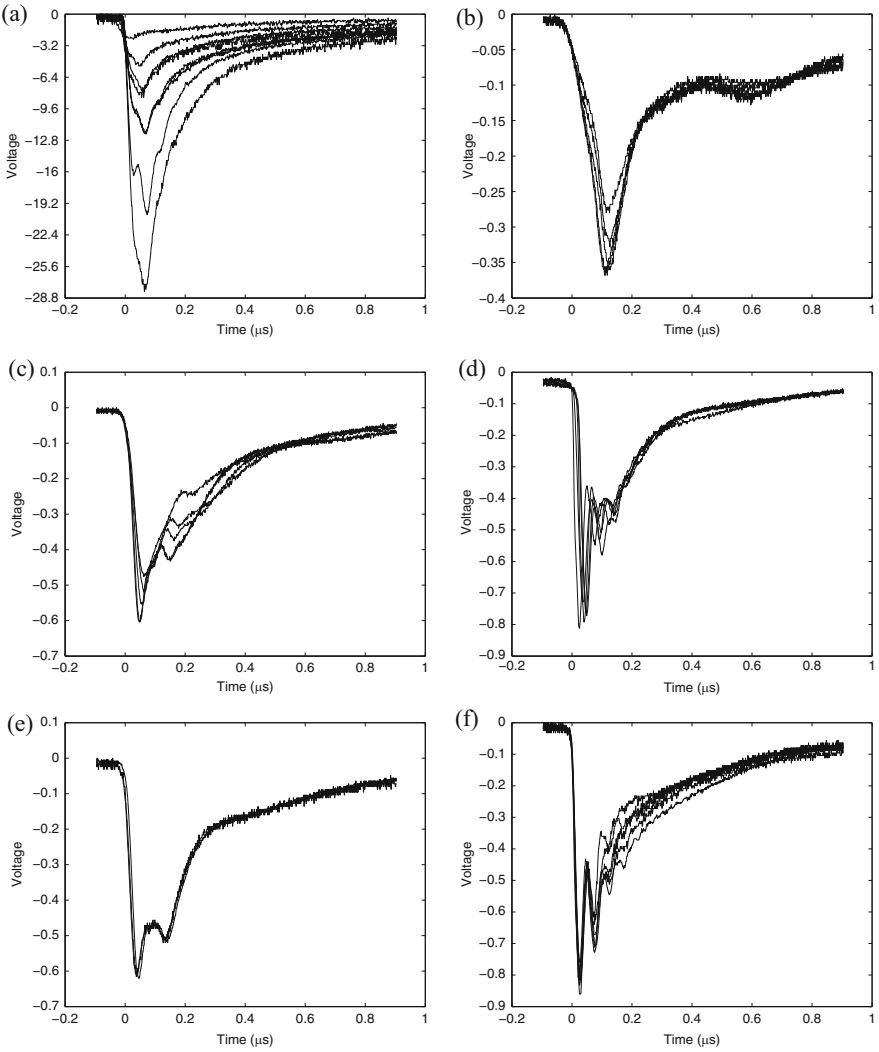

Fig. 3.50 Light intensity levels for various shapes of converging shocks: (**a**) circular shock, (**b**) one obstacle, (**c**) three obstacles, (**d**) four obstacles, (**e**) heptagon, and in (**f**) octagon, reproduced from [41], with the permission of AIP

The temperature measurements were conducted by means of photometric and spectroscopic equipment. Experiments were conducted with various combinations of driver and driven gases. The combination that produced maximum luminescence was helium as driver gas and argon as driven gas. Cylindrical shocks with initial Mach numbers $M = 2.3$ and $M = 3.8$ were transformed to polygonal form by an array of symmetrically arranged eight thin wing-shaped profiles, Fig. 3.53.

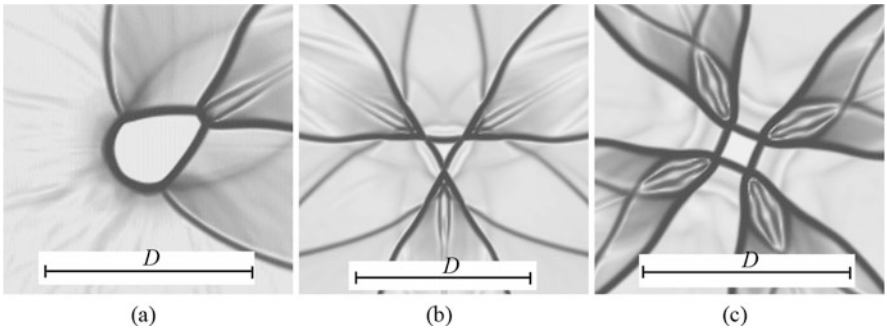

Fig. 3.51 Schlieren images from simulations in Overture showing shock waves close to the center of convergence for different shapes (**a**) one cylinder, (**c**) three cylinders, and (**d**) four cylinders. The diameter, D, of the cylindrical obstacle is indicated in the figures, reproduced from [41], with the permission of AIP

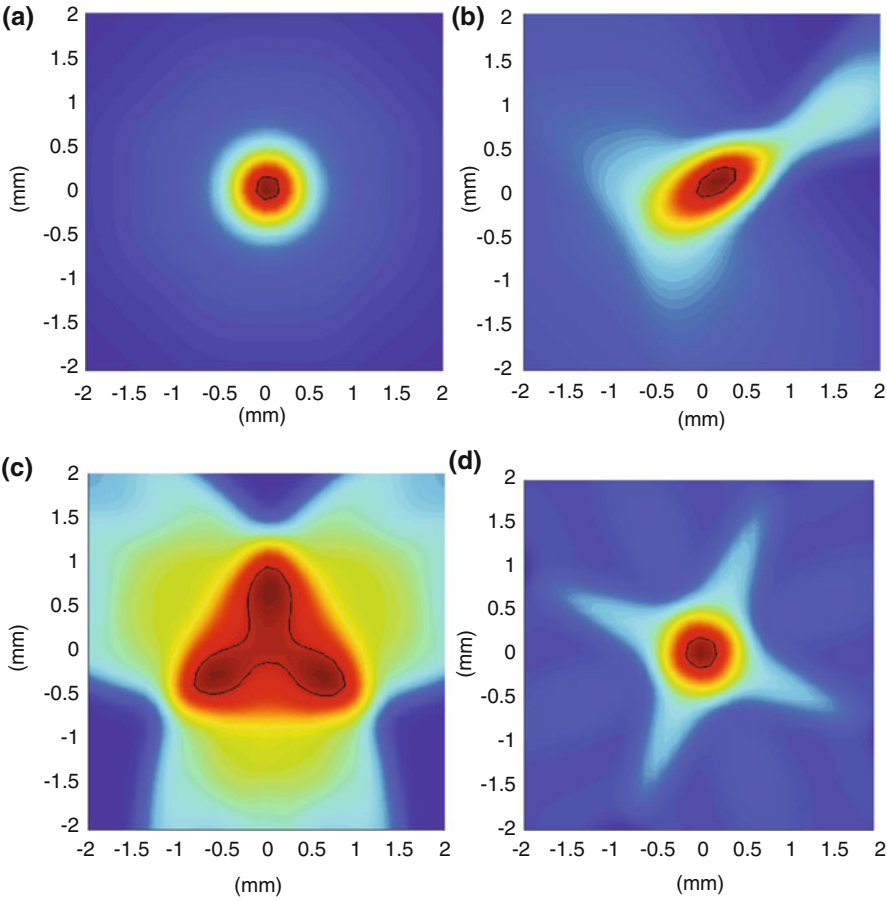

Fig. 3.52 Numerical temperature fields of a cylindrical shock as well as shocks disturbed by one, three, and four cylindrical objects, reproduced from [41], with the permission of AIP

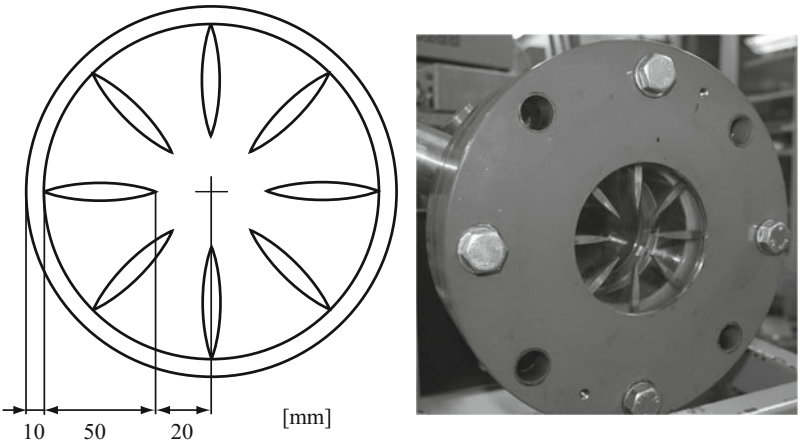

Fig. 3.53 Wing-shaped profiles in the convergence chamber, reproduced from [65], with the permission of AIP

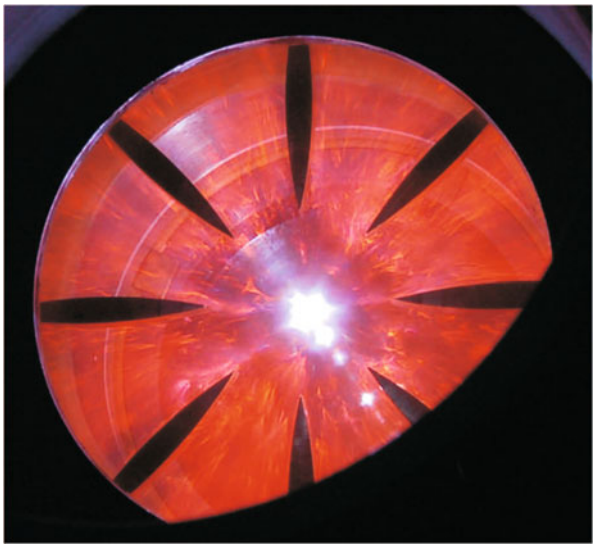

Fig. 3.54 Hot, compressed, and glowing argon gas core at the moment of shock implosion, reproduced from [65], with the permission of AIP

Multiple exposure technique made it possible to measure experimentally the value of the power-law exponent for converging polygonal shocks both in air and argon. This was compared with the Guderley solution

$$\frac{r}{r_0} = \left(1 - \frac{t}{t_c}\right)^{\alpha}, \tag{3.19}$$

for cylindrical shocks where r_0 is the initial radius and t_c the time needed for the shock front to reach the center. The values of power-law exponents for the

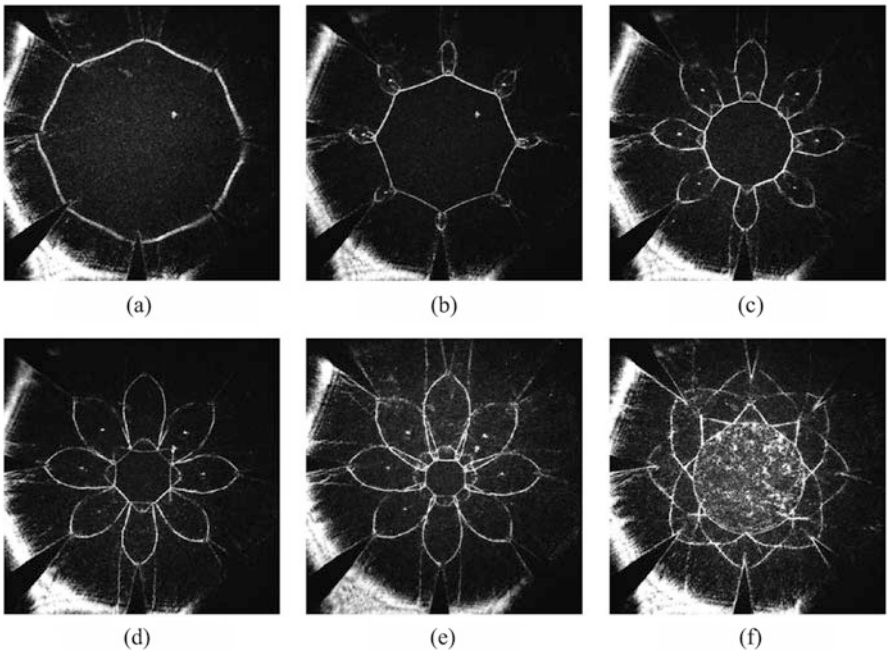

Fig. 3.55 Experimental schlieren images of converging (**a**)–(**e**) and diverging (**f**) shocks in air. (**a**) $\Delta t = -17.4\,\mu s$. (**b**) $\Delta t = -11.0\,\mu s$. (**c**) $\Delta t = -6.6\,\mu s$. (**d**) $\Delta t = -3.9\,\mu s$. (**e**) $\Delta t = -2.6\,\mu s$. (**f**) $\Delta t = +17.4\,\mu s$, reproduced from [65], with the permission of AIP

polygonal case were lower than for the circular case both for air and argon. A fit of experimental data for converging octagonal shock in air gave the value of $\alpha \approx 0.875 \pm 0.010$ and in argon $\alpha \approx 0.862 \pm 0.015$ as compared to the cylindrical case in air $\alpha \approx 0.834$ as and argon $\alpha \approx 0.816$. The lower values of the power-law exponent in the octagonal case give a slower than cylindrical shock convergence as may be seen from Fig. 3.56.

Polygonal shock fronts produced by this method showed a very high degree of symmetry during convergence all the way to the shock implosion and even after reflection from the center as can be seen in Fig. 3.55. Photographs of the light-emitting hot gas core at the moment of implosion give additional strong evidence of the high degree of stability of the convergence process in this case. Figure 3.54 shows light-emitting argon gas core at the moment of implosion. Figure 3.57a shows the full view of the test chamber, and Fig. 3.57b is a magnification showing a thin streak of argon plasma spanning the 5 mm space between the lower and upper plates of the chamber. Figure 3.57b gives a strong evidence of the preserved two-dimensional symmetry until the final instant of shock implosion.

Spectrometric measurements of light emission during shock implosion in argon were also conducted. The value of the initial Mach number at the boundary of the test section was $M = 3.8$. A spectrometer with a high temporal resolution of 60 ns

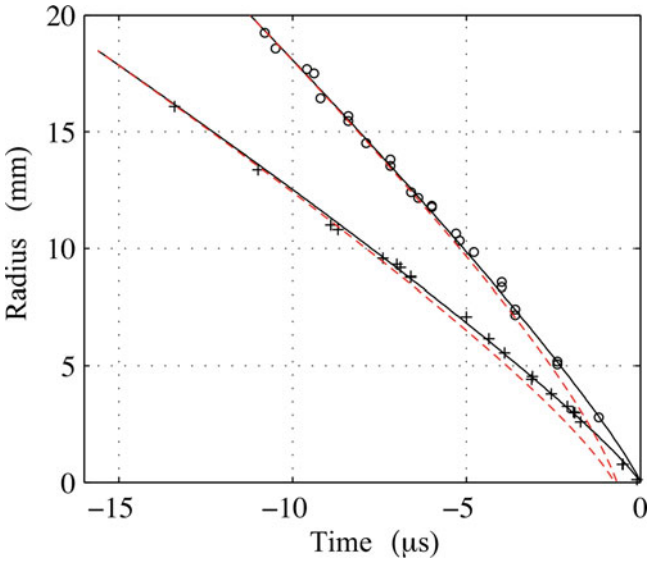

Fig. 3.56 Convergence of octagonal shocks in (+) and argon (o) as compared to cylindrical Guderley solutions (dashed line), reproduced from [65], with the permission of AIP

was used, and the temperature was deduced by a fit of the filtered continuum spectra to the black-body function. Figure 3.58 shows two black-body curve fits of a filtered continuum spectra at $t = 310$ and $t = 3,230$ ns after implosion giving temperatures of $T = 5,400$ and $T = 4,650$ K, respectively.

The maximum temperature of $T = 5,800 \pm 200$ K was measured at 100 ns after shock implosion. The temperature variation with time after implosion based on black-body fits is shown in the next Fig. 3.59.

Numerical computations were conducted to further enhance the description of the shock convergence process. The numerical model based on the artificially upstream flux vector splitting (AUFS) scheme for two-dimensional Euler equations introduced by Sun and Takayama [103] was adopted on an unstructured triangular mesh with automatic mesh refinement boosting the numerical accuracy in complicated geometry. Numerical schlieren shock profiles are shown in Fig. 3.60, and a comparison between numerical and experimental schlieren is given in the next Fig. 3.61.

The numerical model in this investigation was based on the solution of two-dimensional Euler equations with an ideal gas equation of state. The ideal gas approximation will certainly not hold as the converging shock approaches the focal region, and real gas effects such as ionization will play a significant role in the shock thermodynamics of the convergence process. The maximum measured temperatures in this two-dimensional case were under 6000 K as illustrated in Fig. 3.59. The ionization levels in argon at such temperatures are negligible, and ideal gas model may be incorporated. Comparison between numerical and experimental temperature

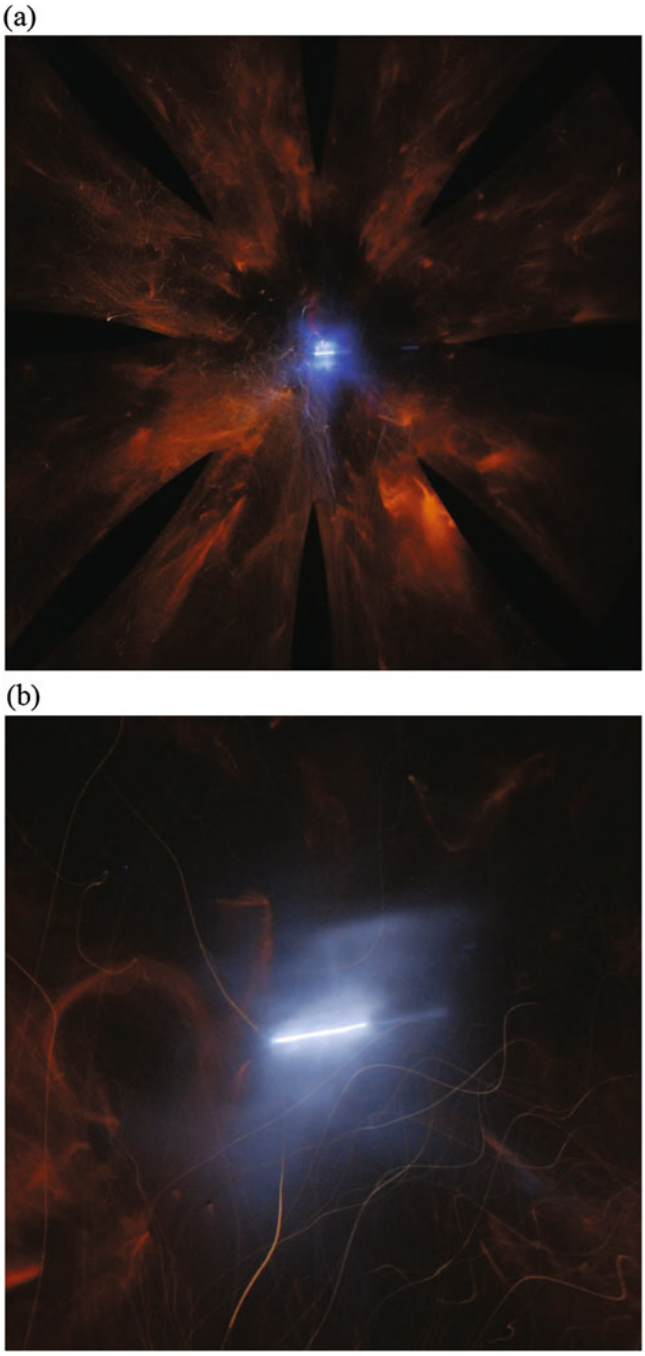

Fig. 3.57 Hot light-emitting argon gas core at the instant of implosion: (**a**) general view and (**b**) magnification of the core, reproduced from [65], with the permission of AIP

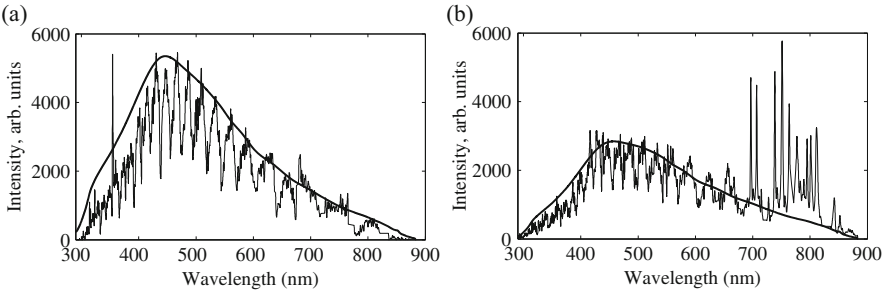

Fig. 3.58 Black-body fits of filtered continuum spectra at two instants after implosion, reproduced from [65], with the permission of AIP

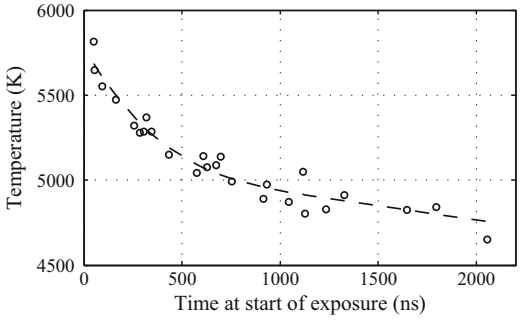

Fig. 3.59 Temperature variation with time after implosion, reproduced from [65], with the permission of AIP

values at the moment of shock implosion in argon is shown in Fig. 3.62. Figure 3.62 shows fair agreement of the prediction of the numerical model and experimental results in the temperature levels as well as the pulse duration.

Numerical temperature fields at various instants in the process of octagonal convergence are shown in the next Fig. 3.63.

In this respect it is worthwhile to note the similarities in shock formation mechanisms for converging symmetrical shocks. The symmetric shock structure shown in Fig. 3.43 was obtained by perturbing an initially cylindrical shock by eight small cylindrical objects placed symmetrically in the convergence chamber. The shock evolution and the overall shock dynamical is similar to converging shock fronts produced by eight thin wing-shaped profiles as shown in Fig. 3.55. A series of experimental images from I. Glass's book *Shock Waves and Man* [50] shows converging detonation shocks triggered by eight detonators and illustrated in Fig. 3.64. Also, in this case, the mechanisms of symmetric shock formation are the same as in the previous two cases as may be seen by, e.g., comparison with numerical schlieren images, Fig. 3.60 as well as temperature fields shown in Fig. 3.63.

The individual shock wave profiles generated by eight point source explosions transform into star-like structures very similar to those obtained by diffracting an initially cylindrical shock by eight thin wing-shaped profiles. Initial symmetry

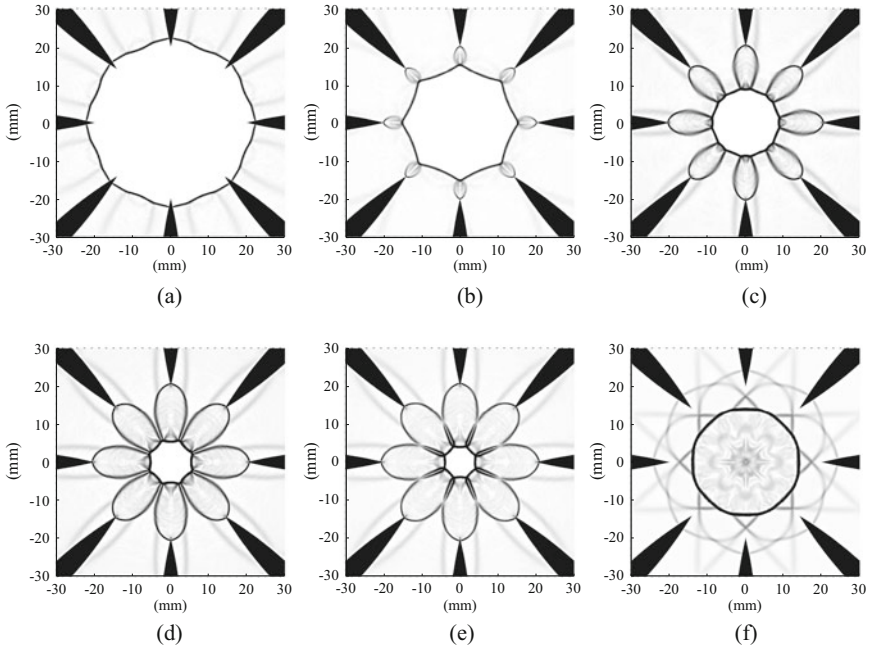

Fig. 3.60 Numerical schlieren images of converging shocks in air with initial Mach number $M = 2.7$ close to the center of the test section. (**a**) $\Delta t = -17.4\,\mu s$. (**b**) $\Delta t = -11.0\,\mu s$. (**c**) $\Delta t = -6.6\,\mu s$. (**d**) $\Delta t = -3.9\,\mu s$. (**e**) $\Delta t = -2.6\,\mu s$. (**f**) $\Delta t = +17.4\,\mu s$, reproduced from [65], with the permission of AIP

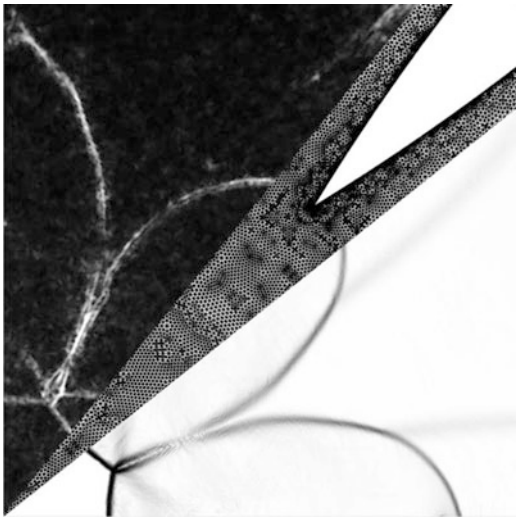

Fig. 3.61 Comparison of numerical and experimental schlieren images, reproduced from [65], with the permission of AIP

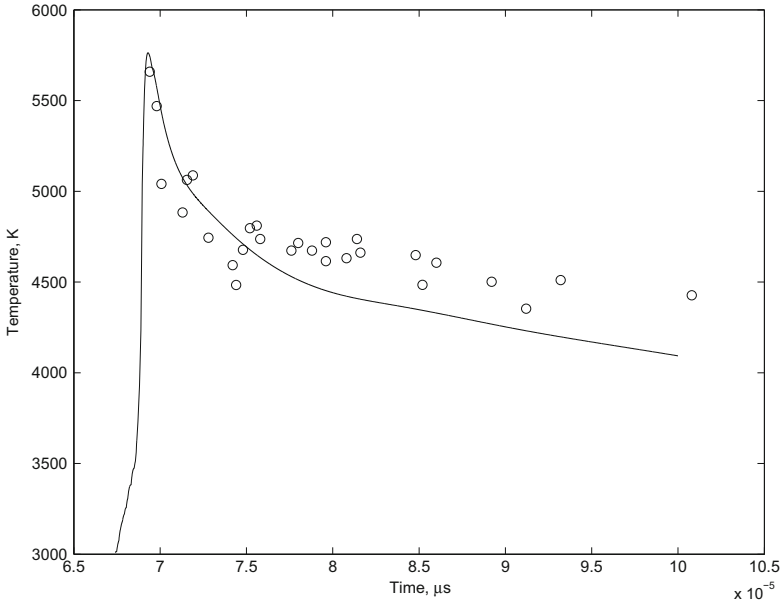

Fig. 3.62 Comparison of numerical and experimental temperature values close to implosion instant, reproduced from [10], with permission from Springer

imposed on the flow by obstacles or detonations coupled with a tendency to planarity as the shock strength increases results in polygonal-like structures. Plane shock portions meeting at the corners of the structure suffer Mach reflection which results in creation of new plane sides and thus reorientation of the polygon. A 22.5 degree rotation of the original configuration is distinctly seen in frame 15 of Figs. 3.64 and 3.63d.

The role of real gas effects during cylindrical and spherical shock implosion in monatomic gas was investigated theoretically and numerically by Kjellander, Tillmark, and Apazidis in [66]. The real gas effects for monatomic gas, such as ionization, electronic excitation, and Coulomb interaction, were incorporated in the jump conditions over the shock interface. These relations together with theory of geometrical shock dynamics (GSD) were integrated numerically along the C_+ characteristic. The main results of this study indicate that real gas effects in monatomic gas, especially ionization, have a major limiting effect on the final temperature of compressed gas, as its kinetic energy is transformed into other energy modes. An interesting feature of this process is that the compression ratio, e.g., density ratio, undergoes a substantial increase (almost 4 times greater) as compared to the ideal case. The Mach number and temperature for cylindrical and spherical shocks converging in monatomic gas are shown in Fig. 3.65. Figure 3.65 shows the

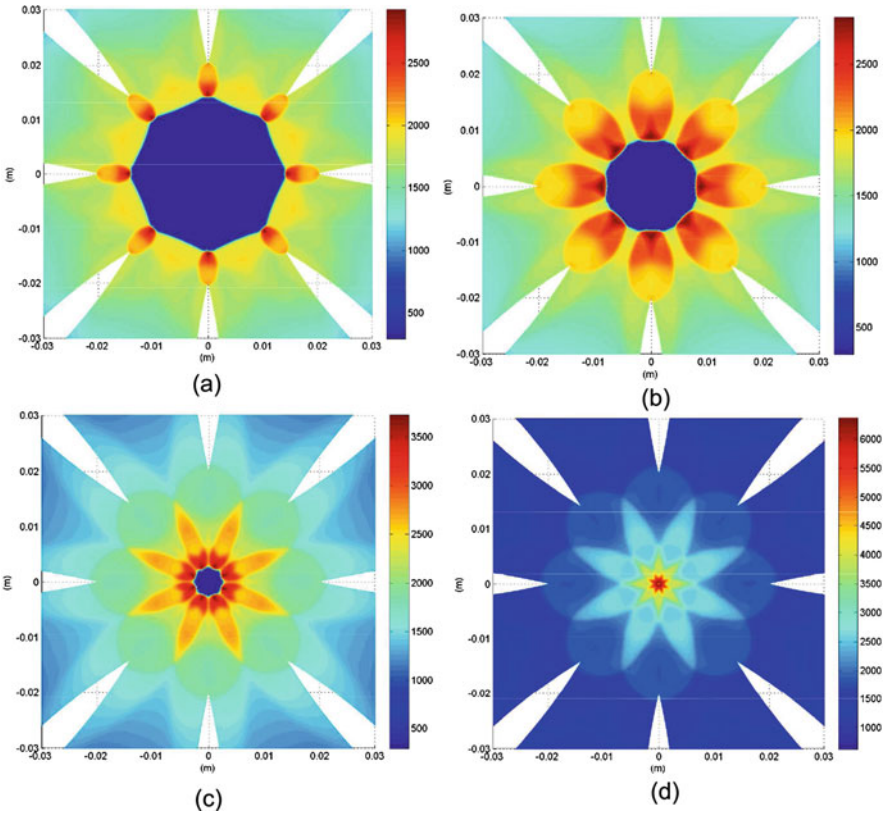

Fig. 3.63 Numerical temperatures fields in argon at various time instants (**a**)–(**d**). Initial Mach number $M = 3.7$, reproduced from [10], with permission from Springer

strong limiting effect of mainly ionization on the Mach number and temperature for cylindrical (C) and spherical (S) converging shocks. Full lines show relations including ionization and are compared with dashed line representing the ideal gas case.

3.5.5 Generation of Polygonal Shocks by Multiple Exploding Wires

Polygonal shock focusing can also be achieved by using multiple synchronized shock waves generated by exploding wires. One example of such an experiment is that by Gross and Eliasson [38]. In this experiment, an exploding wire system was used to generate multiple shock waves, and the shock waves were visualized by a z-folded schlieren system. The working principle of an exploding wire used for shock generation experiments is that by rapidly discharging high-voltage capacitors

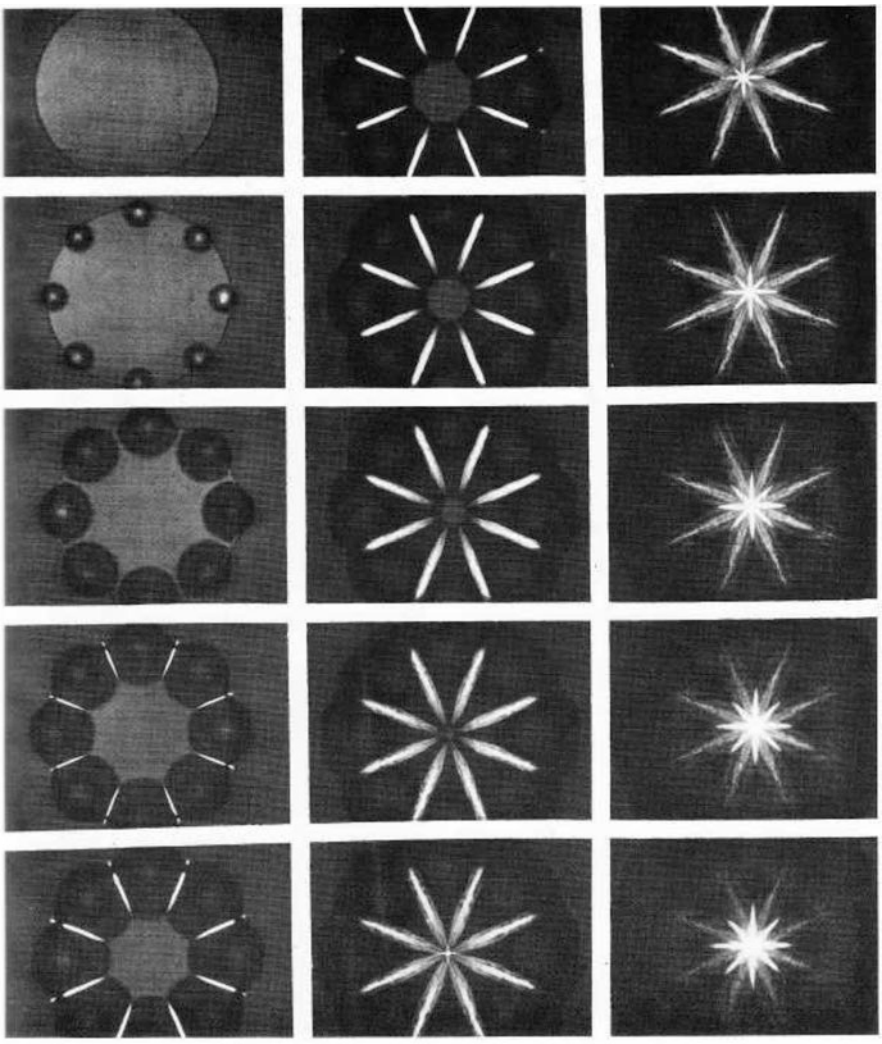

Fig. 3.64 Converging sh ock waves initiated by eight detonators placed symmetrically on the surface of a disc, reproduced from [50], (US Naval Weapons Laboratory)

though a small-diameter wire, the wire will rapidly be heated up and vaporized due to the resistance of the wire itself. Following vaporization, the column of hot gas or plasma made from the wire then expands rapidly, creating an expanding shock wave. This heating must occur over a sufficiently small time scale to ensure that the wire vaporizes rather than melts. In this setup, depicted in Fig. 2.9, the capacitors were charged by a Glassman EH series high-voltage power supply. The capacitors were five high-voltage capacitors connected in parallel with a total capacitance of 1.3 μF and a charge of 30,000 V. The experiment used a model 131M spark gap

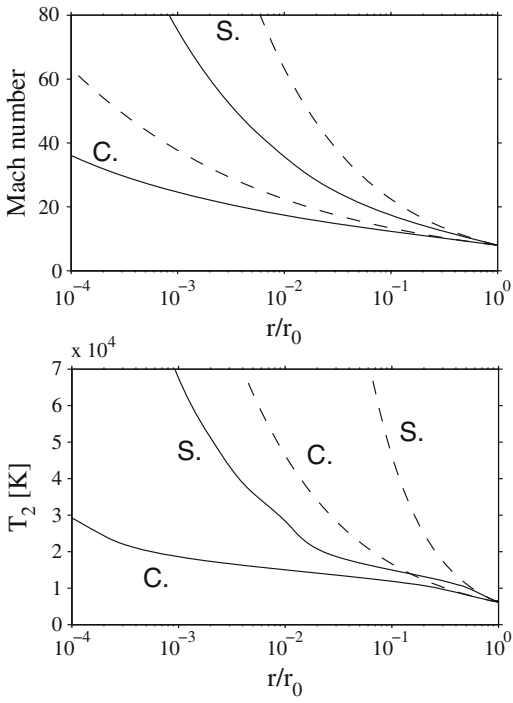

Fig. 3.65 Mach number and temperature behind the converging cylindrical and spherical shocks, reproduced from [66], with the permission of AIP

switch. Spark gap switches work by using a spark between two terminals to make or break contact in the circuit on time scales that are much faster than those achievable with electromechanical relays.

Shock focusing from multiple synchronized shocks was obtained both in two-dimensional scenarios, by using longer straight copper wires, and in three-dimensional scenarios, by using short looped copper wires. Experiments were performed with stored energies of over 400 J that were released within 2 µs. Several types of experiments were performed to investigate how multiple cylindrical or spherical shocks interacted. Experimental results showing successful shock focusing produced by three individual shock waves of equal strength is shown in Fig. 3.66. For this case, the three wires that were placed concentrically around the focal point did not generate transition from RR to IR, in agreement with [42].

However, by placing the wires with an angle of 60° between them, Fig. 3.67a, RR transition to IR occurred as expected. Symmetric focusing in two-dimensional was achieved by using a symmetry plane (a plastic sheet that allowed the shocks to reflect off its edge) along with the three wires placed the 60° angle between the three wires, shown in Fig. 3.67b. Larger numbers of wires, here up to 12 wires were tested, still represent a challenge in terms of obtaining equal initiation times and strength, Fig. 3.67c. This challenge can partially be overcome by using separate spark gaps for each wire. Figure 3.67d shows a comparison between the experiments (lower half) compared to numerical simulations obtained using Euler equations (upper half), similar to those presented in reference [86], resulting in very good agreement.

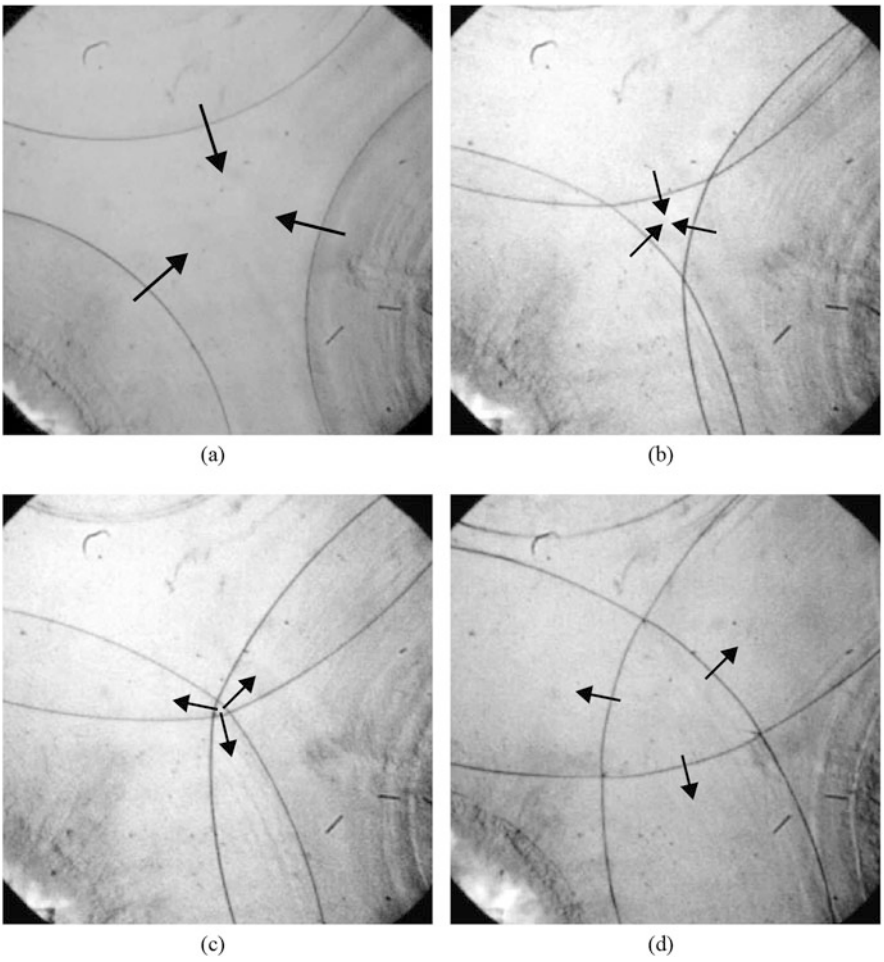

Fig. 3.66 Exploding wire results for regular reflection, arrows pointing in the direction of shock propagation. Three wires were evenly distributed in a circular pattern at equal radial distance around the focal region. Shocks were visualized using high-speed schlieren imaging. Converging shocks in (**a**) and (**b**) and reflected diverging shocks in (**c**) and (**d**). Figures obtained from V. Eliasson

3.5.6 Polygonal Shocks: Simulations

Qiu and Eliasson [86] studied the interaction of multiple blast waves to direct energy toward a target area while simultaneously reducing collateral damage away from the target. Simulations of multiple point source micro-explosives were performed, and the resulting shock interaction and coalescence behavior were explored. Figure 3.68 shows numerical schlieren visualizations of all cases at an early time instant and a

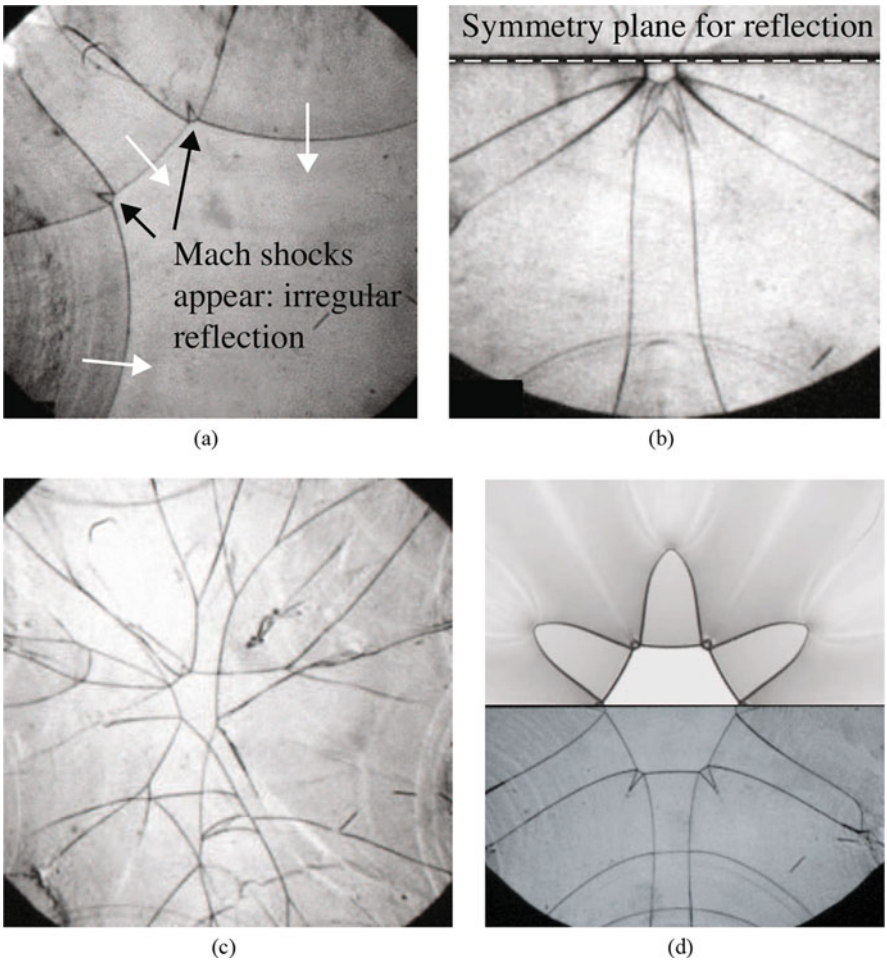

Fig. 3.67 Exploding wire results for irregular reflection. (**a**) To promote RR to IR transition, three wires were placed with a 60° angle between the middle wire and the two wires on each side. (**b**) Same setup as in (**a**) but a symmetry plane was added to generate a polygonal converging shock wave. (**c**) Twelve wires were successfully exploded albeit the timing was not synchronized. (**d**) Comparison between inviscid Euler simulations (top) and experiments (bottom). Figures from V. Eliasson

later time instant just before the converging shock fronts reach the focal region. For each case, probes were placed at the two points of interest, T1 and S1, to collect pressure data as a function of time.

For cases featuring three, five, and ten micro-explosives placed concentrically around the focal region, the resulting conditions were compared with those obtained using a single micro-explosive, summarized in Table 3.3. The energy summed over all micro-explosives and the radial position were kept constant. Each micro-

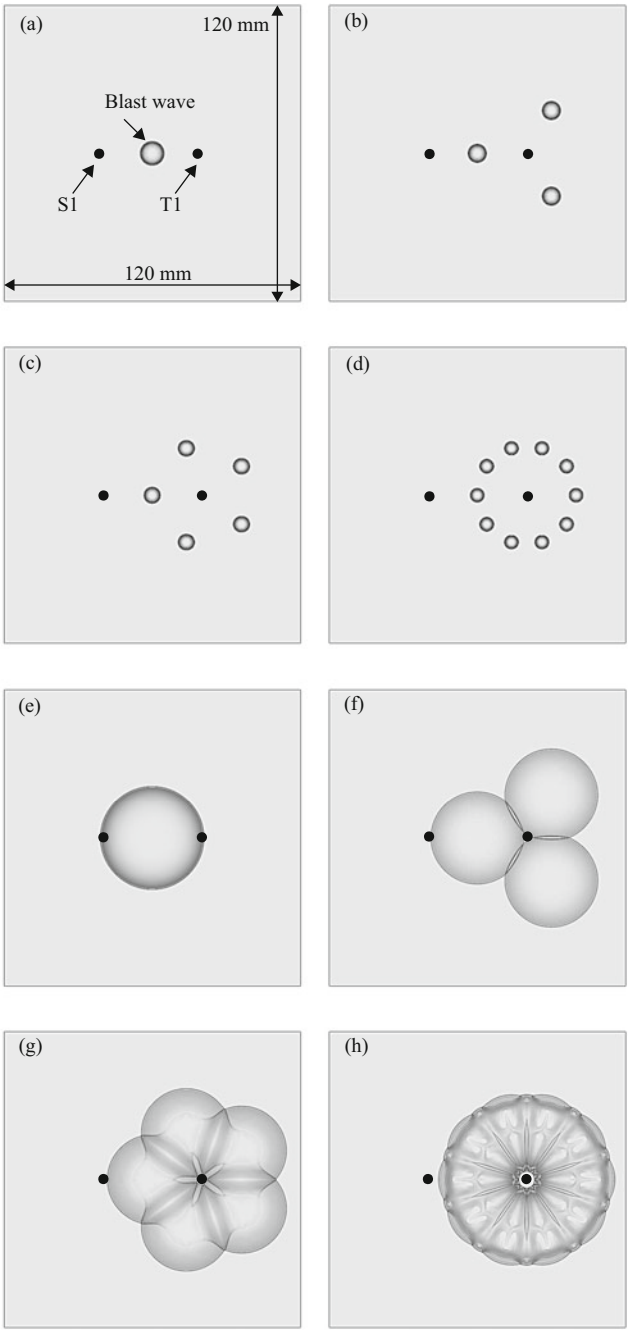

Fig. 3.68 Schlieren visualizations of the cases with (**a**) one (1C), (**b**) three (3C), (**c**) five (5C), and (**d**) ten (10C) point explosions in their early stages (top row) and later stages (bottom row), reproduced from [86], with permission from Springer

Table 3.3 Comparison of normalized peak pressure, p, and impulse, J, at the focal region (denoted T1 in Fig. 3.68) as well as a point (outside region, denoted S1 in Fig. 3.68) representing collateral damage for cases with one, three, five, and ten micro-explosives

	Focal region		Outside region	
Case	p	J	p	J
1	1	1	1	1
3	3.2	3.5	0.42	0.48
5	7.6	5.8	0.31	0.35
10	21.2	10.2	0.28	0.41

The total energy is kept constant for all cases, and impulse is collected for 20 time units after the peak pressure occurred, from [86]

explosive was modeled as a point source explosion using Taylor's approach [106]. The resulting blast wave propagation and shock front coalescence were solved using the inviscid Euler equations of gas dynamics on overlapping grids employing a finite difference Godunov scheme [51] and adaptive mesh refinement. Results show that multiple micro-explosives are beneficial for creating extreme conditions at the intended target area; with energy conserved, the use of 10 micro-explosives, each with initial energy E, increased the peak pressure by a factor of 20 over the use of a single micro-explosive with initial energy $10E$. Moreover, peak pressure at a point away from the target area is reduced by more than a factor of three. Impulse, which is a more relevant measure of the destructive force of a shock wave, follows similar trends as peak pressure.

This study achieved two goals: (1) showed it was possible to increase the extreme conditions at a designated target area by using multiple munitions and utilize shock focusing from the combined shock fronts and (2) proved that the reduction of collateral damage away from the target area was substantial. Furthermore, from the results with one, three, and five munitions, it was seen that the peak pressure at target S1 (representing collateral damage) was mainly influenced by the energy of the nearest blast; however, the peak pressure at target T1 (at the intended focal region of all coalescent shocks) was influenced by the shock focusing process. In the case of three munitions (case 3C), the convergent shock front formed a triangular shape that remained triangular during the focusing process. For the case with five munitions (case 5C), a pentagon was obtained. It only had time to reconfigure once from a pentagon (five-sided polygon) to a decagon (ten-sided polygon) during the focusing process. In the case with ten munitions (case 10C), the coalescent shock waves first formed a decagon and then changed into an icosagon (20-sided polygon) and back again to a decagon. Subsequently, this process was repeated multiple times throughout the focusing process. At each reconfiguration stage, the shock front Mach number was increased. The authors also investigated scenarios where one munition has been delayed. It was found that for cases with three, five, and ten munitions, with one munition delayed by Δt, there is not much influence on the peak pressure at target T1. But as the delay time was increased to $3\Delta t$, the pressure recorded at target T1 was reduced dramatically. This is also related to the position of the center of energy. With a longer time delay, the center of energy was shifted further away from target T1.

Next, to enable optimization of the shock focusing process, Qiu et al. [87] chose to utilize GSD because for shock dynamics problems, it can be more efficient than solving the Euler equations (for two-dimensional problems, the complexity is reduced at least one order of magnitude). Thus, GSD was implemented and parallelized for two-dimensional computations using a spatial decomposition method coupled with a front-tracking algorithm. With the use of symmetric boundary conditions, the method resulted in a considerable speedup for the shock focusing case of a 12-sided polygonal shock [87]. This GSD code also provides excellent agreement with Euler simulations in regard to predicting the location (or time) when reconfiguration processes occur, i.e., RR to IR transition. As a polygonal converging shock propagates toward the center, the lines of symmetry of the shock front are independent from its reconfiguration process. Thus, it is possible to compute only one section of the shock front instead of the full geometry. This symmetry feature indicates that the norm vector at each point where the line of symmetry meets with the shock front is always directed to the center. This is the boundary condition for each symmetric part of the shock front. For example, since the shock front features a polygonal shape, geometrical symmetry is used such that only a triangular portion of the converging shock, from a corner where two shocks meet to the midpoint of a neighboring planar side, is considered. The shock velocity on either side of this triangle is always directed along the sides of the triangle, i.e., the symmetrylines. With this condition, the problem size can be reduced from N down to $N/2n_l$, where N denotes the number of discrete points and n_l denotes the number of symmetric lines. A test on 12-sided polygonal (dodecagon) converging shock has been performed to verify the boundary condition. Three different symmetric parts (1/2, 1/4, and 1/24) have been computed independently and compared with the full size; see Fig. 3.69. It can be seen that all of the symmetric parts match the full size result very well. For performance analysis, the speedup of the symmetric boundary condition is defined as wall-clock time ratio of the full geometry versus the reduced geometry using a single core. Results are summarized in Table 3.4, and it is shown that for the dodecagon shock front, the speedup can be obtained up to 19.26.

3.6 Cylindrical Convergence

Is it possible to produce a converging cylindrical shock by some other method than the ones we discussed so far? In a short but very interesting paper, Saillard, Barbry, and Mounier [91] use GSD theory to compute the shape of the shock tube wall that will change an initially plane shock of uniform strength into a converging cylindrical sector or spherical cap without Mach reflections. The idea is to obtain a cylindrical or spherical shock section converging at the apex of a conically shaped tube. This method offers several advantages as compared to other methods. The converging shock is obtained directly without any reflections. The converging shock is not disturbed by the flow from an initial blast wave but propagates into a quiescent, undisturbed medium ahead. Ideally there are no losses due to transformation from planar to circular form. On the contrary the shock strength increases due to area

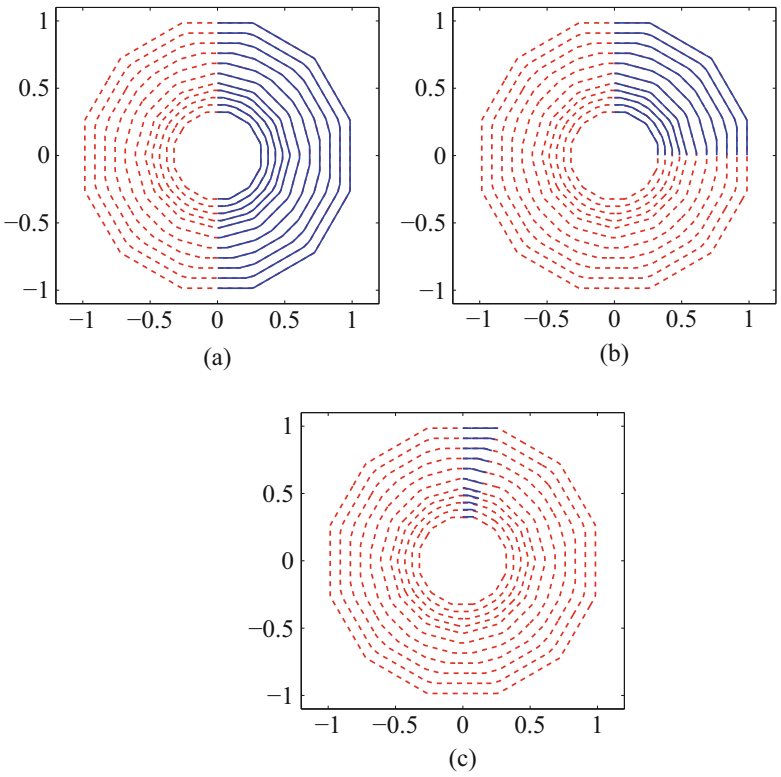

Fig. 3.69 Dodecagon shock front propagation at successive time instants. Red dashed line represents the full geometrical simulation and blue solid line represents, from left to right, 1/2, 1/4, and 1/24 of the full-size simulation using symmetric boundary conditions. (**a**) 1/2. (**b**) 1/4. (**c**) 1/24, reproduced from [87], with permission from Elsevier

contraction. We will discuss these as well as other properties of this method here. Figure 3.70 shows division of the computational region into subregions (I), (II), (III), and (IV). Subregion (I) is bounded by the final cylindrical shock and curved portion of the C_+ characteristic. Point F here is a singular point. Region (II) is connected with region (I) by C_+ characteristic to F and C_- characteristic. Region (III) is determined by the axis from A to B which is connected to region (II) by the C_+ characteristic. Finally region (IV) is connected by C_+ to initial shock and by C_- to region (II) or (III). The solution in the whole computational region is thus obtained. Of specific interest is the solution for which $M_0 = M_B$. In this case points A and B coincide, and the discontinuity of the wall shape at F vanishes. The authors call such case for a regular solution.

In a later work, Dumitrescu [37] confirmed once again that it is theoretically possible to produce a cylindrical shock sector in a two-dimensional channel by gradually changing wall shape of initially straight channel. An example of such shape transformation is shown in Fig. 3.71. Figure 3.71 shows a transformation of

Table 3.4 Computational cost and speedup of 1/2, 1/4, and 1/24 of the full geometrical simulation using symmetric boundary conditions

Problem size	Full size	1/2 size	1/4 size	1/24 size
Computational cost	17.15	8.65	4.44	0.89
Speedup	1.0	1.98	3.86	19.26

All the simulations are terminated after 10,000 iterations, from [87]

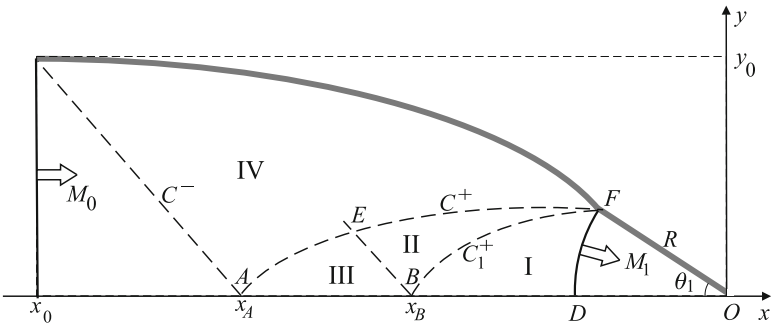

Fig. 3.70 Schematic diagram of the solution with subregions of the flow field, according to [91]

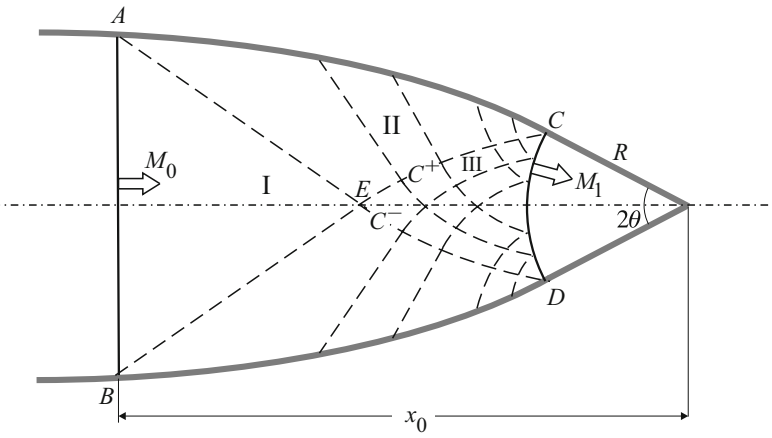

Fig. 3.71 Wall shape transformation of initially straight two-dimensional channel, according to [37]

initially plane shock AB into a circular sector CD. The region between AB and CD is divided into three subregions: in subregion (I) bounded by the initial straight shock and two straight parts of C_+ and C_- characteristics where the flow is in uniform state. Region (II) is a simple wave region adjacent to the uniform region (I). Region (III), bounded by the curved portions of C_+ and C_- characteristics and the cylindrical shock sector, is a region of uniform cylindrical implosion. Dumitrescu

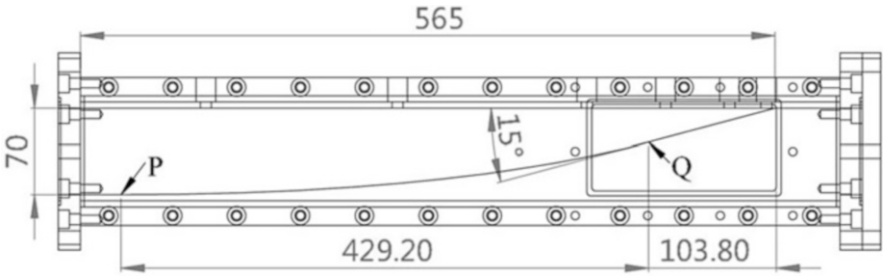

Fig. 3.72 Sketch of the end section where the straight shock is transformed to a cylindrical sector, reproduced from [124], with the permission of AIP

argues that gas dynamic problems in all regions with known boundary conditions along the region boundaries are well-posed and the flow parameters can thus be determined.

This method of transformation from a plane to a cylindrical shock was realized experimentally by Zhai et al. [124]. Using the GSD theory in the method described by Saillard [91], Barbry [12], Dumitrecu [37], the authors obtain an equation for the coordinates of the points (x_i, y_i) on the wall boundary in the form

$$y - y_i = (x - x_i) \tan(\xi \theta_i), \tag{3.20}$$

where ξ is a parameter that can be varied. Value $\xi = 1$ is chosen initially. The experiments were conducted in a shock tube with the end section wall shaped according to (3.20) as shown in Fig. 3.72.

Figure 3.73 shows experimental schlieren images of converging (a) and (b) and reflected (c) shocks in the channel. The circular form of the shocks is distinctly seen.

An interesting and different technique leading to similar results of transforming a planar incident shock into a cylindrical transmitted shock has been proposed by Dimotakis and Samtaney [36]. The authors proposed to use a suitably shaped interface between two gases that will refract the initial plane shock into a cylindrical shape. For a set of parameters defining the density ratio, ratio of specific heats between the gases and initial Mach number and the angle between the incident shock and the contact surface, they computed the equation for the interface by using local shock-polar analysis. Figure 3.74 shows the initial shock tube configuration with the two gases separated by the interface.

The authors conducted several numerical case studies for various values of the parameters using inviscid Euler equations as well as compressible Navier-Stokes code. Figure 3.75 shows the results of numerical computations for the inviscid (bottom) and viscous (top) case with the final cylindrical form of the converging shock.

This purely theoretical and numerical investigation was followed up by an experimental and numerical study of shock focusing in a 25° internal wedge mounted asymmetrically in shock tube [16]. The test gas was CO_2 and N_2 to

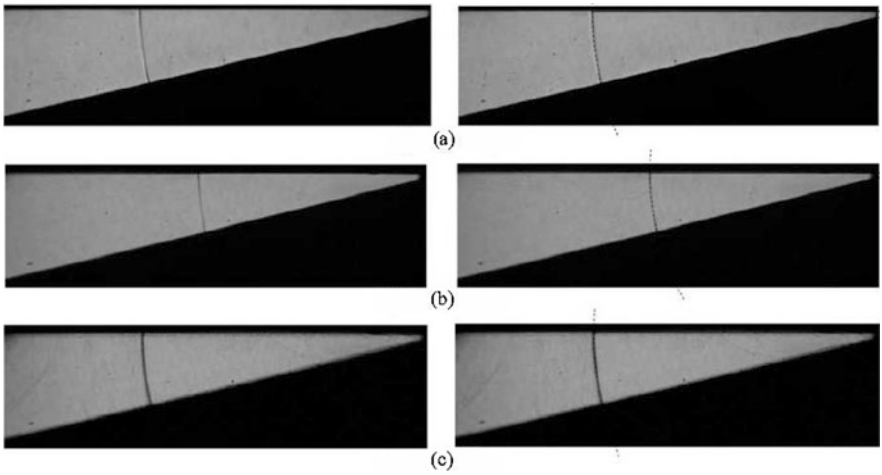

Fig. 3.73 Experimental schlieren images of converging (**a**, **b**) and reflected (**c**), shocks with initial Mach number $M_0 = 1.2$ and half-wedge angle $\theta_0 = 15°$. (**a**) $t = 1050\,\mu s$. (**b**) $t = 1100\,\mu s$. (**c**) $t = 1500\,\mu s$, reproduced from [124], with the permission of AIP

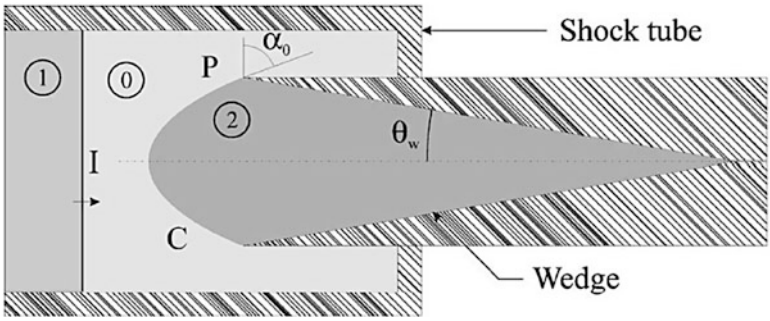

Fig. 3.74 Initial configuration showing the shock tube and the interface between two gases, reproduced from [36], with the permission of AIP

eliminate the real gas effects. One of the main and interesting results of this study is the influence of the initial shock configuration on the following shock strengthening and focusing process. Two initial shock strengths were tested in N_2: $M = 1.49$ and $M = 2.43$ as shown in Fig. 3.76.

The increase of the Mach number as the shock approaches the apex of the wedge was calculated and compared with the results of GSD theory for converging cylindrical shocks. The results are shown in Fig. 3.77.

As one can see from Fig. 3.77, the initially stronger shock has a typical stepwise evolution of a polygonal shock when plane portions of the shock propagate with a constant Mach number until they merge and develop a new Mach stem with a higher Mach number as, e.g., in [8] Fig. 3.32. On the average the increase in the

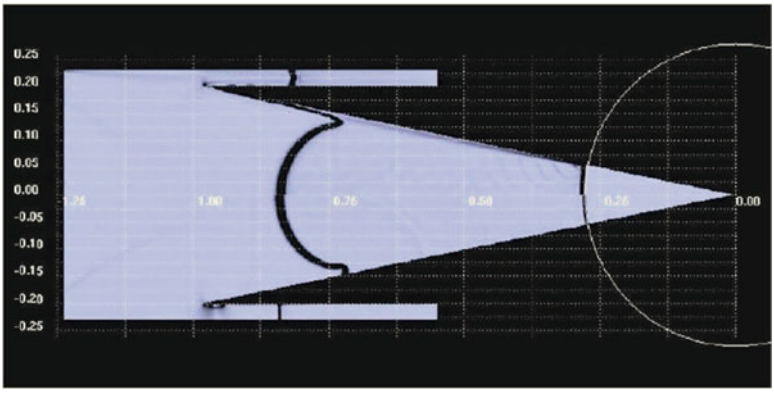

Fig. 3.75 Transformation of the initial plane shock into cylindrical form by a gas lens, reproduced from [36], with the permission of AIP

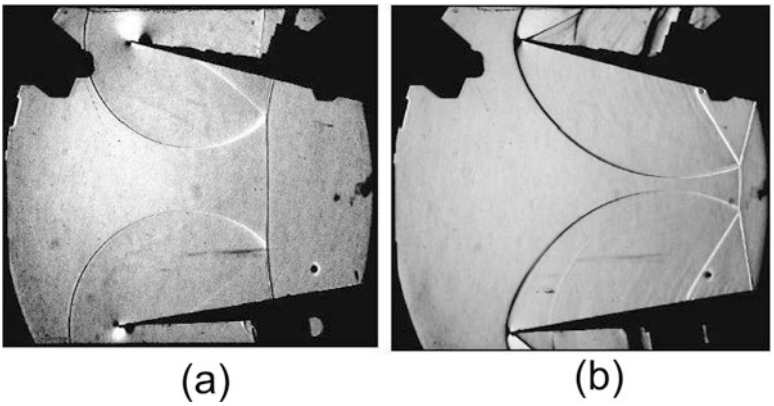

Fig. 3.76 Shock convergence in a wedge for two initial Mach numbers (**a**) $M = 1.49$ and (**b**) $M = 2.43$, reproduced from [16], with permission from Cambridge University Press

Mach number is the same as for a converging cylindrical shock which can be clearly seen in Fig. 3.77. This tendency is not so pronounced in Fig. 3.77a depending on a weaker initial shock.

3.7 Spherical Convergence

Spherical shock convergence is a far more powerful method of shock amplification than cylindrical case. In terms of experimental realization, it also presents a much harder challenge. In a pioneering experimental work by Roberts and Glass [89], the authors studied imploding shock waves in a hemispherical chamber filled with

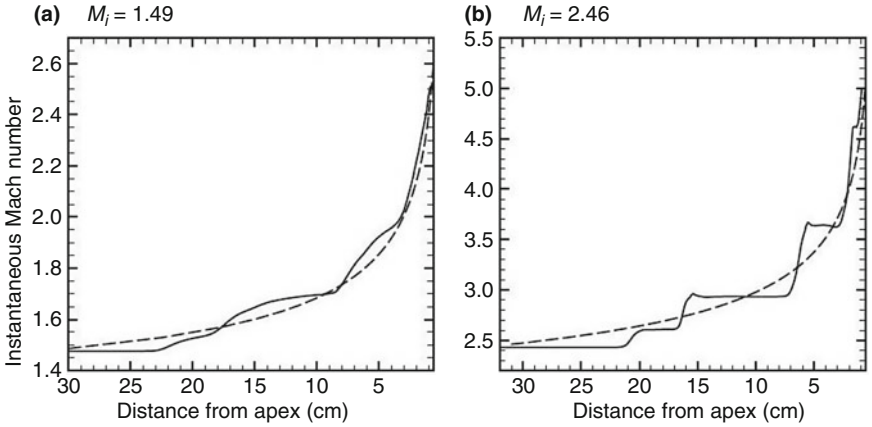

Fig. 3.77 The evolution of the calculated shock number for the converging shock in the wedge (solid lines) compared with a results of GSD (dashed lines) for a cylindrical shock, reproduced from [16], with permission from Cambridge University Press

hydrogen-oxygen-helium mixture at high pressure (∼10 atm). A detonation wave initiated at the center of the chamber was reflected from the chamber boundary and generated a hemispherical shock converging at the center of the chamber as shown in the sketch in Fig. 3.78.

Spectroscopic measurements of the light radiation from the imploding shock with a fit to Planck's curve (3.22) resulted in a black-body temperature of 5,600 K ± 200 K. The authors reported a deviation of the implosion point from the center of the chamber. To overcome this deviation from the center as well as reproducibility problems, this initial study was followed up by a more extensive investigation by Roig and Glass in 1977 [90]. By perfecting the shock initiation techniques, the authors were able to solve the off-centered implosions problem. Luminescence spots at various instants during the shock implosion are illustrated in Fig. 3.79.

The duration of the implosion pulse was determined to be $4 - 9\mu s$ depending on initial pressure. A typical temperature variation during implosion is shown in the next Fig. 3.80.

The ambient temperature T_A is 3000–3500 K and is elevated to the peak T_P = 4600 K as a result of shock implosion. Temperature histories as function of time at various initial pressures are shown in Fig. 3.81 in which the ambient temperature of around 3200 K is seen to rise to around 5000 K at the peak of implosion. The authors showed that the debris from the exploding wire igniting the initial shock lowers the duration of the implosion pulse as well as implosion temperature peaks. A maximum peak pressure was estimated at $(12.5 \pm 1.0) \cdot 10^3$ atm.

In 1982 Saito and Glass [92] conducted spectroscopic temperature measurements at the focal point of the explosive-driven implosion chamber used in the previous two studies. Converging shocks were produced by two methods. In the first one, labeled as gas runs by the authors, the chamber was filled with pressurized

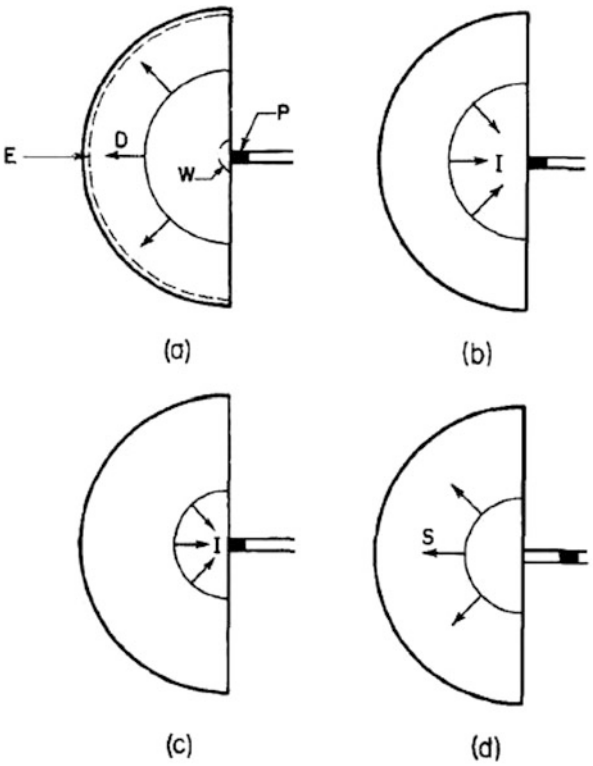

Fig. 3.78 Schematic of implosion chamber shock wave dynamics, reproduced from [89], with the permission of AIP

stoichiometric $H_2 - O_2$ gas mixture, and an outgoing detonation wave was initiated by an exploding wire at the center of the chamber. In the second method, labeled as explosive runs, an explosive shell of pentaerythritol tetranitrate (PENT: $C_5H_8N_4O_2$) was placed at the wall of the chamber. An outgoing detonation wave thus ignited an intense implosion shock by reflection impact. Fits of spectroscopic measurements to the black-body curve for both methods confirmed that the continuous radiation spectra were black-body curves with temperatures in the range $10,000 - 13,000$ K for gas runs and $15{,}000-17{,}000$ K for explosive runs.

We have already previously mentioned an extensive experimental study of spherical shock wave convergence by Hosseini and Takayama in 2005 [59], in connection with the experimental determination of the power-law exponent for converging spherical shocks. In this study a complete spherical test chamber was used. For visualization purposes the spherical test section of 150 mm diameter was transparent and placed inside a transparent aspheric outer wall with the dimensions of 270 and 203.3 mm. Figure 3.82 illustrates a photograph and a schematic diagram of the experimental setup.

The shock waves were generated at the center of the test chamber by silver azide pellets (AgN_3) that were glued to an optical fiber and ignited by irradiation of Nd:YAG laser beam. Double-exposure holographic interferometry as well as high-

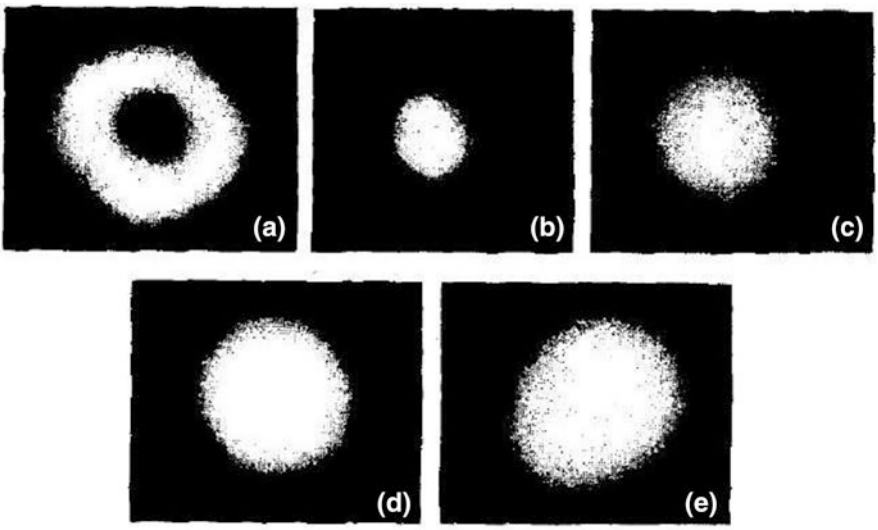

Fig. 3.79 Luminescence at various instants during shock implosion at the center of the chamber, reproduced from [90], with the permission of AIP

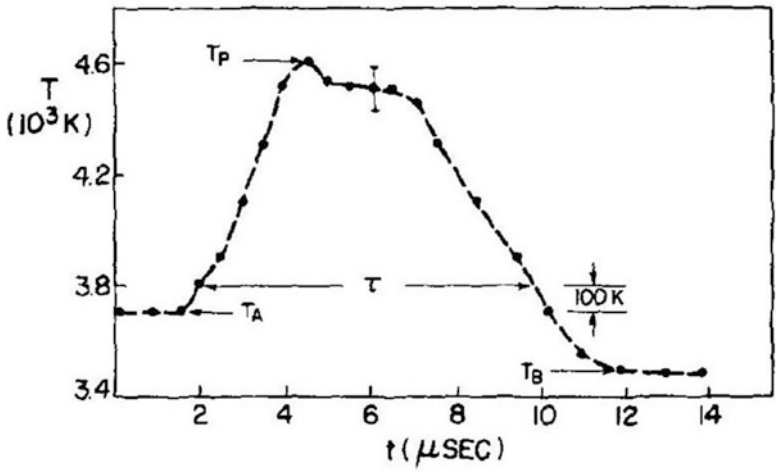

Fig. 3.80 Typical temperature variation during implosion, reproduced from [90], with the permission of AIP

speed (1,000,000 frames per second) time-resolved shadowgraph method was used for flow visualization. Pressure measurements of the incident and reflected shocks at the boundary of the test section were also conducted. The value of the incident Mach number, $M = 1.105$, at the wall of test section could thus be established. Variation of the diverging shock Mach number from the center of the test section to the wall for pellets with various masses is shown in the accompanying Fig. 3.83.

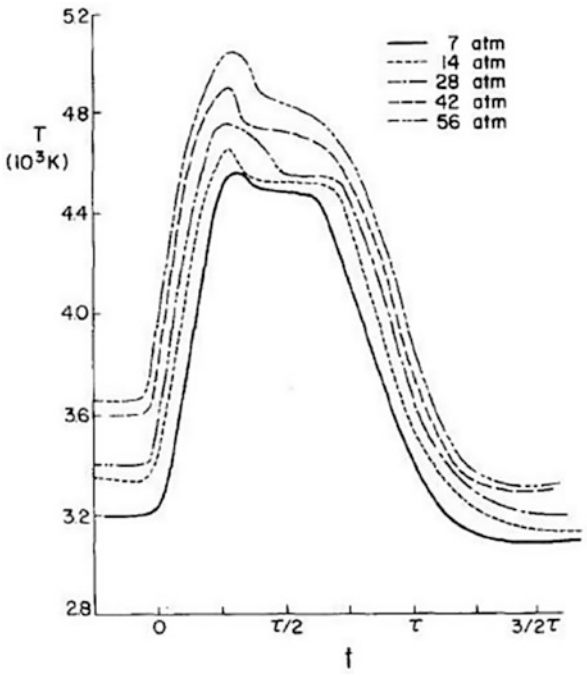

Fig. 3.81 Typical temperature variations at various initial pressures, reproduced from [90], with the permission of AIP

The strength of the initial spherical wave is rapidly decreased as the shock diverges from the center of the explosion. The Mach number of the initial diverging shock as it impinges on the boundary of the spherical test section is close to 1 even for strong initial shocks generated by 10 mg pellets with Mach initial number above 7. Excellent optical setup enables to trace the shock propagation of diverging as well as converging shocks. A series of high-speed shadowgraph images illustrate the propagation of the initial diverging shock in Fig. 3.84.

It is interesting to note here that although the initial shape of the diverging shock is not spherical, it tends to a spherical form as the shock propagates from the center of explosion demonstrating the inherent stability of diverging shocks. A corresponding sequence of converging shocks after reflection from the boundary of the test section is shown in Fig. 3.85.

The form of the converging shock fronts is close to spherical after the reflection. The deformation of the converging shock fronts and deviation from the spherical form increased as the shock approached the center of the test chamber encountering with detonation products gas cloud. A remarkable and important achievement of this investigation is the detailed visualization and analysis of the convergence process of a spherical shock inside a spherical convergence chamber. The value of the power-law exponent could therefore be extracted from radius versus time plot, Fig. 3.17, with high degree of accuracy for this case. This was possible due to a sophisticated optical setup combined with high-speed (1,000,000 fps) camera as well as sequential infinite fringe interferometry and pressure measurements.

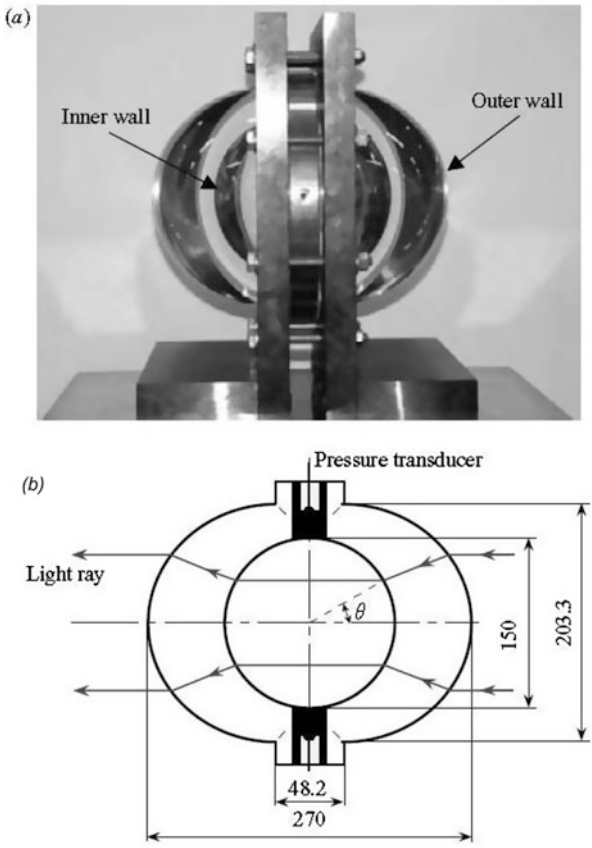

Fig. 3.82 Experimental setup (**a**) photograph and (**b**) schematic diagram, reproduced from [59], with permission from Cambridge University Press

As we have seen, spherical converging shocks are mainly generated by reflecting a blast wave created at the center of a sphere by a semispherical or spherical surface, thus reversing it to focus at the center of the chamber, as in, e.g. [59]. This method has several disadvantages: (1) the strength of the initial blast wave created at the center of the chamber is significantly decreased as it reaches the reflector boundary; (2) there are further significant losses in the strength of the reflected, converging shock due to the flow directed outward from the center of convergence created by the strong initial blast wave; (3) the symmetry of the reflected shock is distorted as it propagates in the region disturbed by a powerful initial blast wave; (4) the symmetry of the converging shock is further distorted as it encounters detonation products gas cloud at the center of the chamber; (5) temperature measurements of the converging shock are contaminated by the temperature field from the outgoing blast wave usually initiated by explosion; and (6) it is difficult to access the center of the sphere for visualization and measurements. To overcome these difficulties, one could utilize the idea of shaping cylindrical or spherical shock by a gradual transformation of a channel with initially straight walls put forward by Saillard [91],

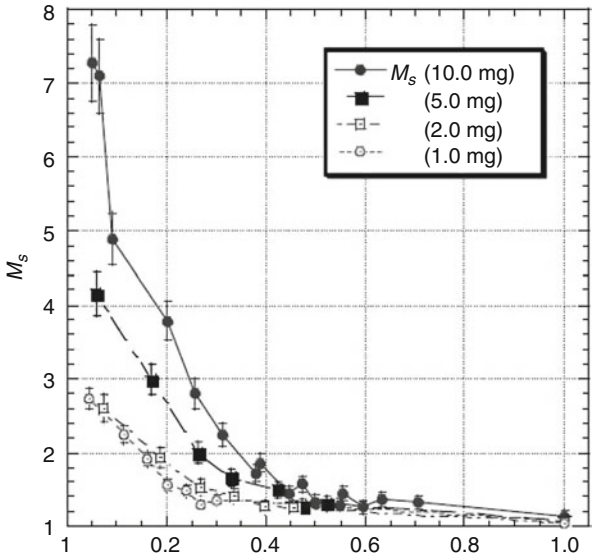

Fig. 3.83 Variation of diverging shock Mach number with radius, reproduced from [59], with permission from Cambridge University Press

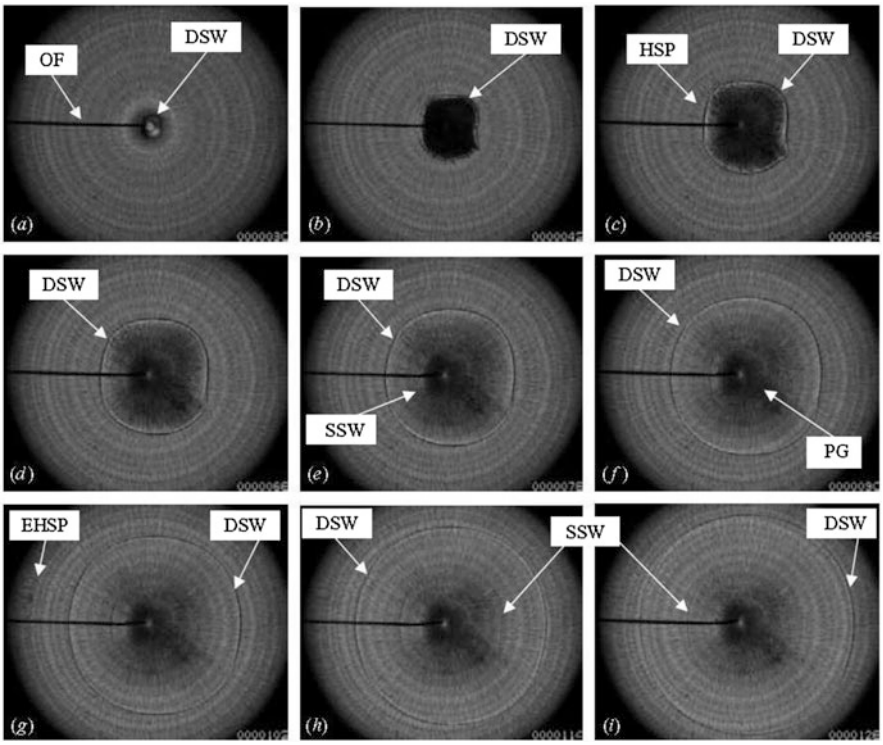

Fig. 3.84 High-speed shadowgraph visualization of diverging shocks, reproduced from [59], with permission from Cambridge University Press

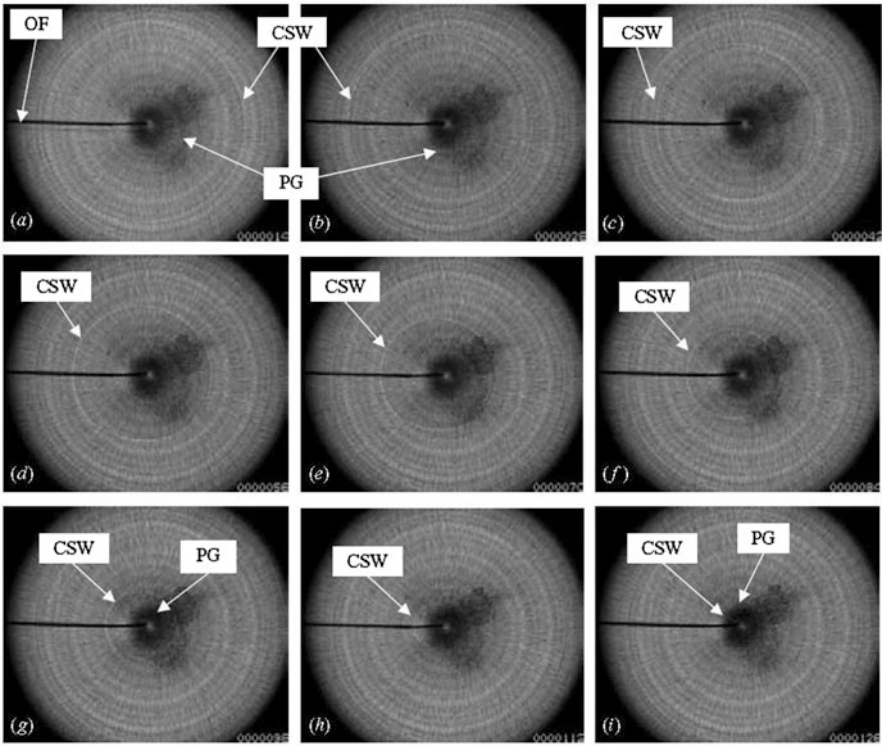

Fig. 3.85 High-speed shadowgraph visualization of converging spherical shocks, reproduced from [59], with permission from Cambridge University Press

Barbry [12], Dumitrecu [37], and Zhai [124]. The initial plane shock would then focus at the apex of the cone directly without struggling against the flow ahead. There would be no disturbances from the oncoming flow. The region ahead of the advancing shock would be undisturbed, and the conical geometry would provide direct access to measurements through a small opening at the tip of the cone. It is well known, however, that shock convergence in a simple conical geometry creates a series of Mach reflections leading to shock fronts with plane portions decreasing the focusing effect.

The idea of shock form tailoring by gradual transformation of channel walls was further developed in an experimental, theoretical, and numerical investigation by Kjellander, Tillmark, and Apazidis [68]. In this work the authors studied convergence of a spherical cap produced in a shock tube with cylindrical cross-section. The spherical form of the final converging cap is obtained by a smooth transformation of a plane shock in a specially constructed transformation section. The shape of the walls of the transformation section were obtained by Whitham's theory of GSD along with numerical computations so that an initially plane shock takes the form of a perfect spherical cap without any Mach reflections. When the

spherical form is obtained, it is guided to a final small steel conical end section where it implodes at the tip of the cone. A tiny opening at the tip of the cone provides free access to hot gas-plasma core produced by intense shock compression. The opening is sealed by a quartz glass, and measurements of radiation spectra are performed by leading the light pulse from glowing gas plasma through optical fibers to photomultipliers and a spectroscope. The shape of the walls of transformation section in parametric form is given by Eq. (3.21).

$$\begin{cases} x &= C_1 \sin\theta \\ y &= C_2 - C_3(1 - \cos\theta) \end{cases} \tag{3.21}$$

The values of coefficients C_1, C_2, and C_3 are chosen to match the dimensions of the of the shock tube and under the constraint of a set final cone angle defining the small conical end of the section. Numerical schlieren images showing convergence in a conventional conical section vs smooth transformation section are illustrated in Fig. 3.86.

The transformation section was made of a plastic cast held in place by a steel housing. The end cone was manufactured in steel with the tip cut 0.8 mm from its apex leaving a circular opening with radius of 0.3 mm. The opening was sealed with

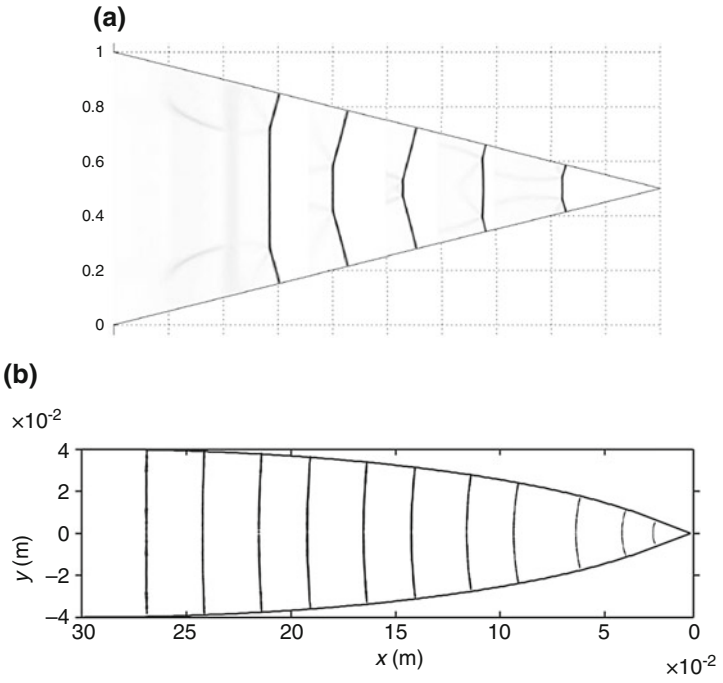

Fig. 3.86 Numerical schlieren images of convergence in (**a**) conventional axisymmetric conical section, from N. Apazidis private communication and (**b**) smooth transformation section, reproduced from [68], with the permission of AIP

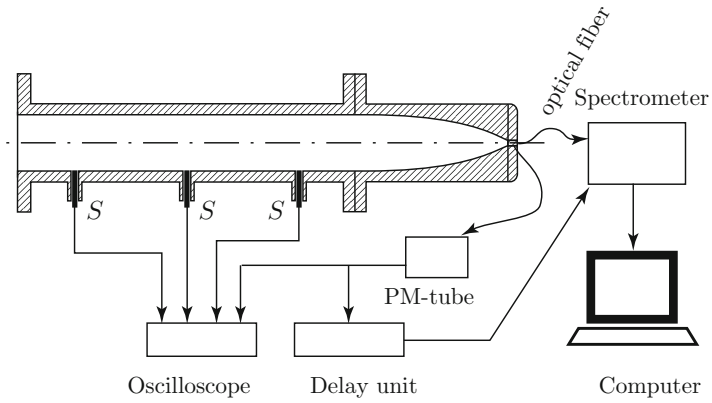

Fig. 3.87 Schematic diagram of the spectrometric setup. The photomultiplier (PM) tube detects the first light from the shock wave and triggers a delay unit which in turn triggers the spectrometer. An oscilloscope stores the signals from the PM tube and the shock sensors $S_1 - S_3$, reproduced from [68], with the permission of AIP

a 1.5 mm thick quartz window mounted in a frame of the steel tube and secured by brass sleeves. The sketch of the experimental setup with time-delay, photometric, and spectroscopic equipment is displayed in Fig. 3.87.

A series of experiments were conducted with argon as a test gas and helium as driver. Spectroscopic measurements of the intense light radiation of the compressed argon plasma at the moment of implosion were performed. The spectra of radiation at various instants after implosion were obtained and the corresponding temperature deduced by a curve fit to Planck's function:

$$I_\lambda(\lambda, T) = \frac{2hc^2}{\lambda^5} \frac{1}{\exp(hc/\lambda kT) - 1}, \tag{3.22}$$

where I_λ is the intensity per unit wavelength λ, h Planck's constant, c the speed of light, and k Boltzmann's constant. The resulting black-body curves with corresponding temperatures at various instants after implosion are shown in Fig. 3.88 with a maximum temperature of 27,000 K.

Experimental values of the temperature variation with time after implosion are illustrated in the next Fig. 3.89.

Figure 3.90 shows damage by the focused shock on the 5 mm quartz glass window insulating the opening at the end of the conical test section after a series of runs.

This investigation showed the possibility of obtaining extreme conditions in the argon gas compressed by a converging spherical shock. The features of the experimental equipment used in this work were such that the spectroscopic temperature measurements could be initiated only with a 250 ns delay after the implosion. This means that the question of maximum possible temperatures during and right after the implosion was still an open one. Experimental, theoretical, and

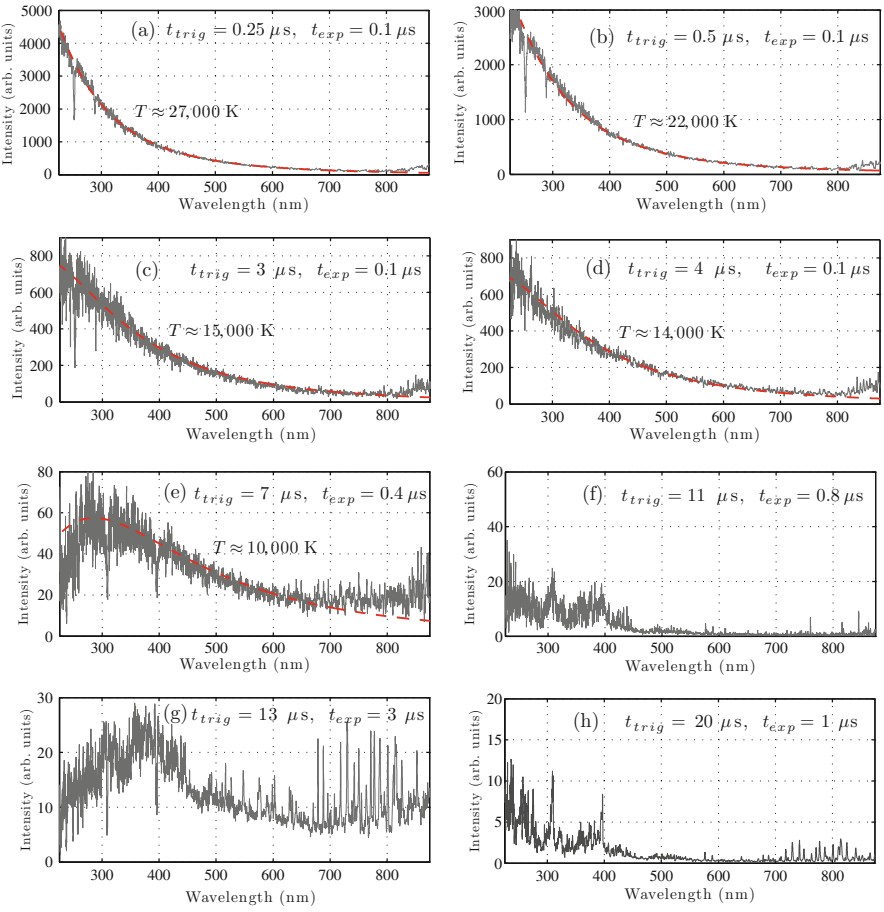

Fig. 3.88 Spectra from converging shock in argon. Initial $M_S = 3.9$, $p_1 = 10.0$ kPa. The spectra are taken during separate runs at different times relative to the shock implosion, t_{trig}, and with varying exposure times t_{exp}. For (**a**)–(**e**), black-body curve fits (dashed, red) are also plotted in the spectra, reproduced from [68], with the permission of AIP

numerical work by Liverts and Apazidis [74] addressed this question in greater detail.

Experimental investigations were carried out in the upgraded shock tube facility at KTH [74]. The shock tube was equipped with a fast-opening valve (FOV) instead of membranes separating the driver from the driven section. Shock generation was fully automated substantially reducing the run time as compared to the manual control. The general view of the shock tube with a FOV and conically shaped test section is shown in Fig. 3.91. A corresponding sketch of the diagnostic setup is shown in Fig. 3.92.

The thermodynamics of the final spherical convergence was investigated theoretically and numerically by means of Whitham's theory of GSD combined with jump

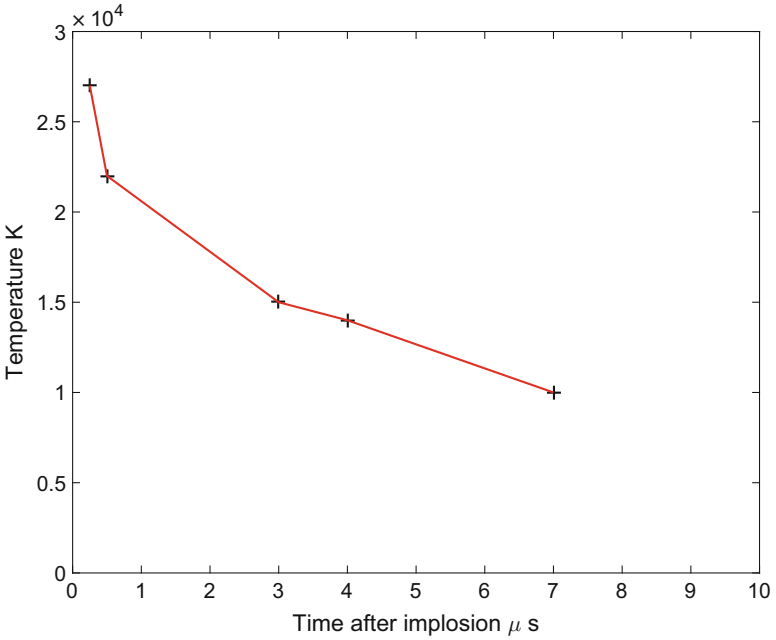

Fig. 3.89 Temperature variation with time after implosion, data, reproduced from [68], with the permission of AIP

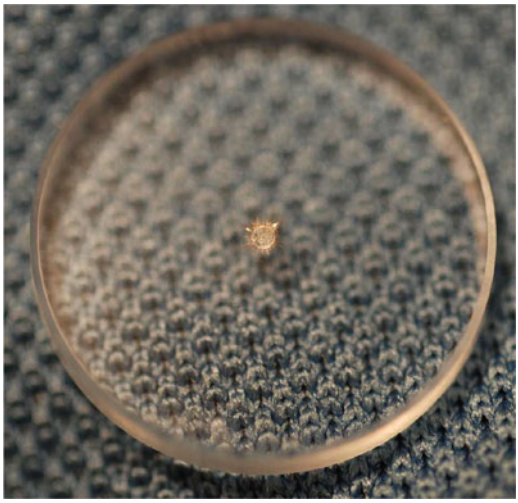

Fig. 3.90 Viewing quartz glass damage caused by the focused shock, reproduced from [68], with the permission of AIP

relation over the shock interface that account for real gas effects including multiple-level ionization, excitation, Coulomb interaction, and radiation. The ionization products were calculated using the Saha equations:

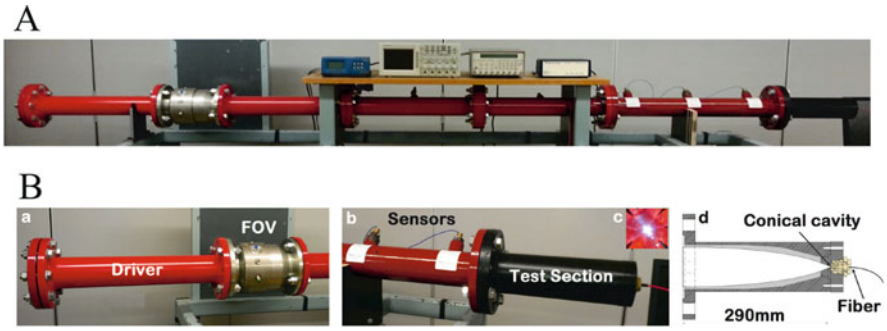

Fig. 3.91 (**a**) General view of the shock tube. (**b**) Enlarged view of the driver with FOV and conically shaped test section, from M. Liverts private communication

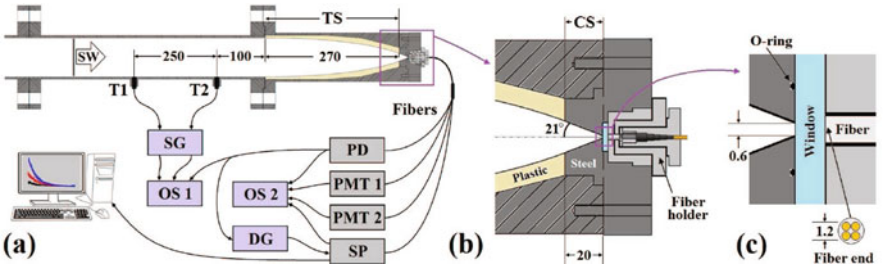

Fig. 3.92 (**a**) Schematic diagram of shock tube and diagnostic setup. *SG*, signal conditioner; *OS*, oscilloscope; *DG*, delay generator; *PD*, photodiode; *PMTs*, photomultiplier tubes equipped with bandpass interference filters (220 and 405 nm CWL); *SP*, spectrometer; (**b**), zoomed area of the conical segment; (**c**) zoomed area of the conical tip, optical window, and fiber details, reproduced from [74], with the permission of APS

$$\frac{\alpha_{i+1}\alpha_e}{\alpha_i} = \left(\frac{2\pi m_e kT}{h^2}\right)^{3/2} \frac{m_A}{\rho} \frac{2Q_{i+1}}{Q_i} \exp\left(-\frac{I_{i+1}^{\text{eff}}}{kT}\right) \tag{3.23}$$

where m_e is the electron's mass, k is the Boltzmann's constant, h is the Planck's constant, m_A is the mass of argon atom, α_e is the electrons concentration per number of atoms, α_i is the ions concentration in ionization stage i per number of atoms, Q_i is the electronic partition function in the ionization stage i, and T is the absolute equilibrium temperature. The ith effective ionization potential is reduced due to Coulomb interactions $I_i^{\text{eff}} = I_i - \Delta I_i$, where $\Delta I_i = (i+1)e^2/4\pi\varepsilon_0 r_D$, where e is the electrons charge, ε_0 is the vacuum permittivity, and r_D is the Debye screening radius.

The specific internal energy per unit mass of the monatomic gas accounting for non-ideal gas effects was used as:

$$e = \frac{3}{2}(1+\alpha_e)RT + \frac{1}{m_A}\left[\sum_{i=1}^{l}\alpha_i \sum_{j=1}^{i} I_j^{\text{eff}} + \sum_{i=0}^{l}\alpha_i \frac{U_i}{Q_i}\right] + \sigma T^4 - \frac{kT}{8\pi\rho r_D^3} \tag{3.24}$$

where R is the specific gas constant, $\sigma = 7.57 \cdot 10^{-16}\,\mathrm{J\,m^{-3}\,K^{-4}}$, and U_i is the total excitation energy of atom/ion in ionization stage i. The terms represent respectively translation, ionization, excitation, radiation energies and the last term is due to the Coulomb interaction.

The following equation of state including the Coulomb correction and the radiation pressure was used

$$p = (1 + \alpha_e)\rho RT - \frac{kT}{24\pi r_D^3} + \frac{\sigma}{3}\rho T^4 \tag{3.25}$$

The enthalpy of the gas is then given by $h = e + p/\rho$. Complimented with charge conservation equations, the resulting nonlinear system was solved using Newton method iterative approach. Figure 3.93 shows the Mach number amplification in the transformation section (TS) as the shock travels along 270 mm long transformation section. At the beginning of this section we have the initial Mach number M_0 which is amplified to M_S at the end of this section as the shock enters the final 20 mm long conical section (CS) where the final convergence is completed.

The converging shock front trajectory including the real gas effects was plotted and compared with the ideal gas trajectory at the same initial Mach number, $M = 8$. The results are shown in Fig. 3.94

As one can see the real gas effects, mainly ionization have a limiting effect on shock wave speed, increasing the value of power-law exponent in Guderley solution for argon ($\gamma = 5/3$) from 0.688 in ideal gas to 0.752 in real gas. To obtain the details of the ionization process in argon during and right after implosion photomultiplier tubes PM equipped with 220 and 450 nm bandpass interference filters were connected through optical fibers to a small opening at the apex of

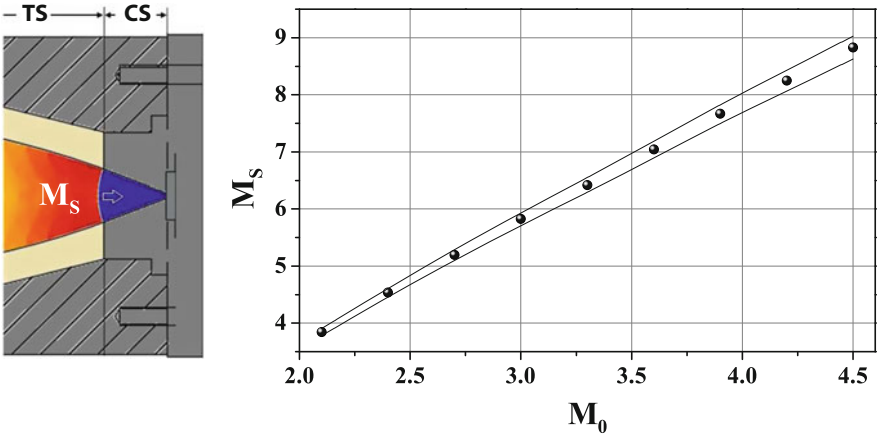

Fig. 3.93 Mach number amplification in the transformation section, reproduced from [74], with the permission of APS

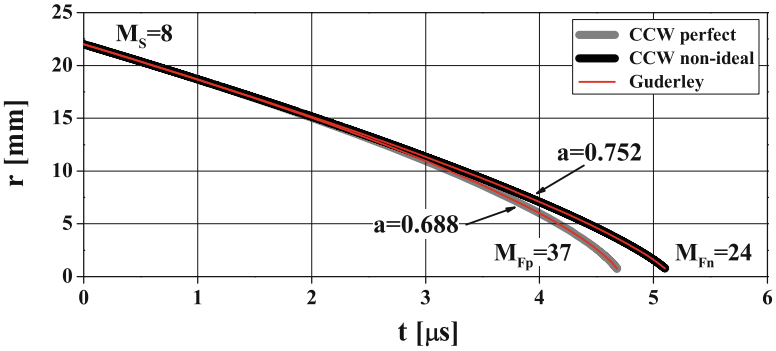

Fig. 3.94 Comparison between the calculated shock front trajectories in non-ideal effects vs perfect gas, reproduced from [74], with the permission of APS

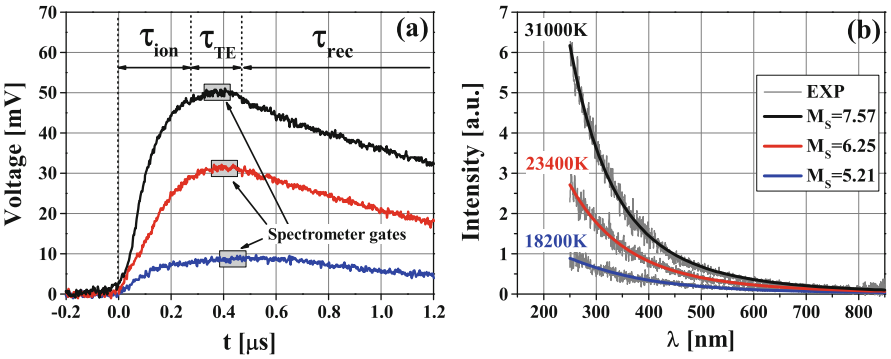

Fig. 3.95 (**a**) PM intensity curve and (**b**) flash light spectra fitted with Plank's law, reproduced from [74], with the permission of APS

the end conical section. The PM signals identified three regions of the electron density variation: (a) ionization τ_{ion}, (b) local thermal equilibrium τ_{TE}, and (c) recombination τ_{rec}. The regions correspond to the increase, plateau, and decrease regions of the PM signal curve, respectively. The spectroscopic measurements are then conducted at the local thermal equilibrium window, and the corresponding temperature is deduced by the fit to the Planck's black-body curve. The results of these measurements are shown in Fig. 3.95.

Figure 3.95a shows the three regions for different values of the Mach number at the beginning of the final conical convergence section, namely, $M_S = 5.21$, 6.25, and 7.57. The time of ionization varies between 250 and 400 ns with shorter times for stronger shocks. The local thermal equilibrium τ_{TE} when the spectroscopic measurements are conducted lasts for about 100 ns. Black-body temperatures deduced from Plank's law for corresponding values of the Mach number are shown in Fig. 3.95b with highest value of T =31,000 K. Further calculations based on the presented model show that the real gas temperatures to be expected are more than an order of magnitude lower than for a corresponding ideal case. For example,

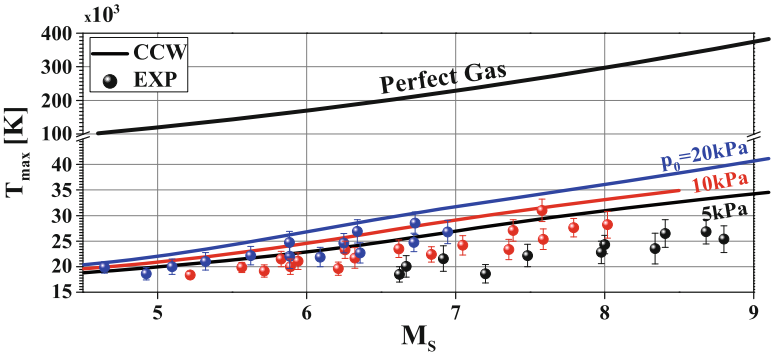

Fig. 3.96 Comparison of final implosion temperatures for perfect and real gas as function of Mach number, reproduced from [74], with the permission of APS

extending the calculation toward the shock radius $r = 50\,\mu\text{m}$, the perfect gas approach predicts temperature of order of 1.5 million K behind the incident shock front with Mach number $M \approx 125$, while in the non-ideal case, it is limited to 55,000 K and $M \approx 62$ (Fig. 3.96).

The main results of this investigation show that non-ideal effects become significant for Mach number $M > 10$ and dominate for $M > 20$. Evidently ionization presents a large energy sink to account for this reduction in temperature. In practical situation the highest possible temperatures in argon gas obtained by converging spherical shock are expected be of order of 30,000 K.

3.8 Shock Focusing in Water

"While a large number of investigations have been carried out on the propagation of shock waves in air, there has been very little reported concerning their formation and transmission through water, especially when the waves have been produced by impact." We can read this quote from a very nice and early investigation by J.H. McMillen in 1945 [78]. A large number of investigations of shock generation and propagation in water have been conducted since it would probably be fair to say that their number is still much less than those of shock propagation in gases. One can think of several reasons for that, one of which is the existence and availability of a shock tube—a simple and ingenious device that has been in the service of the researchers worldwide for a period of last 100 years. The shock tube is however used to study shocks in gases. How can one create a shock in water? There are several methods used by the researchers, one of which is illustrated with great elegance in this early work that we cited in the beginning of this section. The author used a high-velocity impact of small spherical particle hitting the free water surface. A spark shadowgraph image of a slightly elliptic shock generated by a high-velocity impact of a 3.2 mm steel sphere is shown in Fig. 3.97.

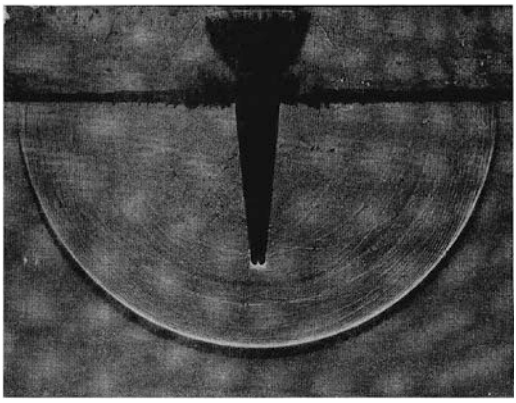

Fig. 3.97 Spark shadowgraph image of a shock wave after advancing 78 mm into the water by a 3.2 mm steel sphere at an impact velocity of 1073 m/s, reproduced from [78], with the permission of APS

One of the interesting features of this figure beside the sharp and distinct image of the shock front in water created by the impact is the luminescence around the front tip of the air-filled cavity created by the high-velocity particle. The author notes that the luminescent cusp around the tip of the cavity gradually fades as the sphere slows down.

Physical properties of water differ in many respects important for shock generation and propagation from those of gases. Water density is about 1000 times greater, and water is considered to be incompressible in a broad number of scenarios when pressure variations are moderate. The incompressibility assumption is certainly not true in the above situation since it would lead to infinite speed of the signal propagation. As we know the speed of sound in water is about 1500 m/s which is about 4.4 times greater than in air at normal conditions. In this example the small metal sphere is traveling at 1073 m/s when it hits the water surface and the shock wave is thus generated by a subsonic source. The average value of the Mach number in this case is estimated to $M = 1.04$. For a gas this would mean a weak, near-sonic wave, with a pressure ratio of approximately 1.1 over the shock. In the present case, the pressure ratio over the shock is 462! This enormous difference can be explained by a different structure of the equation of state (EOS) for water compared to that of an ideal gas. The Tait equation of state for compressible liquids, see, e.g., [62], has the following structure:

$$p(\rho) = (p_0 + B)\left(\frac{\rho}{\rho_0}\right)^{\gamma_2} - B, \tag{3.26}$$

with ρ_0 and p_0 being the reference density and pressure, respectively, and B a pressure-like constant describing the stiffness of the liquid. The numerical values of $B = 4050$ atm and $\gamma_2 = 6.68$ can be found in, e.g., [30]. One can see that this equation of state relates small density variations to very large pressure variations.

Another and maybe even more spectacular difference between water and gas is the ability to sustain large negative pressures due to strong cohesive forces. In a recent experimental study by El Mekki Azouzi et al. [44], the authors measure

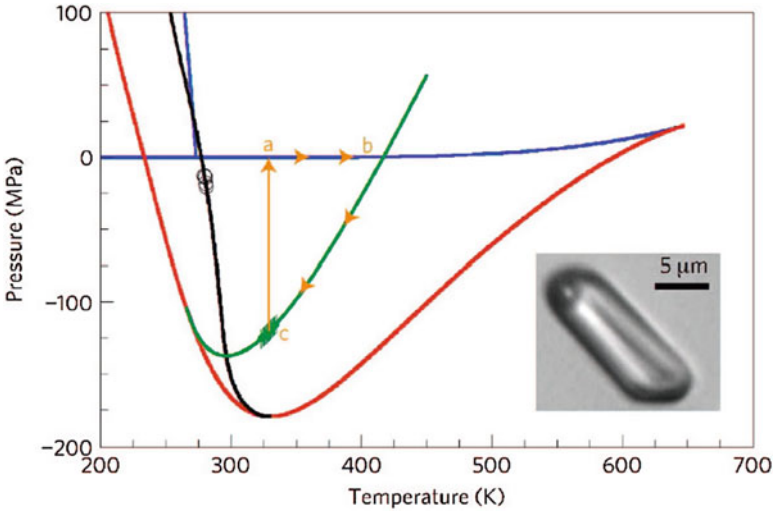

Fig. 3.98 Green curve showing the negative pressures sustained by water in a quartz inclusion along isochor at $\rho = 922.8\,\mathrm{kg\,m^{-3}}$, reproduced from [44], with permission from Springer

negative pressures as low as −140 MPa before water breaks by cavitation. Negative pressures are produced by fluid inclusion of water in quarts. Figure 3.98 illustrates the negative pressure along the isochor (green curve) obtained in this study. This study represents a slow, quasi-stationary process. Negative pressures in water are however a natural part of a dynamic process of wave propagation. Although the theoretical threshold for cavitation in water is estimated at about −150 MPa [32, 46, 125], the appearance of cavitation is usually reported at much higher limits of around −30 MPa. This is often attributed to the existence of so-called nucleation sites or impurities in the form of minute spherical gas bubbles, gas trapped in crevices of solid particles or walls of the vessel containing liquid [107]. Negative pressures and cavitation in water are often connected to shock wave propagation created by underwater explosions. The strong compression wave is reflected as an expansion or tension wave at the free surface. Wilson et al. [121] described a method where the tensile stress of the wave reflected from the free surface was measured by the initial spray dome velocity V_0 by the relation

$$V_0 = \left(\frac{2}{\rho U}\right)\left(p - \frac{F}{2}\right), \tag{3.27}$$

where p is the maximum explosion pressure, ρ is the liquid density, U is the wave speed, and F is the maximum tension of the reflected wave. The value of F for the cavitation threshold found by this method was 8.0 atm for ordinary water. Trevena and co-workers [107] also used a bullet-piston method which is also based on the reflection of the pressure pulse in liquid from a free liquid surface. The pulse is created by a bullet hitting a piston at a lower end of a vertical cylindrical tube containing liquid. When the pressure pulse is reflected from the free surface of the

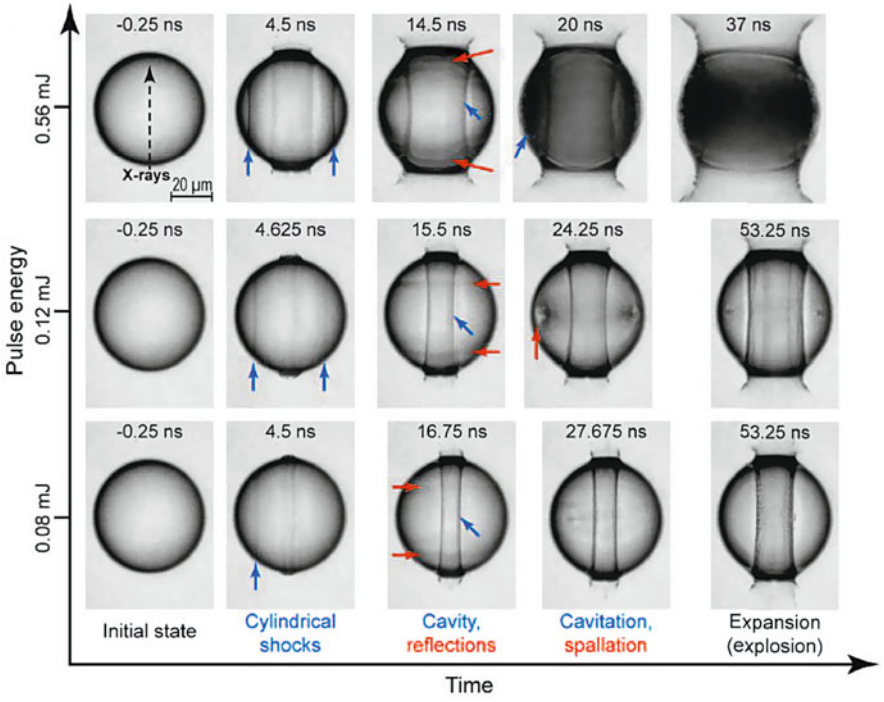

Fig. 3.99 A series of images of a 55 µm water drop showing generation propagation and reflection of a shock generated by an X-ray laser pulse, reproduced from [98], with permission from ACS

liquid at the upper end of the tube, it is reflected as a tension wave in liquid. The pressure pulses of 300 atm with a pulse duration of 500 µs were reported. Many researchers argued that the low cavitation threshold as compared to the maximum theoretical value observed in dynamic processes is due to relatively large pulse duration. Recently a threshold of below −100 MPa was evaluated in experimental work of Stan et al. [98]. The pressure pulses of nanosecond rise time were created by X-ray laser pulses at the internal surface of water drops.

Figure 3.99 shows how the initial shock is reflected from the bubble interface as an expansion wave that is seen to focus at the locations close to the interface where the spallation and cavitation occurs.

In another recent work, shock propagation within a two-dimensional droplet was investigated by schlieren imaging [96]. The shock was generated by exploding wire technique and the droplet, or thin water column was placed in a rectangular test chamber with transparent upper and lower glass plates allowing for visualization through schlieren imaging. The general view of the experimental setup is shown in Fig. 3.100. The length of the test section is 200 mm, and the distance between the lower and upper plates is 5 mm, creating an essentially two-dimensional channel for shock propagation, Fig. 3.101.

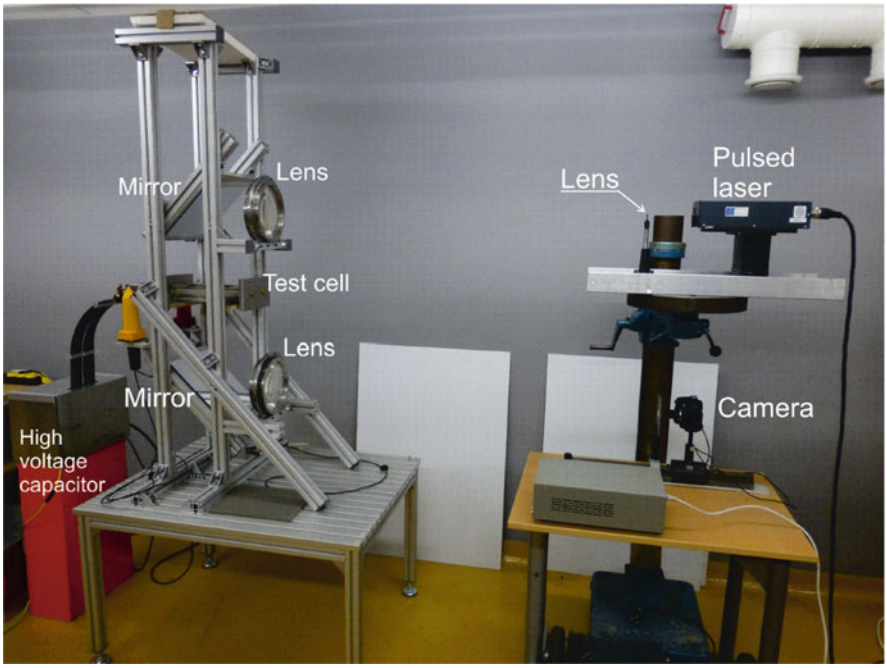

Fig. 3.100 General view of the experimental setup, from N. Apazidis private communication

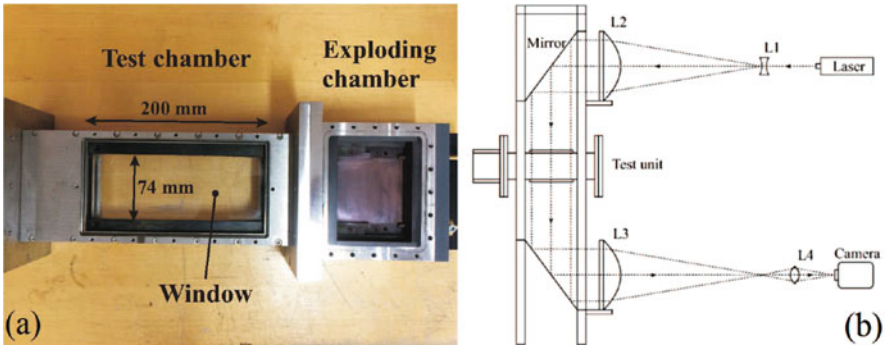

Fig. 3.101 Upper view of the test unit, reproduced from [96], with permission from APS

The blast wave is generated by letting high current pass through a thin copper wire stretched between the electrodes over the width of exploding chamber. A 22 mm diameter two-dimensional water droplet with straight walls is generated by hydrophobic coating between the lower and upper glass plates and placed in the test chamber at a distance of 200 mm from the explosion source, Fig. 3.102.

Figure 3.103 shows a sequence of images of shock propagation within a two-dimensional water droplet. The strength of the blast wave is $M = 2.4$ as it impinges on the droplet. Figure 3.103a and b show the initial shock in air and the

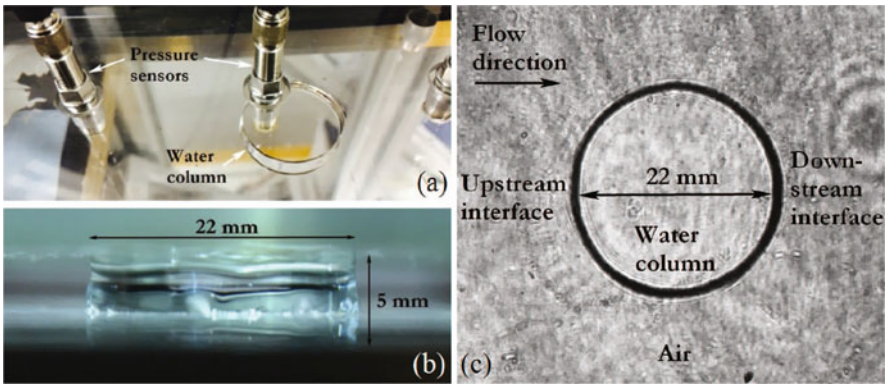

Fig. 3.102 Two-dimensional water droplet created by hydrophobic coating, reproduced from [96], with permission from APS

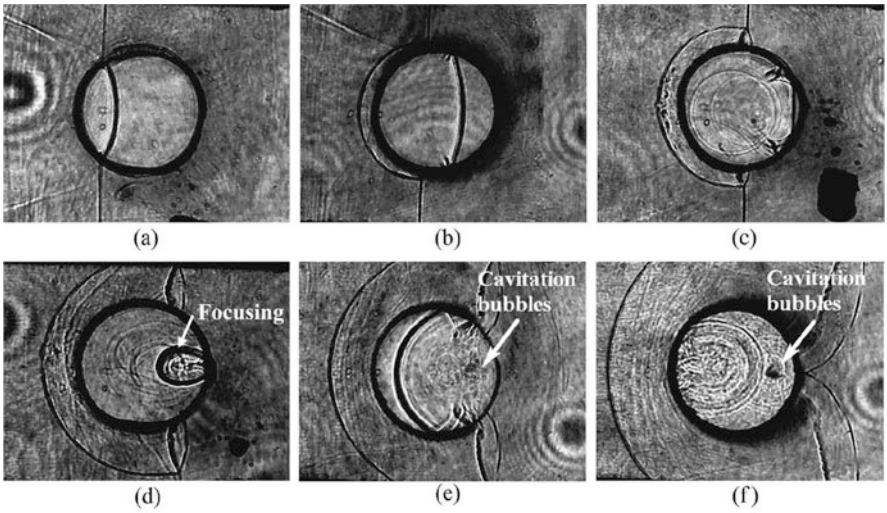

Fig. 3.103 Shock propagation and reflection inside the droplet at various time instants (**a**)–(**f**), reproduced from [96], with permission from APS

transmitted shock in water droplet, propagating with a higher speed. Figure 3.103c shows appearance of the expansion wave as a result of shock reflection from the droplet interface. In Fig. 3.103d the expansion wave is seen to focus in the vicinity of the droplet boundary creating a focused region of negative pressures leading to cavitation seen in Fig. 3.103e,f.

It is interesting to note at this point that the focusing process leading to extreme conditions in the focusing region results in the decrease of pressure with large negative pressures in water in this case of an expansion wave contrary to focusing of the compression wave which leads to the increase in pressure.

Negative pressures generated by tensile stresses exist not only as a result of shock reflection from a liquid-gas interface but also in a trailing tensile wave following the compression wave. This is an important mechanism of shock propagation in water that is used in medical applications such as shock wave lithotripsy (SWL). This method has been successfully used during the past three decades in clinic treatment of kidney stones. The principle is based on generating a sharp pressure pulse at one of the foci of a truncated ellipsoidal reflector thus generating an outgoing spherical blast wave which after reflection converges at the kidney stone placed at the location of the second focal point of the ellipsoidal reflector.

The pressure pulse is often generated by a spark discharge at the focus of the ellipsoidal reflector as, e.g., in Dornier HM3, the first commercial lithotripter system [19, 28], schematically illustrated in Fig. 3.104.

The axial pressure distribution was computed by nonlinear beam propagation model [29], which was able to reproduce the general waveform, measured by Coleman and Saunders [31]; see Fig. 3.105. Note the negative pressure produced by the trailing tensile wave.

Sommerfeld and Müller [97] studied focusing of plane shock waves and spherical blast waves by parabolic and ellipsoidal reflectors. The authors used a second-order Godunov-type method to obtain a numerical solution to axisymmetric Euler equations with the Tait equation of state for water. They considered focusing of

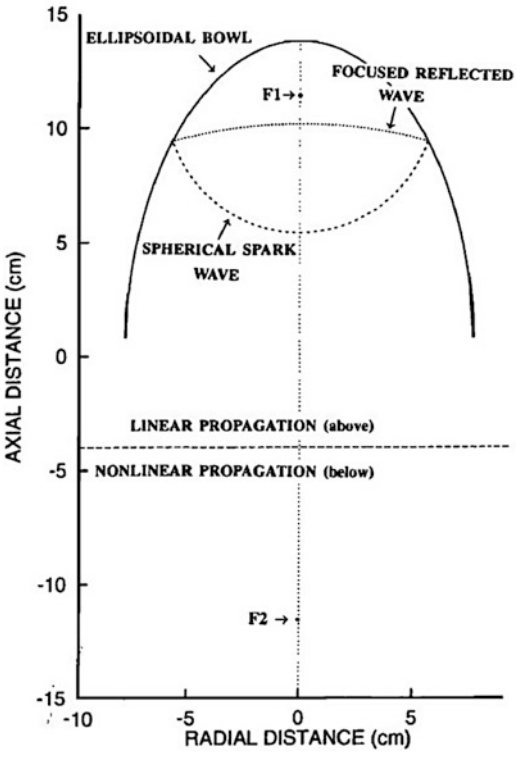

Fig. 3.104 Schematic drawing of the geometry of Dornier HM3 lithotripter, reproduced from [28], with the permission of AIP

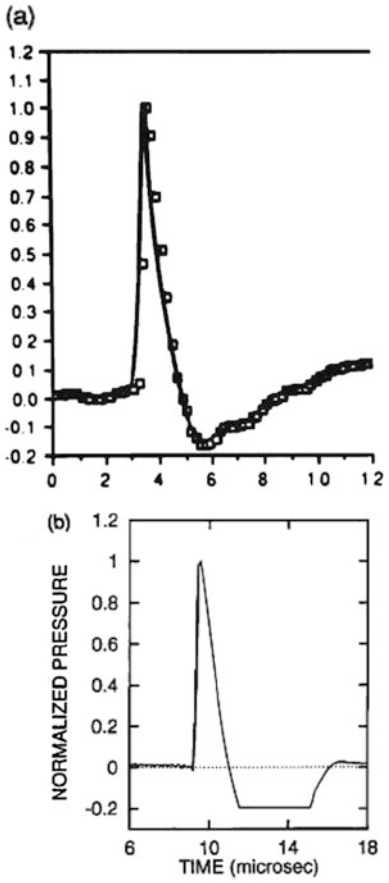

Fig. 3.105 Measured and computed waveforms. (**a**) Waveform measured by Coleman and Saunders [31]. (**b**) Corresponding computed waveform, reproduced from [28], with the permission of AIP

a plane shock by a parabolic reflector. For stronger shocks it was found that the focal point shifted closer to the reflector surface as compared to geometrical focus. The geometrical focus is also transformed to a focusing region since the strength of the converging shock depends on the location of the reflection point and is greater for outer regions of the reflector. The authors proposed a modified shape of the reflector to compensate for this effect so that the reflected shock will converge at the geometrical focus of the parabolic geometry. Experimental shadowgraph and schlieren images documented the focusing of a blast wave generated by spark discharge from the ellipsoidal reflector and are illustrated in Fig. 3.106. Figure 3.106 shows successive shock fronts with focusing in the central portions and expansion in the outer regions due to the reflector edges.

Gustafsson [53] investigated a similar problem in a study initiated by Lesser, although in plane geometry. He considered a possibility to extract high pressures at a focal point of an elliptic reflector by imposing impulsive pressure at the other focus of the reflector. Gustafsson studied the problem in the linear approximation by geometrical acoustics. Figure 3.107 shows the schematic of the geometry and

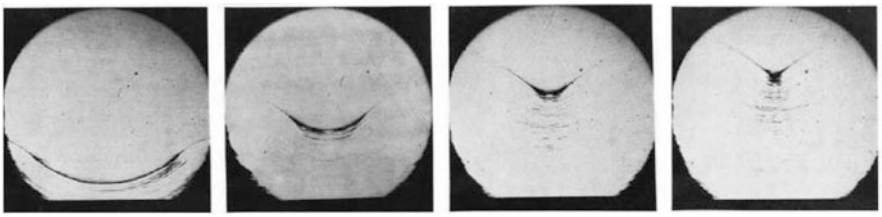

Fig. 3.106 Shadowgraph images of the converging shock wave reflected from an ellipsoidal reflector, reproduced from [97], with permission from Springer

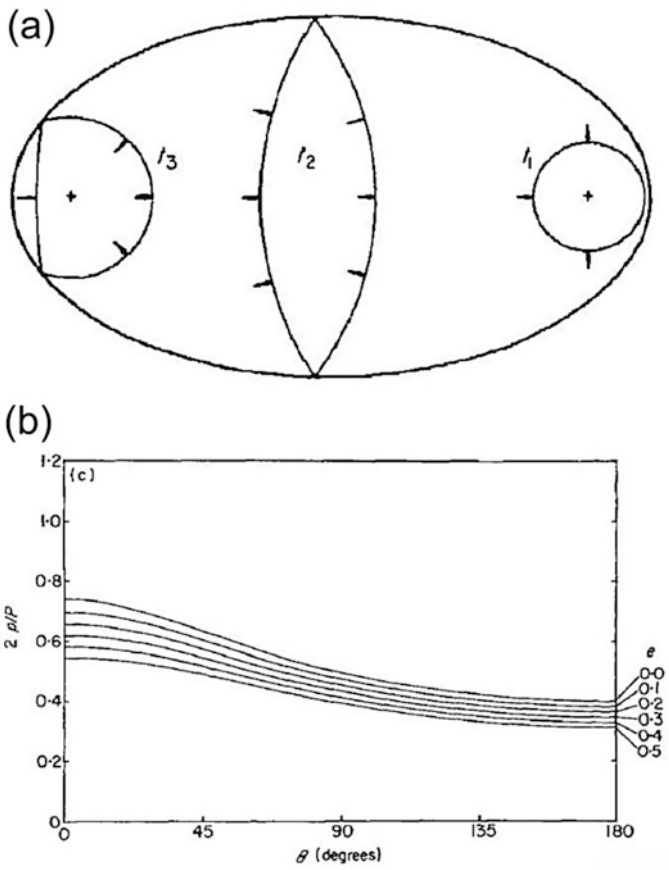

Fig. 3.107 (**a**) Schematic of shock propagation in an elliptic reflector. (**b**) Pressure distribution around the converging shock for various eccentricities, reproduced from [53], with permission from Elsevier

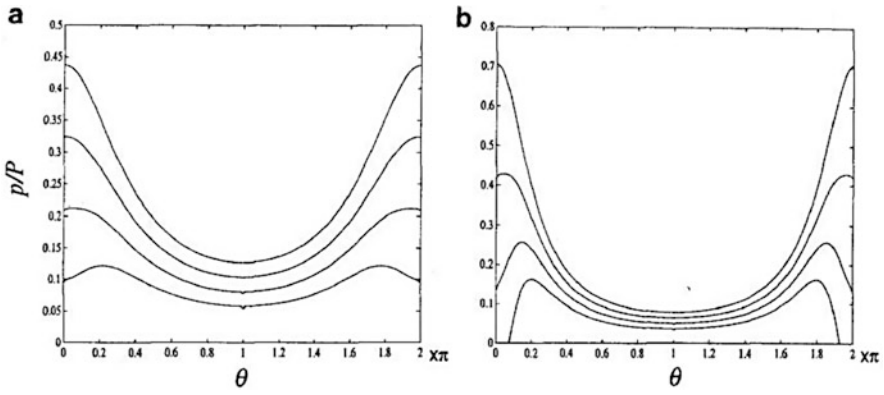

Fig. 3.108 Pressure distribution around successive converging wave fronts for various eccentricities (**a**) $e = 0.3$ and (**b**) $e = 0.5$, reproduced from [6], with permission from Springer

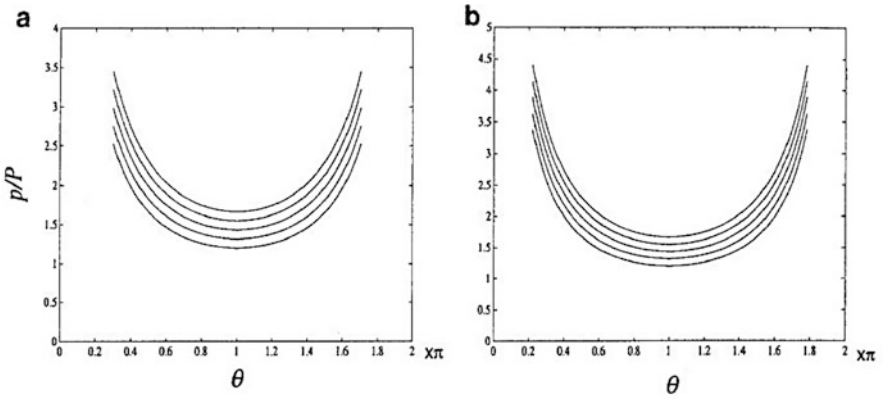

Fig. 3.109 Pressure distribution around successive converging wave fronts at various distances. (**a**) Two focal distances and (**b**) four focal distances, reproduced from [6], with permission from Springer

linear shock propagation in the elliptic chamber as well as pressure distribution around the converging shock front at some distance from the focal point. One can note that the maximum and minimum pressures are obtained on the axis of the reflector with maximum for $\theta = 0$ that is at a point which is closer to the first focus where the shock is generated. This follows the general trend described in [97] with a higher strength of the shock emanating from the reflection closer to the point of shock generation.

Apazidis [6] used similar techniques of geometrical acoustics in axisymmetric ellipsoidal and paraboloidal reflectors. The pressure distribution around the converging shock front in an ellipsoidal reflector follows the same trend as in [53] although with a greater maximum to minimum pressure ratio along the front, as shown in Fig. 3.108. Corresponding pressure distributions for the case of a paraboloidal reflector are shown in Fig. 3.109.

An ellipsoidal reflector was also considered by Hamilton [55], by geometrical acoustics and use of Kirchhoff integral to account for the effect of diffraction of the reflected field. The pressure distribution of the reflected wave is evaluated along the axis of the reflector for various types of the initial signal. Figure 3.110 shows comparison of the computed pressure pulses along the axis of the ellipsoidal reflector with measurements.

More recently this technique was revisited by Sankin et al. [93] and applied to focusing of laser-generated shock waves by a truncated ellipsoidal reflector. Numerical computations of the reflected pressure pulses at the focal region of the reflector were compared with measurements. Spherical diverging blast waves with peak pressures in the range 2.1–5.9 MPa were produced by 5 ns laser pulses at the focus of the reflector. The reflected pressure pulse had a leading compressive wave with peak pressure of 26 MPa with 0.1–0.2 μs pulse length, followed by a trailing tensile wave with a peak pressure of −3.3 MPa with 0.2 μs duration. Figure 3.111 illustrates generation at the first focus F_1 the and extraction at the second focus F_2 of the measured pressure profiles generated by laser pulses in the truncated ellipsoidal reflector [93].

A numerical study of shock induced bubble collapse under a typical lithotripter pressure pulse was conducted by Johnsen and Colonius [61]. The authors considered a spherical gas bubble subjected to a plane shock wave with a typical pressure profile at the converging focal point of the reflector; see Fig. 3.112.

Numerical solution to Euler equations with water phase modeled by the Tait equation of state revealed some interesting features of bubble dynamics under the impulsive pressure load from the shock wave. Initially slow bubble motion in the direction of shock propagation is accelerated as the shock reaches the distal bubble side inducing bubble contraction and deformation of the interface. A high-velocity liquid jet hits the distal interface of the bubble dividing it into two separate regions; see Fig. 3.112 (Fig. 3.113).

It is noteworthy that Johnsen and Colonius [61] attribute the highest impulsive pressure load on the wall during bubble collapse to the action of the water-hammer shock at the distal bubble interface as shown in Fig. 3.114. The water-hammer-induced pressure load is substantially higher than the pressure load due to the initial shock.

Similar features of bubble dynamics under the action of impulsive pressure from a passing initially plane blast wave in water are also described in [7]. Figure 3.115 illustrates several stages of shock-bubble interaction. In Fig. 3.115a a transmitted shock in the bubble is seen to be bent by the interface and lags behind the incident shock in water. Water-hammer shock, right behind the downstream bubble interface, is seen in Fig. 3.115b. Note also the expansion wave marked by the yellow circle as well as two small high-pressure regions at the triple point location close to the bubble interface. Figure 3.115c show the focusing of the shock reflected from the downstream bubble interface resulting in the elongated high-pressure region at the axis stretching from the focal region to the water-hammer shock. Deformation of the bubble into two separate regions with counter-rotating vortices and creating a high-speed water jet with maximum velocities of 1100 m/s is illustrated in Fig. 3.115d–f. Figure 3.115e shows the powerful outgoing spherical blast wave emanating from the bubble collapse.

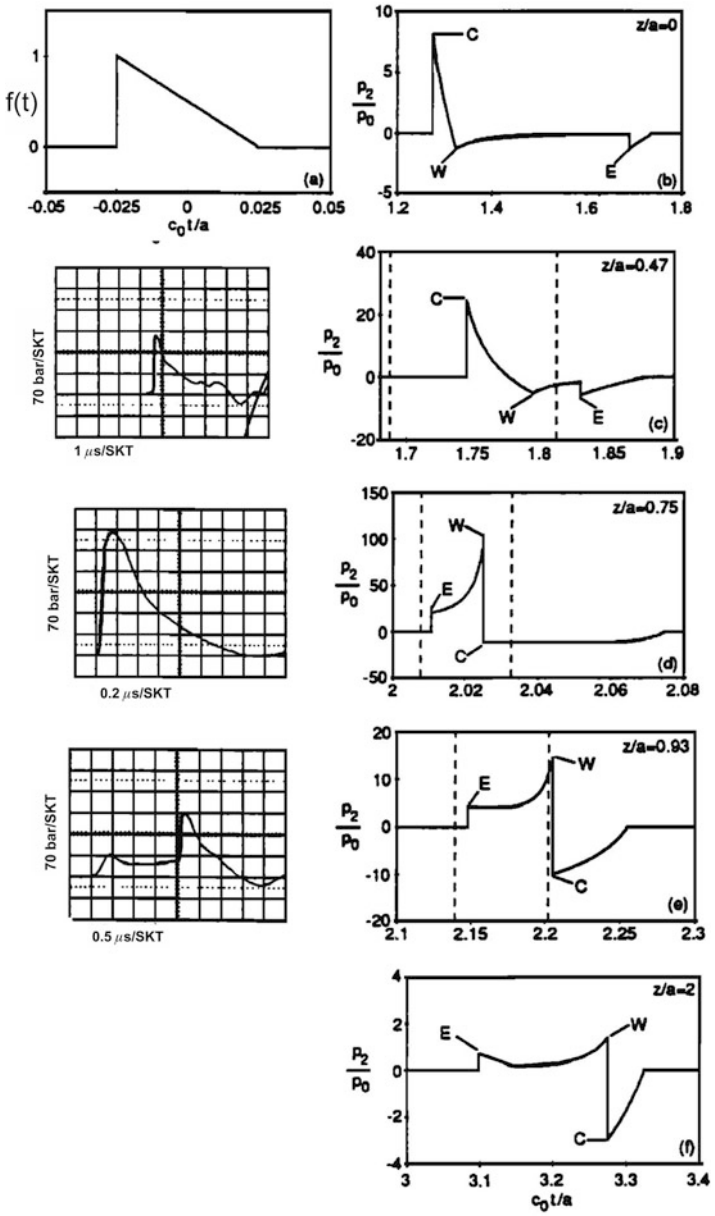

Fig. 3.110 Comparison of pressure pulses with measurements obtained in water by Müller [80], reproduced from [55], with the permission of AIP

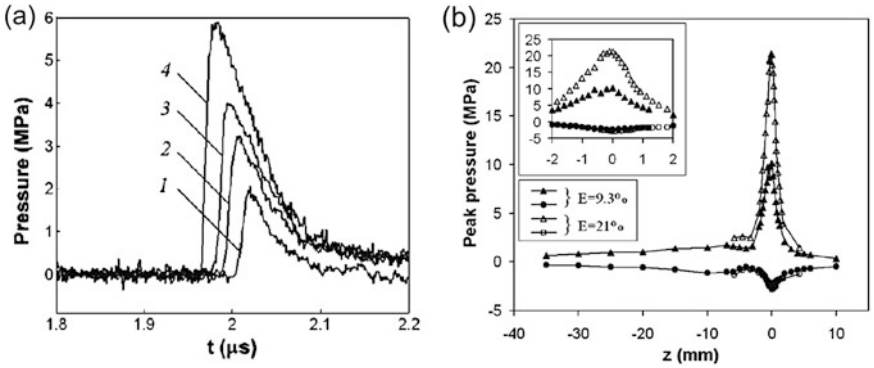

Fig. 3.111 (**a**) Initial at F_1 and (**b**) reflected at F_2 pressure pulses along the axis of the reflector. (**b**) Shows positive and negative peak pressures of the focused shock, reproduced from [93], with the permission of AIP

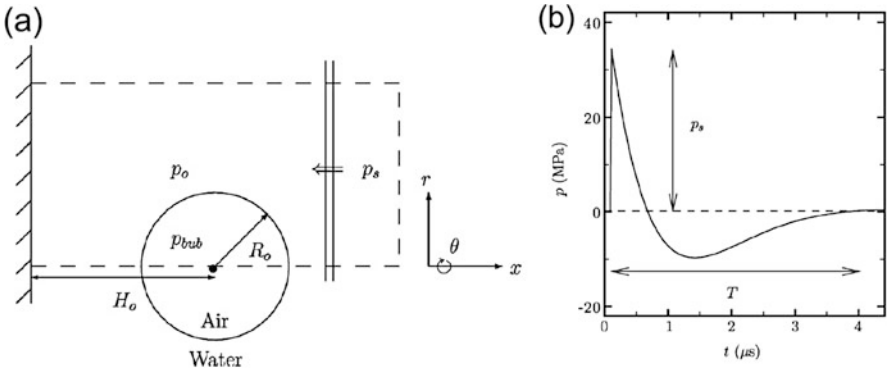

Fig. 3.112 (**a**) Schematic of the problem and (**b**) pressure pulse form at the focus, reproduced from [61], with the permission of AIP

In general the extreme conditions such as high pressures, temperatures, and densities due to focusing in gases become substantially more severe, especially with respect to pressures in liquids. This is due to a much higher density of, e.g., water as compared to air and at the same time very low compressibility of water. Such extreme conditions impose very high demands on the experimental rigs, vessels, and chambers containing liquid. The inner parts and walls of the test chambers are easily destroyed by the enormous impulsive pressures produced in liquid. Impulsive pressures in liquids are usually produced by various types of explosions or impacts, resulting in a blast wave profile propagating from the source of explosion. Various types of waves, plane, cylindrical, and spherical can be generated by so-called exploding wire technique, by a rapid discharge of a high-voltage capacitor through a thin copper wire. If the wire is confined by a thin test section, an initially cylindrical blast wave across the channel is transformed

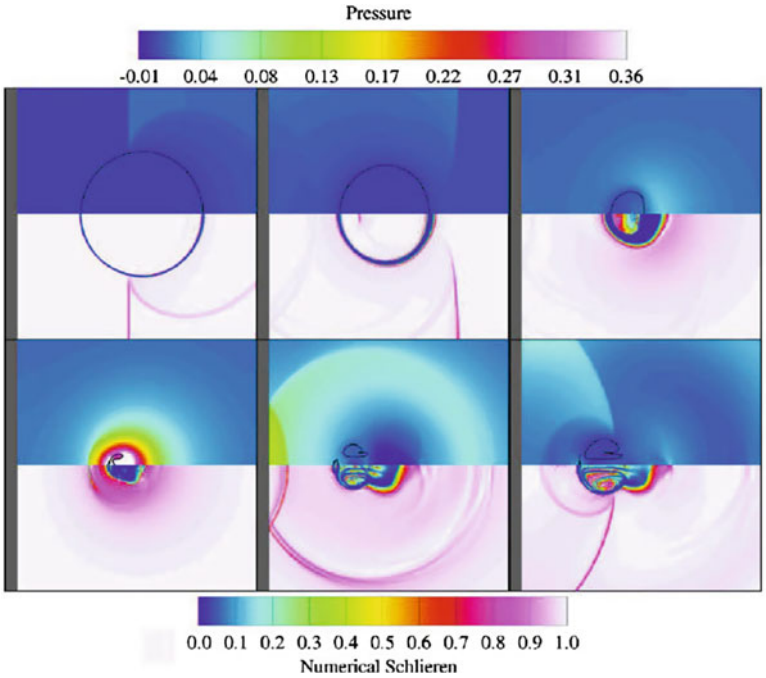

Fig. 3.113 Numerical schlieren of the bubble dynamics, reproduced from [61], with the permission of AIP

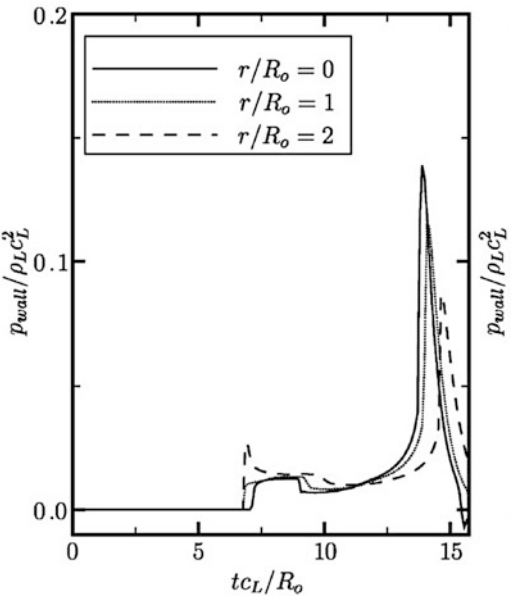

Fig. 3.114 Impulsive pressure load on the wall, reproduced from [61], with the permission of AIP

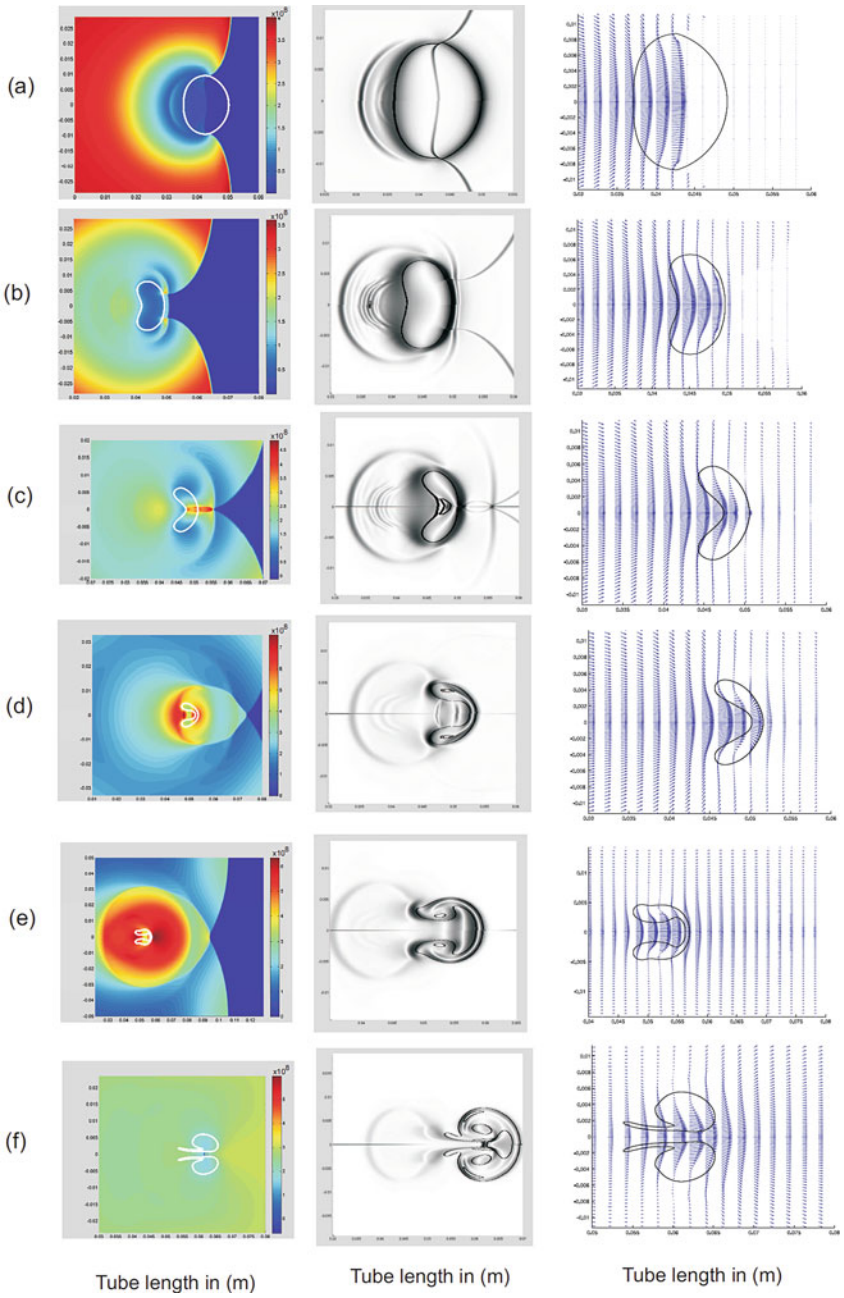

Fig. 3.115 Numerical pressure field, schlieren and velocity vector field under shock induced bubble collapse. (**a**) Tube radius in (m). (**b**) Tube radius in (m). (**c**) Tube radius in (m). (**d**) Tube radius in (m). (**e**) Tube radius in (m). (**f**) Tube radius in (m), reproduced from [7], with the permission of AIP

to a plane wave. However even a plane blast wave is rapidly attenuated due to the blast wave profile. The attenuation increases for an outgoing cylindrical blast and even more so for an outgoing spherical blast wave. While outgoing cylindrical or spherical blast waves are rapidly attenuated, converging blast waves undergo a drastic increase in strength as they approach the center of convergence. This feature gives an excellent opportunity to safely contain the extreme pressures produced by blast waves in liquid. If a cylindrical or spherical array of wires is placed in a liquid container at a large enough distance from the container walls, they will be able to withstand the attenuated outgoing blast wave. At the same time, the converging blast wave focusing at the center of the wire array will produce extreme pressures and energy densities inside the liquid. This idea is successfully utilized by a group of researchers from Technion led by Prof. Krasik. A series of publications of this group report pressures of order of several TPa, temperatures of ∼17 eV, and compression ratios of ∼8 in water [4]. The description of the experimental setup consisting of spherical wire array may be found in Antonov et al. [3, 4]. Such extreme conditions in water are obtained at the center of converging spherical shock generated by a spherical wire array, as shown in Fig. 3.116.

A high current pulse of 500 kA with a rise time of 300 ns is applied to a spherical copper or aluminum wire array generating a converging spherical shock in water. The authors tested combinations of wire arrays with 20, 30, and 40 mm diameters. The authors used 1D HD simulations taking into account the self-magnetic field gradient to obtain an estimate of the final pressure, temperature, and compression as the spherical shock wave is reflected from the center of implosion. They estimated that water volume with the diameter of ∼12 μm would be subjected to a 6.6 TPa pressure with temperature of 17 eV and have a compression ratio of 9. Members of this research group have also looked into the question of stability of the converging cylindrical shock [71]. The converging cylindrical shock is generated by cylindrical

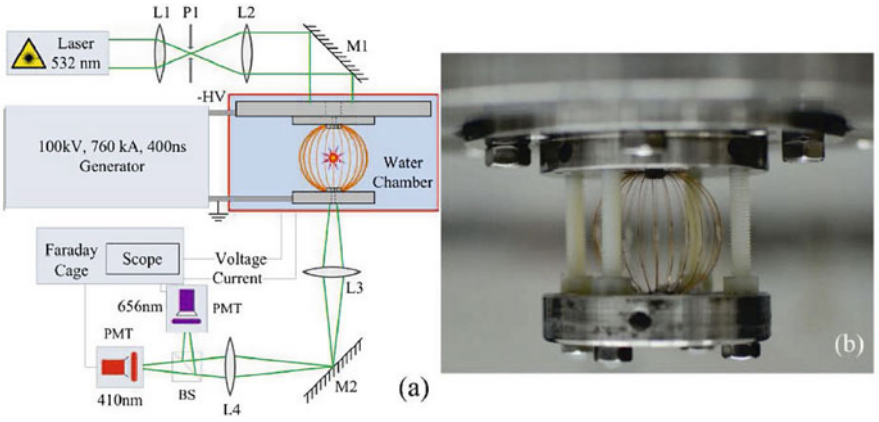

Fig. 3.116 (**a**) Schematic of the experimental setup. (**b**) External view of a 30 mm diameter spherical wire array, reproduced from [3], with the permission of AIP

Fig. 3.117 General view of the cylindrical wire array of 40 Cu wires, reproduced from [71], with the permission of AIP

wire array, as shown in Fig. 3.117. They argued that the converging cylindrical shock in water is less sensitive to the inherent instability as compared to shock convergence in gas due to the low compressibility of water. The authors conducted two-dimensional hydrodynamic simulations to investigate the growth of various type of perturbations of the shock front and found that the initial small-scale perturbations of the shock front were weakly unstable. It is interesting to note that their results correlated well with the results of previous investigations such as [39, 105], and [40] showing various modes of instabilities as the ones displayed in Fig. 3.118.

The just mentioned research shows that the extreme conditions that may be achieved by shock wave focusing are demonstrated to the fullest by spherical shock wave convergence in water resulting in very high-energy density at the center of convergence. It is remarkable that this high-energy density is obtained by only a few kJ of input energy generating the explosion of the spherical wire array. In [5] the authors conducted experimental diagnostics of the warm dense matter at the focal region of underwater explosion by analyzing the data of power and spectrum of the light emission from an optical fiber, data from explosion of a copper tube, as well as time-dependent resistor placed at the center of convergence. Based on these measurements and numerical simulations, they estimated the pressure at the vicinity of implosion origin to reach values of at least 10^{11} Pa. Figure 3.119 shows the damaged copper tube with outer radius of $r \approx 0.5$ mm and wall thickness $d \approx 0.1$ mm placed at the center of implosion.

Converging shocks in water were also experimentally investigated by Eliasson et al. [43]. This work studied the effects of the material properties of the material surrounding the water cavity. Three types of confinement materials were chosen for the experiments: rubber (Solithane), plastic (polycarbonate), and metal (aluminum). The three materials were chosen such that the shock speed in the water, u_s, is lower, in between, or higher than the wave speeds, c_s and c_p, in the solids, respectively. In Case I, with an aluminum core, the shock speed is lower than both the shear and pressure wave speed: $u_s < c_s < c_p$. The shear (s) and pressure (p) waves

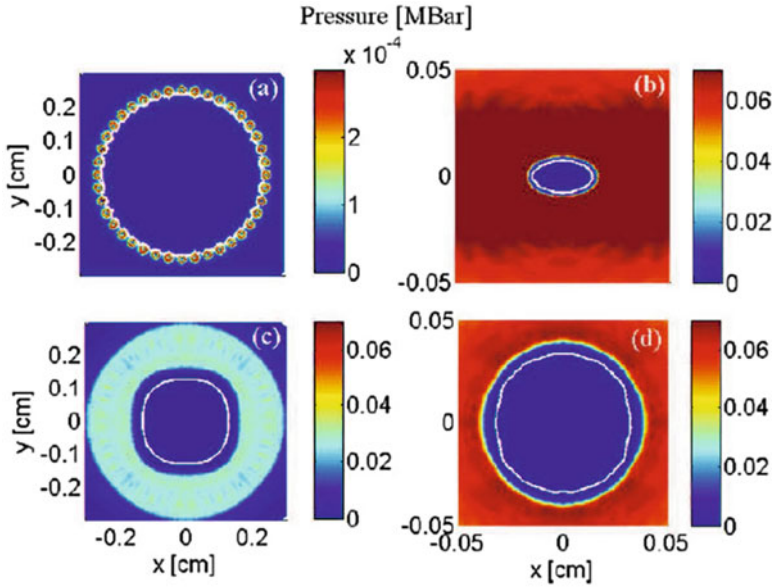

Fig. 3.118 Shock front isobars for (**a**) small-scale initial disturbances and (**b**), (**c**), and (**d**) dipole, quadrupole, and odd-even nonuniformities, reproduced from [71], with the permission of AIP

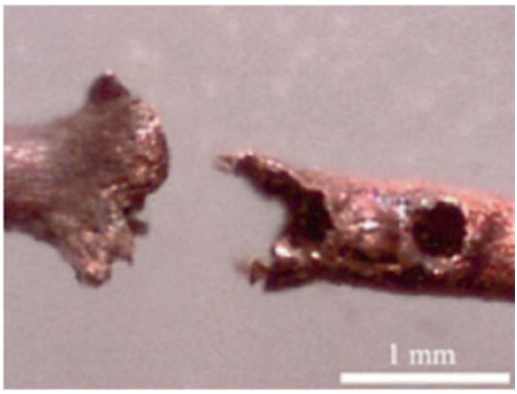

Fig. 3.119 General view of the damaged Cu tube placed at the vicinity of implosion center, reproduced from [5], with the permission of AIP

propagate faster than the shock wave in the water. Theoretically, this produces two oblique shocks in the water, θ_{wp} and θ_{ws}, as depicted in Fig. 3.120. The angles of the oblique shocks are given by $\theta_{\mathrm{wp}} = \arcsin(c_w/c_{\mathrm{p}})$, and $\theta_{\mathrm{ws}} = \arcsin(c_w/c_{\mathrm{s}})$, where c_{w} represents the speed of sound in water. The speed of sound in pure water depends only on temperature to a good approximation. In the present experiments, the ambient temperature was $23 \pm 1\,^{\circ}\mathrm{C}$, giving a speed of sound of 1491 ± 2.8 m/s in water.

Case II corresponds to a shock speed in water larger than the s wave and slower than the p wave in the solid, $c_{\mathrm{s}} < u_{\mathrm{s}} < c_{\mathrm{p}}$. This case was studied with the core

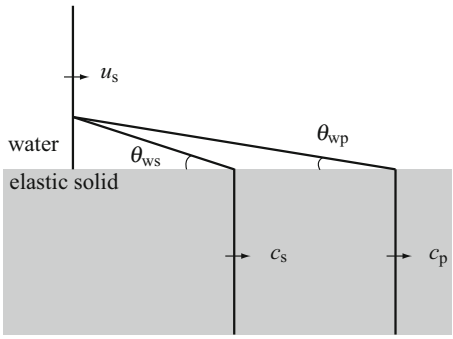

Fig. 3.120 Case I, the speed of the shock, u_s, is faster than both the s and p wave. The core material is aluminum, reproduced from [43], with permission from Springer

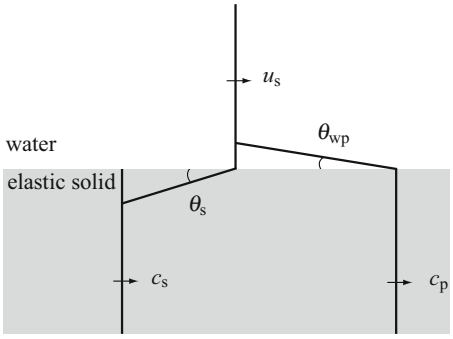

Fig. 3.121 Case II, the speed of the shock, u_s, is faster than the s wave and slower than the p wave. The core material is polycarbonate, reproduced from [43], with permission from Springer

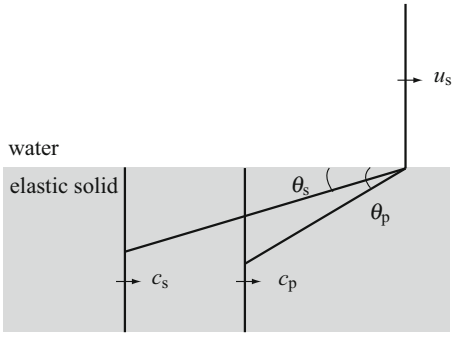

Fig. 3.122 Case III, the speed of the shock, u_s, is faster than both the s and p wave. The core material is Solithane, reproduced from [43], with permission from Springer

made of polycarbonate. The s wave propagates slower than the shock wave, and p waves propagate faster. This results in one oblique shock in water and one oblique shock in the solid. See Fig. 3.121. The angle for the oblique shock for the s wave in the solid is given by $\theta_s = \arcsin(c_s/u_s)$.

The last case, Case III, is when the shock speed in the water is larger than both the s and p wave speeds; see Fig. 3.122. A core made of Solithane results in this condition. The oblique shock in the solid corresponding to the p wave is given by $\theta_p = \arcsin(c_p/u_s)$.

A sequence of schlieren images recorded with a high-speed camera for the aluminum core is shown in Figs. 3.123 and 3.124, from [43]. Weak precursors

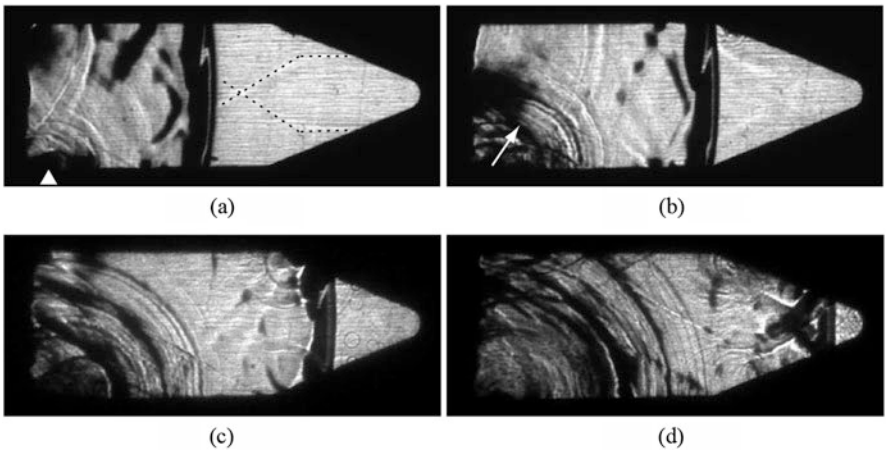

Fig. 3.123 A schlieren sequence for Case I. Exposure time: 200 ns. Impact speed $u_i = 45.4$ m/s. (**a**) $t = 0\,\mu$s. (**b**) $t = 7\,\mu$s. (**c**) $t = 14\,\mu$s. (**d**) $t = 21\,\mu$s, reproduced from [43], with permission from Springer

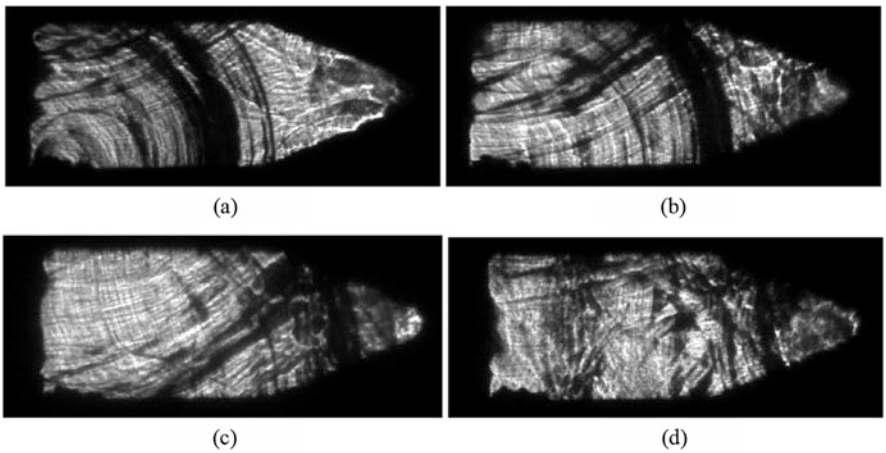

Fig. 3.124 A schlieren sequence for Case I. Exposure time: 200 ns. Impact speed $u_i = 45.4$ m/s. (**a**) $t = 27\,\mu$s. (**b**) $t = 34\,\mu$s. (**c**) $t = 41\,\mu$s. (**d**) $t = 63\,\mu$s, reproduced from [43], with permission from Springer

of the shear wave propagation in the aluminum are seen in the water in both frames reproduced in Fig. 3.123a and b, marked by black dotted lines in the frame reproduced in Fig. 3.123a. A bubble, located in the lower left corner in the frame reproduced in Fig. 3.123a, is oscillating in response to the passage of the shock wave. The oscillations send out compression waves, one of which is marked with an arrow in frame Fig. 3.123b. The shear waves in the aluminum core are traveling with almost twice the velocity of the shock wave in the water. When the shear waves

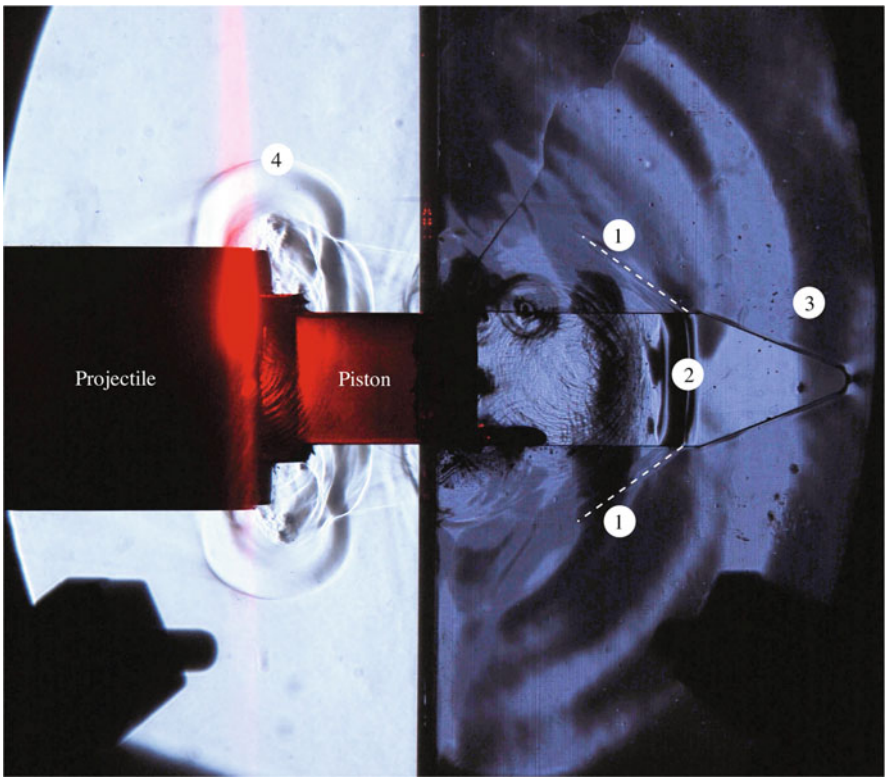

Fig. 3.125 Schlieren image recorded for Case II using a Nikon D80 camera and a 20 ns single spark source. (1) Oblique shear waves, (2) shock wave in water, (3) pressure wave, and (4) shock waves in air. Impact speed $u_i = 56.6$ m/s, reproduced from [43], with permission from Springer

pass the wedge tip, the wedge tip gets a drag in the direction of the shear waves, and the resulting force on the wedge puts the water in tension. As a result, cavitation bubbles are visible in front of the shock wave in the frame reproduced in Fig. 3.123c. The bubbles collapse violently and disturb the wave propagation in the subsequent frames, as shown in frames Fig. 3.124a–c by the smudge at the interface between the water and the solid wedge. The shock wave has focused and is reflecting in frames Fig. 3.124a–d.

A typical schlieren image for Case II is shown in Fig. 3.125. The projectile, shown moving from left to right in the image, has already impacted the polycarbonate piston. Note that the piston is only partially inserted into the water-filled cavity as revealed by the portion, which appears black, as opposed to the portion in air that is glowing red from the scattered laser light. The red vertical streak of light shown crossing the projectile's path is the HeNe laser beam used to trigger the measurement diagnostics. The image shows waves in three separate media simultaneously: shock waves in air, shock waves in water, and shear and pressure waves in a solid.

The impact between the projectile and the piston generates a toroidal shock wave in the air. The symmetry of the upper and lower parts of the toroidal shock indicates that the impact was aligned (planar) and well controlled. Once the Mach number of the toroidal shock wave is established for a certain impact velocity, the toroidal shock can be used as an internal clock for events following, making it possible to determine the instant of the impact. The toroidal shock wave in the air (denoted as 4 in Fig. 3.125, left) has traveled a distance of 18.3 ± 0.2 mm during the impact time, t_i. The shock Mach number of $M = 1.14 \pm 0.01$ indicates a relatively weak shock wave in air.

By analyzing Fig. 3.125, the speed of the shock wave, u_s, propagating through the water can be estimated by measuring the Mach angle, θ_s, of the oblique shock in the polycarbonate core (denoted 1). The angle measures as $38 \pm 1\,^\circ$, giving the speed of the shock in water $u_\mathrm{s} = c_\mathrm{solid}/\sin\theta = (950 \pm 50/)\sin(38 \pm 1)^\circ = 1550 \pm 88$ m/s. The shock wave in water (denoted 2) has traveled 43 mm with shock a Mach number of $M_\mathrm{s} = u_\mathrm{s}/c_\mathrm{w} = (1550 \pm 88)/1491 \pm 2.8 = 1.04 \pm 0.06$, which is consistent with a weak (acoustic) shock in water. Behind the shock in water is an intricate shock pattern consisting of a large number of circular shocks generated by collapsing bubbles induced by cavitation. The time of impact can be estimated by following the path of the shock wave in the water. First, there is a delay set on the time-delay unit, in this case, $t_\mathrm{d} = 94\,\mu$s. It takes $t_\mathrm{p} = l_p/c_\mathrm{p} = 0.041 \pm 0.001$ m$/2100 \pm 100$ m/s$= 19 \pm 1\,\mu$s for the pressure wave to propagate through the piston, with length l_p, until it emerges into the water. Then, it takes $t_\mathrm{w} = l_\mathrm{w}/u_\mathrm{s} = 42.7 \pm 1$ mm$/1550 \pm 90$ m/s $= 27 \pm 1.7\,\mu$s for the shock wave to travel the distance between the end of the piston to the current position, l_w. Thus the time of impact, t_i, can be estimated as $t_\mathrm{i} = t_\mathrm{d} - t_\mathrm{p} - t_\mathrm{w} = 47 \pm 2\,\mu$s before the time instant in the present frame. The pressure wave in the polycarbonate is too weak to generate a detectable oblique shock in the water; consequently the angle denoted θ_wp in Fig. 3.121 is not visible in the schlieren image. The pressure wave (the dark/light band denoted 3) has almost reached the tip of the wedge. As can be seen in the image data, the pressure wave has traveled 70 ± 1 mm in $27 \pm 1.7\,\mu$s, corresponding to a speed of 2540 ± 160 m/s.

These experiments were among the first to show shock waves in air and water simultaneously as pressure and shear waves in a solid at the same time.

Similar experiments were later performed by Wang et al. [110–113]. In these experiments, thinner surrounding structures than used in the previously described experiments by Eliasson et al. [43] were used to further study fluid-structure interactions during underwater shock focusing events. Figure 3.126 shows a schlieren sequence taken with a 1.3 mm thick 1018 steel specimen shaped according to a logarithmic spiral.

Precursor waves are seen in Fig. 3.126b, denoted by arrow 1, and Fig. 3.126c, denoted by arrow 2. The curvature of these waves indicates that the source of the wave is decelerating. A probable reason for the formation of the curved precursor waves is the attenuation and deceleration of the traveling flexural waves in the

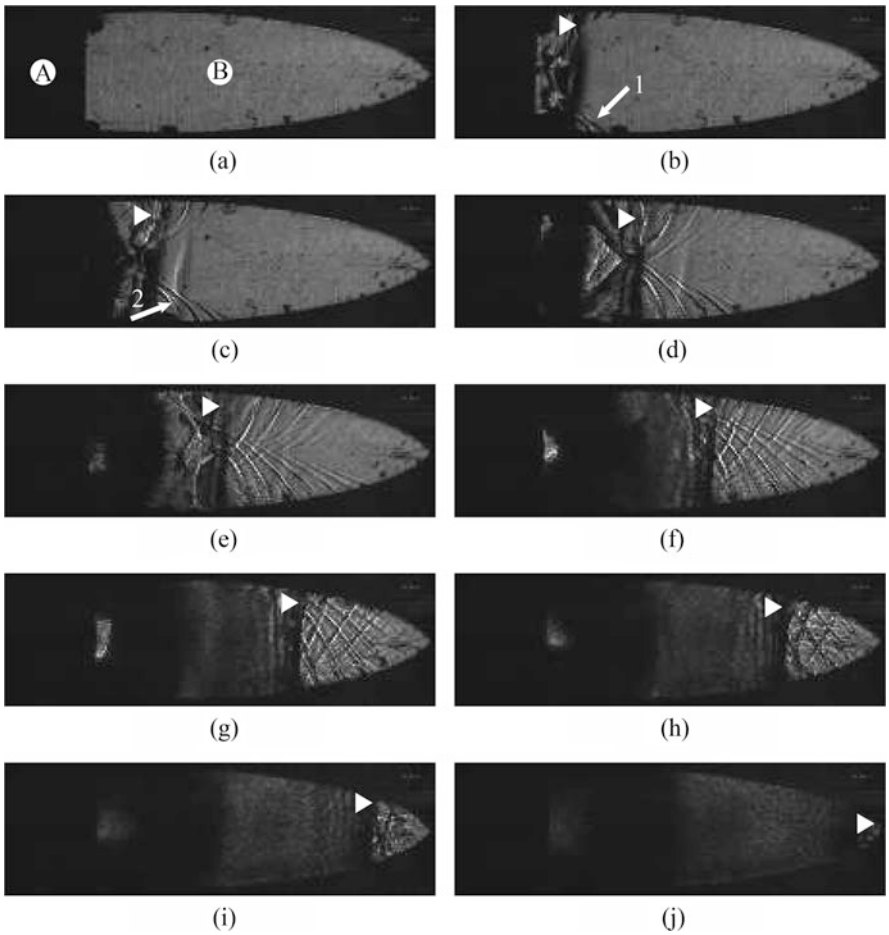

Fig. 3.126 Schlieren images for a 1.3 mm thick steel specimen. Projectile impact speed: 56 ± 1 m/s, exposure time: 40 ns. (**a**) Before test. (**b**) $\Delta t = 0\,\mu s$. (**c**) $\Delta t = 7.09\,\mu s$. (**d**) $\Delta t = 14.19\,\mu s$. (**e**) $\Delta t = 21.3\,\mu s$. (**f**) $\Delta t = 28.4\,\mu s$. (**g**) $\Delta t = 35.5\,\mu s$. (**h**) $\Delta t = 42.59\,\mu s$. (**i**) $\Delta t = 49.69\,\mu s$. (**j**) $\Delta t = 56.8\,\mu s$, reproduced from [113], with permission from Elsevier

solid. Figure 3.126g shows the precursor waves broadening, likely caused by the dispersive characteristic of the flexural waves [83].

Background-oriented schlieren techniques were applied to similar experimental setups reported in [111]. This allowed the authors to not only obtain qualitative schlieren images but also to estimate density and pressure in the water-filled region; see Fig. 3.127.

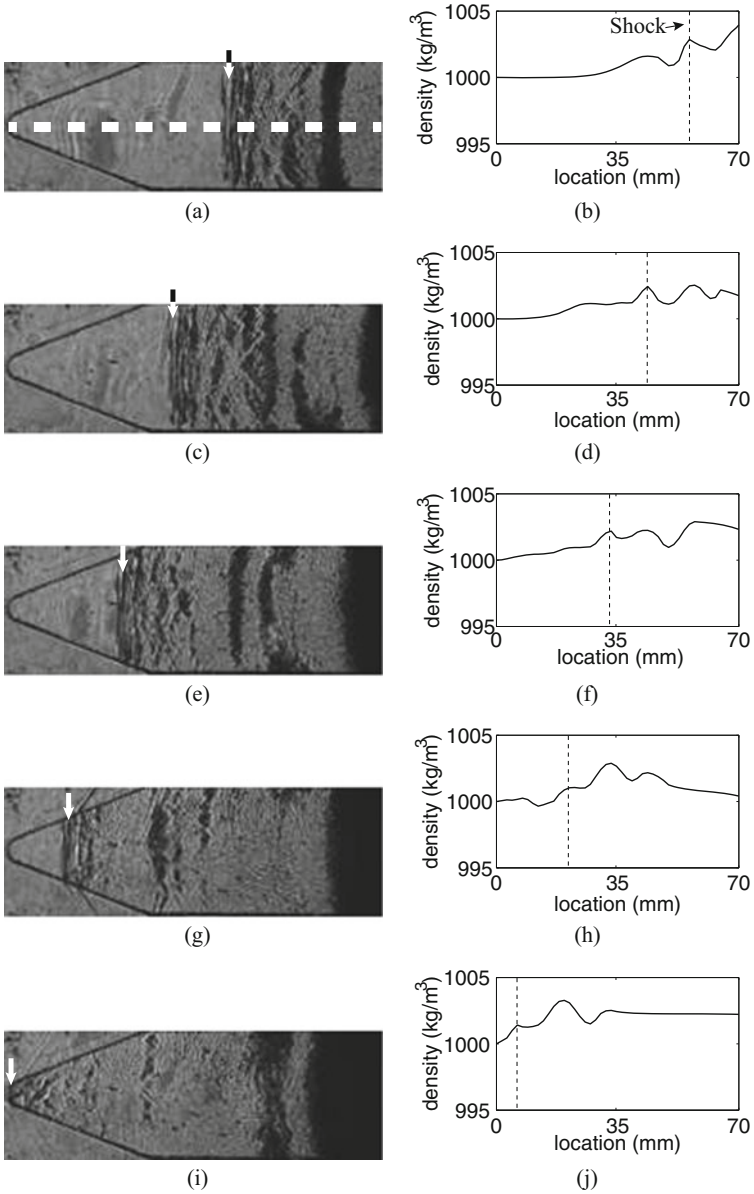

Fig. 3.127 (**a**)–(**e**) Schlieren images. Time interval between frames is 6.9 µs. (**a**) $t = 39.0\,\mu s$, (**b**) $t = 45.9\,\mu s$, (**c**) $t = 52.8\,\mu s$, (**d**) $t = 59.7\,\mu s$, and (**e**) $t = 66.6\,\mu s$. (**f**)–(**j**) Density plot along the center line (indicated in (**a**)) and shock wave location (dashed line) as a function of time. (**f**) $t = 38.45\,\mu s$, (**g**) $t = 46.14\,\mu s$, (**h**) $t = 53.83\,\mu s$, (**i**) $t = 61.52\,\mu s$, and (**j**) $t = 69.21\,\mu s$. The time difference between the schlieren images and BOS data was due to a change of the camera setup, reproduced from [111], with permission from Springer

3.9 Shock Mitigation Using Shock Focusing Techniques

Wan and Eliasson investigated shock mitigation techniques using shock focusing to delay and disperse a shock wave propagating in a two-dimensional channel [109]. Shock wave interaction with solid obstacles arranged in various geometrical patterns can be used for both shock strength amplification or mitigation purposes. Knowledge of one area can be transferred to the other, since the governing shock dynamics is essentially the same. The shock dynamics community has been interested in amplifying the shock strength using converging shock waves since the 1950s [84]. The main reason for the interest in shock focusing is that it can be used as an efficient tool to create high temperatures and pressures at the focal region. A number of experimental efforts have proved that obstacles placed in the path of the converging shock wave can help to stabilize the shock during the focusing phase; see, e.g. [11, 40, 67, 104, 105, 115]. On the other hand, the opposite of shock focusing, namely, shock wave attenuation, is highly relevant to a number of military and civil applications. If an incident shock wave can be deflected or diminished in strength, people and structures can be kept safe. For example, ventilation ducts and tunnels act as wave guides; therefore, it is important to understand how to attenuate shock waves using obstacle barriers. Simply erecting a wall to reflect the shock wave back is not necessarily desirable, since the increase in thermodynamic properties due to the reflection is high. This study, instead of using a matrix of obstacles, an arrangement of square or cylindrical obstacles placed along a logarithmic spiral curve, was investigated, motivated by previous work on shock focusing using logarithmic spirals [110, 111]. Results show that obstacles placed along a logarithmic spiral could delay both the transmitted and the reflected shock wave.

Collection of data starts when the shock wave first impacts the leading edge of the obstacles and the simulation then lasts for about 500 µs. Numerical schlieren plots for nine different obstacle configurations at time instant $t = 500\,\mu s$ are shown in Fig. 3.128. The first four cases, from top to bottom, are arranged in non-staggered columns (NS, NC, NFT, NBT). The fifth and sixth cases (SS and SC) are arranged in staggered patterns. The obstacles in the seventh, eighth, and ninth cases are placed along a logarithmic spiral (LSS, SLS, LCS). The reflected and transmitted shocks and vortices behind the obstacles are clearly visualized in the schlieren plots. Of the first six cases, the NFT case most efficiently minimizes the transmitted shock, and NBT most efficiently reduces the reflected shock wave. The fluid velocities downstream of the obstacle arrays are smaller for staggered cases than non-staggered cases. For different incident shock Mach numbers, away from the logarithmic spiral design Mach number, this shape is effective to either delay the transmitted or the reflected shock wave. Results also confirm that the degree of attenuation depends on obstacle shape, effective flow area, and obstacle arrangement, much like other obstacle configurations.

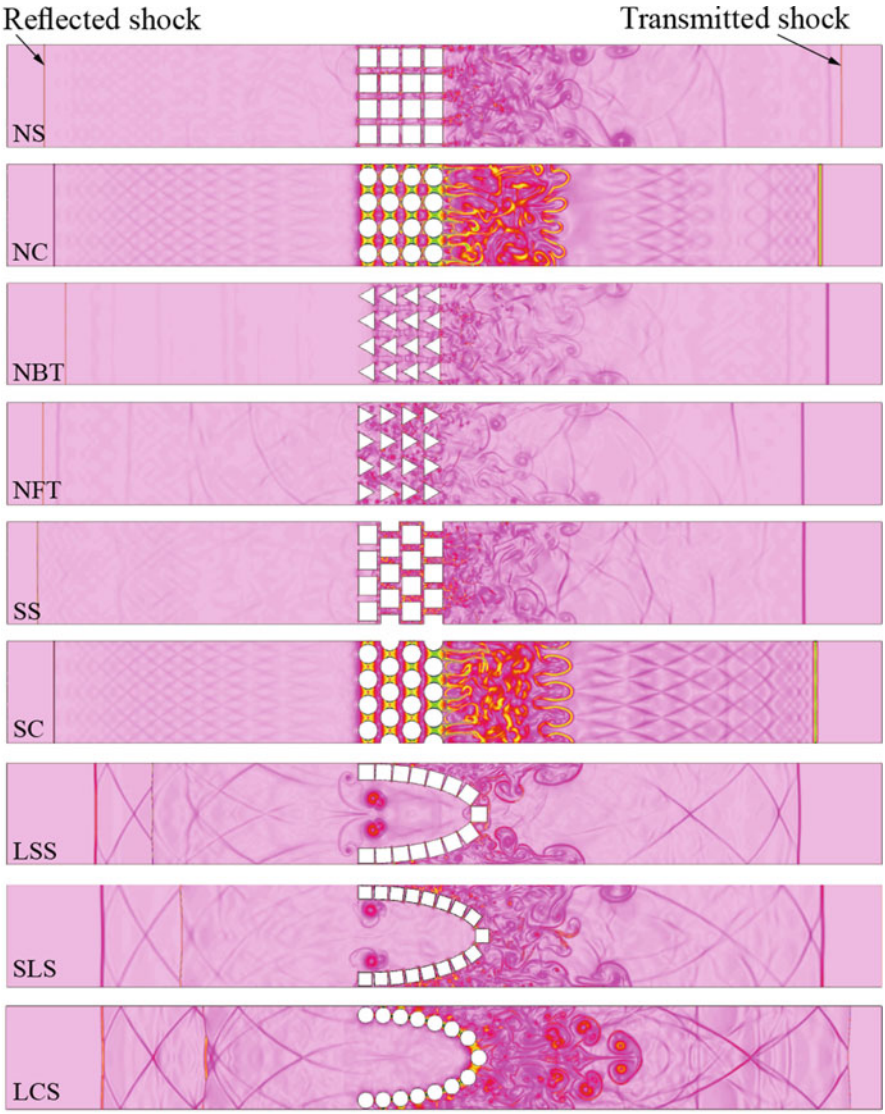

Fig. 3.128 Top to bottom: NS, NC, NBT, NFT, SS, SC, LSS, SLS, and LCS schlieren contours taken at $t = 500\,\mu s$ after the shock first impacts onto the obstacle array. The locations of the incident shock wave and the reflected shock wave are marked with arrows. Note: the first six cases, from top to bottom, were reproduced from the information given in [21]. From [109]

References

1. Ahlborn, B., Fong, K.: Stability criteria for converging shock waves. Can. J. Phys. **56**(5), 1292–1296 (1978)
2. Aki, T., Higashino, F.: A numerical study on implosion of polygonally interacting shocks and consecutive explosion in a box. In: Current Topics in Shock Waves: 17th Proceedings of the International Symposium on Shock Waves and Shock Tubes, Bethlehem, PA, 17–21 July (A91-40576 17-34), pp. 167–172. American Institute of Physics, New York (1989)
3. Antonov, O., Efimov, S., Yanuka, D., Kozlov, M., Gurovich, V.T., Krasik, Y.E.: Generation of extreme state of water by spherical wire array underwater electrical explosion. Phys. Plasmas **19**, 102702 (2012)
4. Antonov, O., Efimov, S., Yanuka, D., Kozlov, M., Gurovich, V.T., Krasik, Y.E.: Generation of converging strong shock wave formed by microsecond timescale underwater electrical explosion of spherical wire array. Appl. Phys. Lett. **102**, 124104 (2013)
5. Antonov, O., Efimov, S., Yanuka, D., Kozlov, M., Gurovich, V.T., Krasik, Y.E.: Diagnostics of a converging strong shock wave generated by underwater explosion of a spherical wire array. J. Appl. Phys. **115**, 223303 (2014)
6. Apazidis, N.: Focusing of weak shock waves in confined axisymmetric chambers. Shock Waves **3**, 201–212 (1994)
7. Apazidis, N.: Numerical investigation of shock induced bubble collapse in water. Phys. Fluids **28**, 046101 (2016)
8. Apazidis, N., Lesser, M.B.: On generation and convergence of polygonal-shaped shock waves. J. Fluid Mech. **309**, 301–319 (1996)
9. Apazidis, N., Lesser, M.B., Tillmark, N. Johansson, B.: An experimental and theoretical study of converging shock waves. Shock Waves **12**, 39–58 (2002)
10. Apazidis, N., Kjellander, M., Tillmark, N.: High energy concentration by symmetric shock focusing. Shock Waves **23**, 361–368 (2013)
11. Balasubramanian, K., Eliasson, V.: Numerical investigations of the porosity effect on the shock focusing process. Shock Waves **23**(6), 583–594 (2013)
12. Barbry, H., Mounier, C., Saillard, Y.: Transformation d'un choc plan uniforme en choc cylindrique ou spherique uniforme Classical and quantum mechanics, general physics (A1110), Report CEA-N–2516, France (1986)
13. Baronets, P.: Imploding shock waves in a pulsed induction discharge. Fluid Dyn. **19**, 503–508 (1984)
14. Betelu, S.I., Aronson, D.G.: Focusing of noncircular self-similar shock waves. Phys. Rev. Lett. **87**(7), 074501 (2001)
15. Book, D., Löhner, R.: Simulation and theory of the quatrefoil instability of a converging cylindrical shock. In: Current Topics in Shock Waves: 17th Proceedings of the International Symposium on Shock Waves and Shock Tubes, Bethlehem, PA, 17–21 July (A91-40576 17-34), pp. 149–154. American Institute of Physics, New York (1989)
16. Bond, C., Hill, D.J., Meiron, D.I., Dimotakis, P.E.: Shock focusing in a planar convergent geometry: experiment and simulation. J. Fluid Mech. **641**, 297–333 (2009)
17. Brode, H.L.: Quick estimates of peak overpressure from two simultaneous blast waves. Tech. rep., Tech. Rep. DNA4503T, Defense Nuclear Agency, Aberdeen Proving Ground, MD (1977)
18. Butler, D.: Converging spherical and cylindrical shocks. Report No. 54/54, Burgess Hill, New York (1954)
19. Cass, A.S.: Comparison of first generation (Dornier HM3) and second generation (Medstone STS) lithotriptors: treatment results with 13,864 renal and ureteral calculi. J. Urology. Am. Urological Ass. **153**, 588–592 (1995)
20. Cates, J., Sturtevant, B.: Shock wave focusing using geometrical shock dynamics. Phys. Fluids **9**(10), 3058–3068 (1997)
21. Chaudhuri, A., Hadjadj, A., Sadot, O., Ben-Dor, G.: Numerical study of shock-wave mitigation through matrices of solid obstacles. Shock Waves **23**, 91–101 (2013)

22. Chessire, G., Henshaw, W.D.: Composite overlapping meshes for solution of partial differential equations. J. Comput. Phys. **1**, 1 (1990)
23. Chester W.: The propagation of shock waves in a channel of non-uniform width. Quart. J. Mech. Appl. Math. **6**(4), 440–452 (1953)
24. Chester, W.: The quasi-cylindrical shock tube. Philos. Mag. **45**, 1239–1301 (1954)
25. Chisnell, R.F.: The normal motion of shock wave through a non-uniform one-dimensional medium. Proc. R. Soc. A **232**, 350–370 (1955)
26. Chisnell R.F.: The motion of a shock wave in a channel, with applications to cylindrical and spherical shock waves. J. Fluid Mech. **2**(3), 286–298 (1957)
27. Chisnell, R.F.: An analytic description of converging shock waves. J. Fluid Mech. **354**, 357–375 (1998)
28. Christopher, T.: Modeling the Dornier HM3 lithotripter. J. Acoust. Soc. Am. **96**(5), 3088–3095 (1994)
29. Christopher, P.T., Parker, K.J.: New approaches to nonlinear diffractive field propagation. J. Acoust. Soc. Am. **90**(5), 488–499 (1991)
30. Cocchi, J.P.,Saurel, R.,Loraud, J.C.: Treatment of interface problems with Godunov-type schemes. Shock Waves **65**, 347–357 (1996)
31. Coleman, A.J., Saunders, J.E.: A survey of the acoustic output of commercial extracorporeal shockwave lithotripters. Ultasound Med. Biol. **15**, 213–227 (1989)
32. Davitt, K., Arvengas, A., Caupin, F.: Water at the cavitation limit: density of the metastable liquid and size of the critical bubble. Europhys. Lett. **90**, 16002 (2010)
33. De Neef, T., Hechtman, C.: Numerical study of the flow due to a cylindrical implosion. Comput. Fluids **6**, 185–202 (1978)
34. Demmig, F., Hemmsoth, H.H.: Model computation of converging cylindrical shock waves – initial configurations, propagation, and reflection. In: Current Topics in Shock Waves: 17th Proceedings of the International Symposium on Shock Waves and Shock Tubes, Bethlehem, PA, 17–21 July (A91-40576 17-34), pp. 155–160. American Institute of Physics, New York (1989)
35. Dennen, R.S., Wilson, L.N.: Electrical generation of imploding shock waves. In: Exploding Wires, pp. 145–157. Plenum Press, New York (1962)
36. Dimotakis, P.E., Samtaney, R.: Planar shock cylindrical focusing by a perfect-gas lens. Phys. Fluids **18**, 031705 (2006)
37. Dumitrescu, L.Z.: On efficient shock-focusing configurations. In: Proceedings, 11th Australian Fluid Mechanics Conference, University of Tasmania, Hobart, Australia (1992)
38. Eliasson, V., Gross, J.: Experimental investigation of shock wave amplification using multiple munitions. In: Ben-Dor, G., et al. (eds.) 30th International Symposium on Shock Waves 2, pp. 1017–1021 (2017)
39. Eliasson, V., Apazidis, N., Tillmark, N., Lesser, M.B.: Focusing of strong shocks in an annular shock tube. Shock Waves **15**, 205–217 (2006)
40. Eliasson, V., Apazidis, N., Tillmark, N.: Controlling the form of strong converging shocks by means of disturbances. Shock Waves **17**, 29–42 (2007)
41. Eliasson, V., Tillmark, N., Szeri, A.J., Apazidis, N.: Light emission during shock focusing in air and argon. Phys. Fluids **19**, 106106 (2007)
42. Eliasson, V., Kjellander, M., Apazidis, N.: Regular versus Mach reflection for converging polygonal shocks. Shock Waves **17**, 43–50 (2007)
43. Eliasson, V., Mello, M., Rosakis, A.J., Dimotakis, P.E.: Experimental investigation of converging shocks in water with various confinement materials. Shock Waves **20**, 395–408 (2010)
44. El Mekki-Azouzi, M., Ramboz, C., Lenain, J.-F., Caupin, F.: A coherent picture of water at extreme negative pressure. Nat. Phys. **9**, 38–41 (2013)
45. Evans, A.K.: Instability of converging shock waves and sonoluminescence. Phys. Fluids **22**(3), 5004–5011 (1996)
46. Fisher, J.C.: The fracture of liquids. J. Appl. Phys. **19**, 1062–1067 (1948)
47. Fong, K., Ahlborn, B.: Stability of converging shock waves. Phys. Fluids **22**(3), 416–421 (1979)

48. Fujumoto, Y., Mishkin, E.: Analysis of spherically imploding shocks. Phys. Fluids **21**, 1933 (1978)
49. Gardner, G.H., Book, D.L., Bernstein I.B.: Stability of imploding shocks in the CCW approximation. J. Fluid Mech. **114**, 41–58 (1982)
50. Glass, I.I.: Shock Waves and Man. University of Toronto Institute for Aerospace Studies, Toronto (1974)
51. Godunov, S.K.: A difference scheme for numerical solution of discontinuous solution of hydrodynamic equations. Math. Sbornik **47**, 271–306 (1959)
52. Guderley, G.: Starke kugelige und zylindrische Verdichtungsstöße in der Nähe des Kugelmittelpunktes bzw. der Zylinderachse. Luftfahrt Forsch. **19**, 302–312 (1942)
53. Gustafsson, G.: Focusing of weak shock waves in a slightly elliptical cavity. J. Sound Vib. **116**(1), 137–148 (1987)
54. Hafner, P.: Strong converging shock waves near the center of convergence: a power series solution. J. Appl. Math. **48**, 1244 (1988)
55. Hamilton, M.F.: Transient axial solution for the reflection of a spherical wave from a concave ellipsoidal mirror. J. Acoust. Soc. Am. **93**(3), 1256–1266 (1993)
56. Henshaw, W.D., Smyth, N.F., Schwendeman, D.W.: Numerical shock propagation using geometrical shock dynamics. J. Fluid Mech. **171**, 519–545 (1986)
57. Hikida, S., Needham, C.E.: Low amplitude multiple burst (lamb) model. Tech. rep., S-cubed Final Report, S-CUBED-R-81-5067 (1981)
58. Hornung, H.G., Pullin, D.I., Ponchaut, N.F.: On the question of universality of imploding shock waves. Acta Mech. **201**, 31–35 (2008)
59. Hosseini, S.H.R., Takayama, K.: Implosion from a spherical shock wave reflected from a spherical wall. J. Fluid Mech. **530**, 223–239 (2005)
60. Johansson, B., Apazidis, N., Lesser M.B.: On shock waves in a confined reflector. Wear **233–235**, 79–85 (1999)
61. Johnsen, E., Colonius, T.: Shock-induced collapse of a gas bubble in shockwave lithotripsy. J. Acoust. Soc. Am. **124**(4), 2011–2020 (2008)
62. Johnsen, E., Colonius, T.: Numerical simulations of non-spherical bubble collapse. J. Fluid Mech. **629**, 231–262 (2009)
63. Kandula, M., Freeman, R.: On the interaction and coalescence of spherical blast waves. Shock Waves **18**, 21–33 (2008)
64. Keefer, J.H., Reisler, R.E.: Simultaneous and non-simultaneous multiple detonations. In: Proceeding of the 14th International Symposium on Shock Waves and Shock Tubes, New South Wales, Australia, pp. 543–552 (1984)
65. Kjellander, M., Tillmark, N., Apazidis, N.: Thermal radiation from a converging shock implosion. Phys. Fluids **22**, 046102 (2010)
66. Kjellander, M., Tillmark, N., Apazidis, N.: Shock dynamics of strong imploding cylindrical and spherical shock waves with real gas effects. Phys. Fluids **22**, 116102 (2010)
67. Kjellander, M., Tillmark, N., Apazidis, N.: Experimental determination of self-similarity constant for converging cylindrical shocks. Phys. Fluids **23**(11), 116103 (2011)
68. Kjellander, M., Tillmark, N., Apazidis, N.: Energy concentration by spherical converging shocks generated in a shock tube. Phys. Fluids **24**, 126103 (2012)
69. Kleine, H.: Time resolved shadowgraphs of focusing cylindrical shock waves. Study treatise at the Stoßenwellenlabor, RWTH Achen, FRG (1985)
70. Knystautas, R., Lee, B., Lee, J.: Diagnostic experiments on converging detonations. Phys. Fluids. Suppl. **1**, 165–168 (1969)
71. Kozlov, M., Gurovich, V.T., Krasik, Y.E.: Stability of imploding shocks generated by underwater electrical explosion of cylindrical wire array. Phys. Plasmas **20**, 112107 (2013)
72. Lazarus, R.: Self-similar solutions for converging shocks and collapsing cavities. SIAM J. Numer. Anal. **18**, 316 (1981)
73. Lazarus, R., Richtmyer, R.: Similarity Solutions for Converging Shocks. Los Alamos Scientific Laboratory of the University of California, Los Alamos, NM (1977)

74. Liverts, M., Apazidis, N.: Limiting temperatures of spherical shock wave implosion. Phys. Rev. Lett. **116**, 014501 (2016)
75. Matsuo, H., Nakamura, Y.: Experiments on cylindrically converging blast waves. J. Appl. Phys. **51**, 3126–3129 (1980)
76. Matsuo, H., Nakamura, Y.: Cylindrically converging blast waves in air. J. Appl. Phys. **52**, 4503–4507 (1981)
77. Matsuo, M., Ebihara, K., Ohya, Y.: Spectroscopic study of cylindrically converging shock waves. J. Appl. Phys. **58**(7), 2487–2491 (1985)
78. McMillen, J.H.: Shock wave pressures in water produced by impact of small spheres. Phys. Rev. **68**(9,10),198–210 (1945)
79. Mishkin, E.A., Fujimoto, Y.: Analysis of a cylindrical imploding shock wave. J. Fluid Mech. **89**(1), 61–78 (1978)
80. Müller, M.: Comparison of Dornier lithotripters: measurement of shock wave fields and fragmentation effectiveness. Biomed. Tech. **35**, 250–262 (1990)
81. Nakamura, Y.: Analysis of self-similar problems of imploding shock waves by method of characteristics. Phys. Fluids **26**, 1234 (1983)
82. Neemeh, R.A., Ahmad, Z.: Stability and collapsing mechanism of strong and weak converging cylindrical shock waves subjected to external perturbation. In: Proceeding of the 14th International Symposium on Shock Waves and Shock Tubes, Berkeley, CA, 28 July–2 Aug, pp. 423–430. Stanford University Press, Stanford (1986)
83. Norris, A.N.: Flexural waves on narrow plates. J. Acoust. Soc. Am. **113**, 2647–2658 (2003)
84. Perry, R.W., Kantrowitz, A.: The production and stability of converging shock waves. J. Appl. Phys. **22**(7), 878–886 (1951)
85. Ponchaut, N., Hornung, H.G., Mouton, D.I.: On imploding cylindrical and spherical shock waves in a perfect gas. J. Fluid Mech. **560**, 103 (2006)
86. Qiu, S., Eliasson, V.: Interaction and coalescence of multiple simultaneous and non-simultaneous blast waves. Shock Waves **26**(3), 287–297 (2016)
87. Qiu, S., Liu, K., Eliasson, V.: Parallel implementation of geometrical shock dynamics for two-dimensional converging shock waves. Comput. Phys. Commun. **207**, 186–192 (2016)
88. Ramsey S.D., Kammb J.R., Bolstad J.H.: The Guderley problem revisited. Int. J. Comput. Fluid Dyn. **26**(2), 79–99 (2012)
89. Roberts, D.E., Glass, I.I.: Spectroscopic investigation of combustion-driven spherical implosion waves. Phys. Fluids **14**, 1662–1670 1971
90. Roig, R.A., Glass, I.I.: Spectroscopic study of combustion-driven implosions. Phys. Fluids **20**, 1651–1656 (1977)
91. Saillard, Y., Barbry, H., Mounier, C.: Transformation of a plane uniform shock into cylindrical or spherical uniform shock by wall shaping. In: Proceedings of the XV-th International Symposium on Shack Tubes and Waves. Stanford University Press, Stanford (1985)
92. Saito, T., Glass, I.: Temperature measurements at an implosion focus. Proc. R. Soc. Lond. A **384**, 217–231 (1982)
93. Sankin, G.N., Zhou, Y., Zhong, P.: Focusing of shock waves induced by optical breakdown in water. J. Acoust. Soc. Am. **123**(6), 4071–4081 (2008)
94. Schwendeman, D.W., Whitham, G.B.: On converging shock waves. Proc. R. Soc. Lond. A **413**, 297–311 (1987)
95. Schwendeman, D.W.: On converging shock waves of spherical and polyhedral form. J. Fluid Mech. **454**, 365–386 (2002)
96. Sembian, S., Liverts, M., Tillmark, N., Apazidis, N.: Plane shock wave interaction with a cylindrical column. Phys. Fluids **28**, 056102 (2016)
97. Sommerfeld, M., Müller, H.M.: Experimental and numerical studies of shock wave focusing in water. Exp. Fluids **6**, 209–216 (1988)
98. Stan, C.A., Willmont, P.R., Stone, H.A., Koglin, J.E., Mengling, L., Aquila, A.L., Robinson, J.S., Gumerlock, K.L., Blaj, G., Sierra, R.G., Boulet, S., Guillet, S.A.H., Curtis, R.H., Vetter, S.L., Loos, H., Turner, J.L., Decker, F.-J.: Negative pressures and spallation in water drops subjected to nanosecond shock waves. Phys. Chem. Lett. **7**, 2055–2062 (2016)

99. Stanyukovich, K.: Unsteady Motion of Continuous Media. Pergamon, Oxford (1960)
100. Stanyukovich, K.P.: Unsteady Motion of Continuous Media. Pergamon Press, Oxford (1960)
101. Starkenberg, J.K., Benjamin, K.J.: Predicting coalescence of blast waves from sequentially exploding ammunition stacks. Tech. rep., Army Research Lab Report ARL-TR-645 (1994)
102. Sturtevant, B., Kulkarny, V.A.: The focusing of weak shock waves. J. Fluid Mech. **73**(04), 651–671 (1976)
103. Sun, M., Takayama, K.: An artificially upstream flux vector splitting scheme for the Euler equations. J. Comput. Phys. **189**(1), 305–329 (2003)
104. Takayama, K., Onodera, O., Hoshizawa, Y.: Experiments on the Stability of Converging Cylindrical Shock Waves. Shock Waves Marseille IV, pp. 117–127. Springer, Berlin (1984)
105. Takayama, K., Kleine, H., Grönig, H.: An experimental investigation of the stability of converging cylindrical shock waves in air. Exp. Fluids **5**, 315–322 (1987)
106. Taylor, G.: The formation of a blast wave by a very intense explosion. I. Theoretical discussion. Proc. R. Soc. Lond. A Math. Phys. Sci. **201**, 159–174 (1950)
107. Trevena, D.H.: Cavitation an generation tension in liquid. J. Phys. D: Appl. Phys. **17**, 2139–2164 (1984)
108. Van Dyke, M., Guttman, A.: The converging shock wave from a spherical or cylindrical piston. J. Fluid Mech. **120**, 451 (1982)
109. Wan, Q., Eliasson, V.: Numerical study of shock wave attenuation in two-dimensional ducts using solid obstacles – How to utilize shock focusing techniques to attenuate shock waves. Aerospace **2**, 203–221 (2015)
110. Wang, C., Eliasson, V.: Shock wave focusing in water inside convergent structures. Int. J. Multiphys. **6**, 267–282 (2012)
111. Wang, C., Qiu, S., Eliasson, V.: Quantitative pressure measurement of shock waves in water using a schlieren-based visualization technique. Exp. Tech. (2013). https://doi.org/10.1111/ext.12068
112. Wang, C., Qiu, S., Eliasson, V.: Investigation of shock wave focusing in water in a logarithmic spiral duct, part 1: Weak coupling. Ocean Eng. **102**, 174–184 (2014). https://doi.org/10.1016/j.oceaneng.2014.09.012
113. Wang, C., Grunenfelder, L., Patwardhan, R., Qiu, S., Eliasson, V.: Investigation of shock wave focusing in water in a logarithmic spiral duct, part 2: strong coupling. Ocean Eng. **102**, 185–196 (2015)
114. Watanabe, M., Takayama, K.: Stability of converging cylindrical shock waves. Shock Waves **1**, 149–160 (1991)
115. Watanabe, M., Onodera, O., Takayama, K.: Shock wave focusing in a vertical annular shock tube. Theor. Appl. Mech. **32**, 99–104 (1995)
116. Welsh, R.L.: Imploding shocks and detonations. J. Fluid Mech. **29**, 61–79 (1967)
117. Whitham, G.B.: A new approach to problems of shock dynamics Part I Two-dimensional problems. J. Fluid Mech. **2**, 145–171 (1957)
118. Whitham, G.B.: A new approach to problems of shock dynamics Part II Two-dimensional problems. J. Fluid Mech. **5**, 369–386 (1957)
119. Whitham, G.B.: A note on shock dynamics relative to a moving frame. J. Fluid Mech. **31**, 449–453 (1968)
120. Whitham, G.: Linear and Nonlinear Waves. Wiley, New York (1974)
121. Wilson, D.A., Hoyt, J.W., McKune, J.W.: Measurement of tensile strength of liquids by an explosion technique. Nature **253**, 723–725 (1975)
122. Wu, J., Neemeh, R., Ostrowski, P.: Experiments on the stability of converging cylindrical shock waves. AIAA J. **19**, 257–258 (1981)
123. Zel'dovich, Y.B., Raizer, Y.P.: Physics of shock waves and high-temperature hydrodynamic phenomena. Dover Publications, New York (1966)
124. Zhai, Z., Liu, C., Qin, F., Yang, J., Luo, X.: Generation of cylindrical converging shock waves based on shock dynamics theory. Phys. Fluids **22**, 041701 (2010)
125. Zheng, Q., Durben, D.J., Wolf, G.H., Angel, C.A.: Liquids at large negative pressures: water at the homogeneous nucleation limit. Science **254**, 829–832 (1991)